MAGMAS IN MOTION: DEGASSING IN VOLCANIC CONDUITS AND

FABRICS OF PYROCLASTIC DENSITY CURRENT

A

THESIS

Presented to the Faculty

of the University of Alaska Fairbanks

in Partial Fulfillment of the Requirements

For the Degree of

DOCTOR OF PHILOSOPHY

By

Alain Burgisser, B.S.

Fairbanks, Alaska

May 2003

UMI Number: 3092289

Copyright 2003 by

Burgisser, Alain
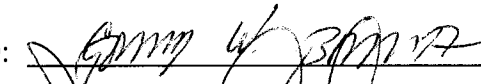
All rights reserved.

UMI®

UMI Microform 3092289

MAGMAS IN MOTION: DEGASSING IN VOLCANIC CONDUITS AND

FABRICS OF PYROCLASTIC DENSITY CURRENT

By

Alain Burgisser

RECOMMENDED: _____

_____

_____

_____

Advisory Committee Chair

_____
Chair, Department of Geology and Geophysics

APPROVED: _____
Dean, College of Science, Engineering, and Mathematics

_____
Dean of the Graduate School

_____
Date

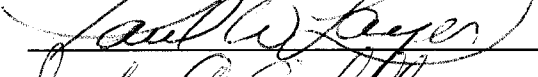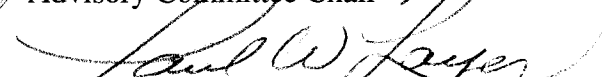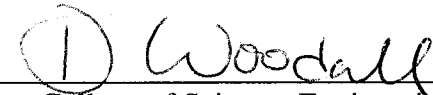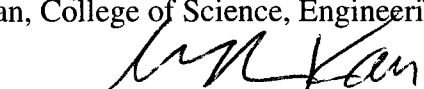# ABSTRACT

Volcanoes are caused by the transport of magma batches from the Earth's crust to the surface. These magmas in motion undergo drastic changes of rheologic properties during their journey to the surface and this work explores how these changes affect volcanic eruptions. The first part of this study is devoted to the dynamic aspects of degassing and permeability in magmas with high pressure, high temperature experiments on natural volcanic rocks. Degassing is measured by the influence of decompression rate on the growth of the bubbles present in the magma while permeability is deduced from the temporal evolution of these bubbles. The parameterization of our results in a numerical model of volcanic conduit flow show that previous models based on equilibrium degassing overestimate the acceleration and the decompression rate of the magma. Assessing permeability effects derived form our results show that the transition between explosive and effusive eruptions is a strong function of the magma initial ascent rate.

The second part of this work is a unification of two end-members of pyroclastic currents (highly concentrated pyroclastic flows and dilute, turbulent pyroclastic surges) using theoretical scaling arguments based on multiphase physics. Starting from the dynamics of the particle interactions with a fundamental eddy, we consider the full spectrum of eddies generated within a turbulent current. We demonstrate that the presence of particles with various sizes induces a density stratification of the current, leading to its segregation into a basal concentrated part overlain by a dilute cloud. To verify our predictions on the interactions of such a segregated pyroclastic current with its surroundings (hills and sea), we studied the products of the 2050 BP caldera-forming eruption of Okmok Volcano (Alaska). This field study allowed us to reconstruct the eruptive sequence and to validate the main aspects of our theoretical model, such as the superposition of a dense and dilute part, their decoupling at sea entrance and the characteristics of the particles they transport.

TABLE OF CONTENTS

LIST OF FIGURES

LIST OF TABLES

ACKNOWLEDGEMENTS

Many people have contributed to this work, the quality of which is the result of their teachings and advices. Furthermore, I am afraid that these people are partly responsible in my addiction to research and volcanology. Science undoubtedly adds to my pleasure to be 'out there', and it is reassuring to know that even the grumpiest volcanologist can be, like myself, touched by the splendors of the Earth. First and foremost, I thank Prof. John Eichelberger, who introduced me to the fascinating and beautiful world of volcanology. I am grateful for his trust, for sending me on the field as much as thinkable, and for allowing me to freely explore various aspects of physical volcanology. His energy and enthusiasm to arrange contacts with other scientists allowed me to meet inspiring people and start fruitful collaborations.

What would I know of scientific originality without the Prof. George Bergantz? His inventiveness and his irrepressible attraction towards new concepts insufflated me the urge to go off the beaten paths and explore new ideas. I owe him a philosophy of scientific explorer, for which the wilder a concept seems, the more appealing it is. His comprehensiveness of geophysics often gave me the unavoidable and inebriating vertigo caused by a glimpse at the complexity of Nature.

Dr. James Gardner taught me the art of experimental volcanology. His scientific method and rigor grounded my impatience to jump to conclusions. Our many intense discussions gave me the opportunity to test and refine my ideas, and I consider his trust as a reward of our collaboration. I also thank him for his admirable patience in correcting my (slowly improving) English.

Prof. Robert Breidenthal initiated me to the mysteries of turbulence and the secrets of the ontology of bears. Crucial concepts of this work were built on his immense knowledge of fluid dynamics, and his wittiness often made my visits to Seattle laughing rides. Working with the team of scientists at the Alaska Volcano Observatory (AVO) was a great advantage. Among others, I particularly appreciated that Dr. Tom Miller freely shared both his deep knowledge of Alaskan volcanoes and his views on pyroclastic currents. Discussions with Brandon Browne, Darren Chertkoff, Jessica Larsen, Jim Beget, Michelle Coombs, Pete Stelling, Pavel Izbekov, and many others were always stimulating and often thought-provoking. Dr. Chris Nye and Prof. Paul Layer were both members of my graduate committee, and I thank them warmly for helping to

send me at Mt. St. Helens to 'broaden my field experience'. Each chapter features specific acknowledgments to the people who helped us to conduct each project.

This short tribute would not be complete without special thanks to Tina Tin, my friends, and my family for their unwavering support. Finally, Laurent Burgisser is kindly reminded that rocks are definitively more interesting than roots...

GENERAL INTRODUCTION

Volcanologists have traditionally considered magmatic systems more as chemical components and less as material objects. During the past three decades, however, the development of physical volcanology has increased remarkably our understanding of the variety and the controls of processes linked to volcanic eruptions. Among these processes, the degassing of magma during ascent and the emplacement dynamics of pyroclastic density currents have taken a preeminent position in the mind of physical volcanologists. While degassing is the driving force behind explosive eruptions, it is also believed to hold the key to a poorly understood behavior of volcanoes: the transition between effusive and explosive eruptions during the same volcanic event. Arguably the most hazardous manifestation of explosive eruptions, pyroclastic density currents remain unpredictable in their trajectories and extent. The inner structure of these currents, which controls their emplacement dynamics, is subject to debate because direct observations are impossible. This lack of understanding of their inner workings hinders our ability to predict the area that may be impacted by these currents.

Situated at the heart of degassing processes, gas bubbles are a recognized control of eruptive dynamics. Whether an eruption will be quietly effusive, as the dome growth at Unzen Volcano (Japan) between 1990 and 1995 (Nakada et al. 1999), or violently explosive, as the 1991 Plinian eruption of Pinatubo Volcano (Philippines; Wolfe and Hoblitt 1996), depends on the way magma degasses. At depth, confined by several megapascals of pressure, the volatiles are dissolved within the magma. During ascent, however, decompression causes these volatiles to exsolve: the magma is degassing, which causes the ascent velocity to increase. The velocity of magma flowing within a volcanic conduit can easily be calculated when bubbles grow in equilibrium with the magmatic liquid. There is, however, no direct way to assess the effect of the disequilibrium between bubbles and liquid. This is a serious limitation to our understanding of eruptive dynamics because the degassing of magma in disequilibrium can affect the flow conditions within the conduit. If the volatiles are kept within bubbles in the magma, their sudden release fragments the magma and an explosive eruption arises. If, however, volatile loss occurs slowly, the magma reaches the surface degassed and an effusive eruption ensues. The capacity of the bubbles to lose gases is controlled by the permeability of the magma, which in turn results from by the coalescence of the gas bubbles. Our knowledge of the processes that might control bubble

coalescence is limited to less viscous magmas. It is therefore urgent to study coalescence for the more viscous magmas, which often alternate dome building with explosive columns in a seemingly unpredictable way.

The first chapter of this work is devoted to the questions of dynamics of degassing and permeability development within a volcanic conduit. We use decompression experiments of hydrated silicate melt to define equilibrium and disequilibrium regimes of bubble growth. We assess the consequences of these experiments on conduit flow dynamics with a one-dimensional model of magma ascent constrained by our data. We quantify the changes in dynamics induced by disequilibrium degassing, and notably the reduction of both the deviation from lithostatic pressure and the flow acceleration at high porosities that were predicted by forcing equilibrium degassing. Permeability and bubble coalescence were studied with a set of experiments run under open degassing conditions. Experiments show that bubbles start to connect at a specific porosity value and that all bubbles have coalesced after a fixed time. The introduction of coalescence into our model allows us to determine the conditions and likely controls on the transition between explosive and effusive eruptive regimes.

Pyroclastic density currents - pyroclastic flows and surges - are among the most impressive and hazardous natural gravity-driven flows. These rapidly moving mixtures of hot volcanic particles and gas travel across the slopes of volcanoes at high speeds (e.g., 150 m s^{-1} at Mt. St. Helens, Moore and Rice 1981). The speed and energy involved in these currents often have destructive consequences and are responsible for a substantial number of lost human lives and property damage (Nakada 2000). The behavior of those flows as they travel down slope is controlled by their internal structure, which results from a delicate balance between the gravity-influenced particles and the strongly buoyant gas.

In Chapter 2, we reappraise the physics of pyroclastic density currents by means of a Lagrangian approach of the interplay between particles and turbulence. We propose three dimensionless numbers based on canonical concepts of multiphase physics, the Stokes number, the stability factor, and the dense-dilute condition, which define various dynamic regimes of particle transport. Evaluations of these numbers show that transient particle concentrations are likely to generate density stratification within the currents. This stratification causes pyroclastic

density currents to segregate into a dilute cloud overriding a dense basal zone dominated by granular interactions.

Although direct observation of the internal organization of pyroclastic density currents is not possible, the currents leave behind deposits that provide a record of their structure. Our theoretical work of Chapter 2 can therefore be applied to the analysis of the deposits of such currents. In Chapter 3, I use stratigraphic and sedimentology data to characterize the various facies of the 2050 BP caldera-forming eruption of Okmok Volcano (Alaska). Beyond reconstructing the eruptive sequence, I focus on the interactions of the main pyroclastic density current with its surroundings (hills and sea). The decoupling of the dense basal part and the dilute cloud is demonstrated at the distal end of the deposits, where successive hills blocked part of the current. The entrance of the current into the 8-km wide strait that separates Okmok from Unalaska Island to the east caused another decoupling. Analyses of the depositional sequences on both islands allow reconstructing the decoupling event and the simultaneous generation of a tsunami by the basal part of the current.

All three chapters were originally written as stand-alone manuscripts, which have been or will be submitted for publication. Chapter 1 is co-authored with Dr. James Gardner, Chapter 2 is co-authored with Prof. George Bergantz, and I am the sole author of Chapter 3. As first author, I was the main contributor behind this work and the instigator of Chapter 2. My coauthors helped to shape the studies with lively discussions, by assisting with experiments, and by editing.

References

Moore JG, Rice CJ (1981) Chronology and character of the May 18, 1980, explosive eruption of Mount St. Helens, *in*: Lipman PW, Mullineaux DR (eds) The 1980 Eruptions of Mount St. Helens, Washington, U.S.G.S. Prof. Paper 1250:133-142.

Nakada S, Shimizu H, Ohta K (1999) Overview of the 1990-1995 eruption at Unzen Volcano, J. Volcanol. Geotherm. Res. 89:1-22.

Nakada S (2000) Hazards from pyroclastic flows and surges, *in*: Sigurdsson H (ed) Encyclopedia of Volcanoes, Academic Press 945-956.

Wolfe EW, Hoblitt RP (1996) Overview of the eruptions, *in*: Newhall CG, Punongbayan RS (eds), Fire and Mud; Eruptions and Lahars of Mount Pinatubo, Philippines, U. Washington Press 3-20.

CHAPTER 1: EXPERIMENTAL CONSTRAINTS ON DEGASSING AND PERMEABILITY IN VOLCANIC CONDUIT FLOW[*]

Abstract

This study assesses dynamical aspects of degassing and permeability in magmas because these processes directly influence the behavior of volcanic eruptions. We describe experiments on hydrated natural rhyolitic glass at high pressure and temperature, which allow assessment of the effect of decompression rate on bubble growth. From the data collected, we define and characterize one growth regime in equilibrium and two regimes in disequilibrium. Equilibrium growth occurs when the decompression rate is slower than 0.1 MPa s^{-1}, while higher rates induce disequilibrium growth. Rates above 0.2 MPa s^{-1} cause porosity to deviate rapidly from equilibrium, defining the first disequilibrium growth regime. If the deviation is large enough, a critical threshold of super saturation is reached and bubble growth accelerates, defining the second disequilibrium regime. We also describe experiments using the same rhyolitic melt in open degassing conditions, which allow determining the onset of bubble connectivity (~43 vol.% porosity). We study coalescence through its profound effect on bubble texture and size distributions, and determine the time scale (~180 s) at which the melt becomes permeable. We parameterize and incorporate our experimental results into a 1D conduit flow model to explore the implications of our findings on eruptive behavior of rhyolitic melts with low crystal contents stored in the upper crust. Compared to previous models that assume equilibrium degassing of the melt during ascent, the introduction of disequilibrium degassing reduces the deviation from lithostatic pressure by ~ 25 %, the acceleration at high porosities (> 50 vol.%) by a factor 5, and the associated decompression rate by an order of magnitude. The integration of the time scale of coalescence to the model shows that the transition between explosive and effusive eruptive regimes is sensitive to small variations of the initial magma ascent speed, and that flow conditions near fragmentation may significantly be affected by connectivity and gas escape.

Introduction

The dynamics of bubble growth, although occurring on a small scale, affect directly the large-scale behavior of volcanic eruptions. Water exsolution into the bubbles is the driving force that controls the growth of bubbles in the volcanic conduit. That growth causes the flow density to decrease, decompression rate to increase, and hence the flow to accelerate, possibly leading to an explosive eruption. Bubbles are present because water supersaturates in the magmatic liquid rising from depth. Since the early work of Sparks (1978), bubble growth dynamics has been explored through increasingly complex numerical models (e.g., Barclay et al. 1995; Lyakhovsky et al. 1996; Proussevitch et al. 1993; Proussevitch and Sahagian 1998; Sparks et al. 1994; Toramaru 1989; 1995) and experimental work (e.g., Gardner et al. 1999; 2000; Mangan and Sisson 2000).

Because of the complex interdependences of the variables involved, many of the processes by which bubbles grow remain unclear. In particular, the relation between growth and decompression rate and the role of bubble connectivity are two poorly constrained processes that directly affect conduit flow dynamics. The highest decompression rates are suggested to arise in the conduit when bubbles grow in equilibrium with the magmatic liquid (Woods 1995). If equilibrium between bubbles and liquid is not maintained, the decrease in density of the mixture is reduced, which minimizes the decompression rate and flow acceleration. Bubble connectivity controls magma permeability, and possibly the transition between explosive and effusive eruptive regimes (Yoshida and Koyaguchi 1999). If magma can become permeable and lose part or all of its gas without fragmenting (Eichelberger et al. 1986), it reduces its porosity, thus limiting further acceleration and possibly leading to effusive eruption.

We describe experiments on hydrated natural rhyolitic glass at high pressure and temperature, which allow us to assess the effect of decompression rate on bubble growth. From the data collected, we define and characterize one growth regime in equilibrium and two regimes in disequilibrium. We also describe experiments using the same rhyolitic melt in open degassing conditions, which allow us to determine the onset of bubble connectivity through its profound effect on bubble texture and size distributions, and to determine the rates at which the melt becomes permeable. Finally, we parameterize and incorporate our experimental results into a 1D conduit flow model to explore the implications of our findings on eruptive behavior. We discuss

the consequences of disequilibrium degassing for conduit flow dynamics, and the role of connectivity in the transition between effusive and explosive regimes.

Methods

We conducted experiments on natural rhyolitic glass from the Panum Crater Dome (PCD; 75.6 wt.% SiO_2 in glass, Mangan and Sisson 2000; Westrich and Eichelberger 1994). Small cores (~ 7 mm length) were filed to fit into 3-mm diameter gold tubing. The tubing was welded shut after adding about 8 wt.% de-ionized water, to ensure super-saturation at run conditions (saturated value: 4.21 wt.% at 150 MPa, this study). Capsules were weighed before and after welding to ensure that no water was lost. Capsules were then placed in an externally heated pressure vessel fitted with a rapid-quench attachment, where they remained at 825 °C and 150 MPa for 5 days to allow the cores to saturate with water.

After the 5-days hydration, one set of samples was decompressed instantaneously to 100 MPa and held for 15 minutes, which ensured the presence of a bubble population in equilibrium with the melt to avoid problems related to nucleation kinetics. The samples were then isothermally decompressed from 100 MPa at rates that increased with lower pressure. Decompression rates were obtained by dropping instantly the appropriate amount of pressure every few seconds in a step-wise fashion to approximate a linear behavior between the pressures of interest. The time step was 20 s for all runs, except for the fastest rates, 1 and 10 MPa s^{-1}, which were obtained by 10 and 3 s steps, respectively. Lowering the sample into the water-cooled base of the vessel after the final decompression step instantaneously quenched the samples.

A second set of samples was quenched at 150 MPa after 5-days hydration. The cores were then reloaded into capsules without water, but with either silicate glass or MgO powder to serve as a sink for expelled water during decompression, allowing open-degassing conditions. The capsules were then reheated to 825 °C and 155 MPa for 5 minutes, decompressed instantaneously to 100 MPa and held for 15 minutes, and finally decompressed at constant rates to lower pressure and quenched instantaneously.

The true diameters of all bubbles within a given volume in thin section were measured using digital images (640×480 pixels) acquired in transmitted light. In the case of the deformed bubbles produced by connectivity, the diameter of a volume-equivalent sphere was taken. The size

distribution of bubbles (BSD) of each sample (~ 150 bubbles) was constructed with three to six images, depending on bubble size. The number density of bubbles (BND) of each sample was calculated using the value of porosity obtained for that sample, following the method of Gardner et al. (1999). Porosities were estimated using similar digital images of thin sections acquired in reflected light. Errors in porosities were estimated from three images for most samples. Bubbles nucleated heterogeneously, in part on the 0.1 vol.% of Fe-Ti oxides present in the melt. Replicate runs show that the nucleated bubbles were similar in number in each experiment. We thus use changes in the BND to monitor for further nucleation and degree of coalescence during decompression.

Experimental results

The instantaneous pressure drop from 150 to 100 MPa at the beginning of each run created a unimodal population of bubbles. Most of these bubbles are attached to crystals, suggesting they nucleated heterogeneously. The number densities of bubbles in all the decompression runs are between 10^5-10^6 cm^{-3}, which confirms the reproducibility of nucleation conditions (Table 1.1). Such densities correspond to a mean bubble diameter of ~35 μm at 100 MPa (ABG1, Table 1.1). The upper part of each sample contains elongated bubbles. This region is more pronounced at low pressure, but is always smaller than a quarter of the total sample height. We avoided this region when making porosity and BSD determinations.

Closed degassing runs

We conducted experiments to assess the maximum decompression rates that permit equilibrium degassing. For each 20 MPa drop, the highest rate that maintained equilibrium was determined (Fig. 1.1). The porosity at equilibrium is calculated from the difference in water saturation between the initial pressure and a given pressure (cf. Equ. (A7) in the *Appendix*). For example, the runs ABG3 and ABG8 were both decompressed in equilibrium (0.1 MPa s^{-1}) down to 60 MPa and then further decompressed to 40 MPa at 0.2 MPa s^{-1} and 0.15 MPa s^{-1}, respectively (Table 1.1). The porosity of the former is less than expected from equilibrium, whereas that of the latter equals equilibrium values. The maximum decompression rate for this increment is thus 0.175 ± 0.025 MPa s^{-1}. We find that the maximum rates that guarantee equilibrium degassing range between 0.125 ± 0.025 MPa s^{-1} at high pressure (60-100 MPa) and 0.175 ± 0.025 MPa s^{-1} at

low pressure (30-60 MPa, Fig. 1.1). We note that slower decompressions would all ensure equilibrium because these rates are maximums, and that they correspond to ascent velocities under a lithostatic load of ~6 m s^{-1}.

We then explored the consequences on bubble growth of a constant decompression rate that exceeds the maximum equilibrium rate. After an initial pressure drop to 100 MPa, we decompressed the runs at constant rates (0.5, 1, and 10 MPa s^{-1}), quenching samples successively in 10 MPa increments (Figs. 1.2 and 1.3). From the successive values of how much porosity deviated from equilibrium, two distinct disequilibrium bubble growth regimes can be defined (Fig. 1.4). A *slow growth rate* regime occurs as the decompression rate first exceeds that of equilibrium. In this regime, porosity increasingly deviates from equilibrium as pressure decreases, but the magnitude of deviation does not change with decompression rate (Fig. 1.3). The slow growth can be illustrated by comparing the mean bubble diameter of a run in disequilibrium with its equilibrium counterpart, correcting for the difference in bubble number densities. At 80 MPa, the mean bubble diameter reaches 38 μm in the slow growth regime (ABG20, Table 1.1) instead of ~48 μm in equilibrium (ABG6). A *fast growth rate* regime occurs where the magnitude of the deviation from equilibrium diminishes and finally vanishes at high porosities. In this regime, the faster pressure decreases, the faster bubbles grow (Table 1.1).

Open degassing runs

We explored the relationship between bubble connectivity and decompression rates, using an experimental setup that allowed open degassing conditions. At slow decompression rates (0.025 MPa s^{-1}), bubble textures change from individual, spherical bubbles to large, distorted bubbles. That change occurred around 43 vol.% porosity, or 32 MPa (Fig. 1.5a, Table 1.2). As developed in the discussion (see the *Connectivity* section below), we interpret this textural change as the consequence of connectivity. At higher pressure, bubbles form unconnected chains that differ strikingly from the random distribution of the bubbles present in closed-degassing runs. At lower pressure, the large coalesced bubbles have deformed shapes with low curvature surfaces. Similar textural changes are observed at higher decompression rates (0.1 MPa s^{-1} and 0.5 MPa s^{-1}, Fig. 1.5b).

Bubble sizes record quantitatively the profound textural changes caused by connectivity (Fig. 1.6a). If we define the start of connectivity when the largest bubbles measured are more than

twice the median size, it occurs between 34 and 30 MPa (41 and 46 vol.%) at 0.025 MPa s^{-1}, between 36 and 30 MPa (40 and 46 vol.%) at 0.1 MPa s^{-1}, and between 30 and 25 MPa (44 and 50 vol.%) at 0.5 MPa s^{-1}. It thus appears that connectivity starts at 43 $\pm$ 3 vol.%, regardless of decompression rate.

Bubble size distributions change dramatically from disconnected to *completely connected* runs (Fig. 1.6a). At low porosity, we note that the size distributions of bubbles in open degassing runs have a similar Gaussian shape, but a broader distribution, than observed in closed system runs (Fig. 1.6b). At higher porosity, large bubble sizes appear in the distribution, which can be better described with a power law spanning up to one order of magnitude (Fig. 1.6c). Distributions of samples with porosities above 60 vol.% are uncertain, because of the low number of bubbles present (Table 1.2). The size distribution thus shifts from Gaussian to power-law as coalescence progresses, but unfortunately, the exact shape of the distribution of completely connected samples cannot be determined with certainty. Nevertheless, the size distributions of completely connected runs seem unchanged by further decompression, despite the high porosities reached (Fig. 1.6a). The bubble number densities of open-system equilibrium runs are similar to closed-system runs and do not significantly vary with coalescence (Table 1.2). We note, however, that the number densities of the disequilibrium runs decrease systematically with decreasing quench pressure.

The pressure range over which connectivity becomes complete increases as the decompression rate increases (Fig. 1.7). At 0.025 MPa s^{-1}, connectivity is complete within an interval of 4 MPa, whereas at 0.5 MPa s^{-1}, connectivity is incomplete after 15 MPa decompression. The completion time for connectivity can be retrieved from the decompression rates and the pressure range. This time seems to be rate-independent and lies between 160 and 180 s (Fig. 1.7). Although coalescence is homogeneous within the main body of a given sample, we observe coalescence to begin at higher quench pressure in the top part of the samples, where elongated bubbles occur (Fig. 1.8). We note that this earlier onset of coalescence of the elongated bubbles occurs regardless of decompression rate.

Discussion

Regimes of bubble growth

The complexity of bubble growth in reaction to a sudden pressure drop is well established (e.g., Proussevitch et al. 1998). Growth caused by a constant decompression rate, however, can be approximated from our experiments by two simple disequilibrium regimes (*slow* and *fast* growth rates, Fig. 1.3). This suggests that one of the main parameters that may vary during these experiments (sample volume, melt viscosity, bubble time delay, super-saturation, and porosity) dominates at a given time. Decompression causes a volumetric expansion of the sample within the gold capsule. We attribute the elongated bubbles present in the upper part of the samples to the shear accompanying this expansion. Because the effect of the shear is confined to a small region of the samples (< 25 vol.%), we conclude that the sample expansion does not influence the average bubble growth. We estimate the viscosities of our experiments to range between 5.9×10^4 at high pressure and 1.5×10^6 Pa s at low pressure (Hess and Dingwell 1996), which are well below the values that affect bubble growth ($\sim 10^{8-9}$ Pa s, Gardner et al. 2000). Our data provide an indirect measure of the amount of water super-saturation, because super-saturation increases with the difference ($\Delta\alpha$) between the equilibrium porosity and the sample porosity (Fig. 1.4). We note that in the slow growth rate regime, super-saturation ($\approx\Delta\alpha$) increases linearly with decreasing pressure regardless of decompression rate (Fig. 1.3). Above a critical value ($\approx\alpha_{cr}$), however, bubble growth accelerates and switches from slow to fast growth regime, quickly becoming faster than the equilibrium rate. This behavior is consistent with the well-known relationship between super-saturation and growth: growth is strongly driven by the amount of excess water, because the rate of water diffusion into the bubble increases with the concentration gradient between the melt and the bubble (Sparks 1978; Proussevitch and Sahagian 1998).

Is super-saturation the main process controlling the two disequilibrium regimes? We note two situations where super-saturation alone cannot explain our data. First, the fastest decompression rate (10 MPa s^{-1}) has a critical value (α_{cr}) much larger than the other rates, whereas this critical value should not depend on decompression rate (Fig. 1.4). We note that the time to reach the critical value is only 4 s for the 10 MPa s^{-1} rate and more than 40 s for the other rates. Bubble time delay, which is a very slow initial growth rate due to unfavorable transport properties of the melt (Proussevitch and Sahagian 1998), may play a role at large decompression rates.

Proussevitch and Sahagian (1998) calculated the bubble time delay for a rhyolitic melt instantly decompressed from 100 MPa to be ~2 s. Our fast rate approximates the instantaneous decompression simulated by Proussevitch and Sahagian (1998), which suggests that the bubble time delay affected the 10 MPa s^{-1} run because of its short duration (4 s). Second, super-saturation alone cannot force $\Delta\alpha$ to vanish at high porosities, thus re-equilibrating melt and bubbles. We suggest this re-equilibration occurs because the spaces between bubbles are reduced at high porosities. In other words, the shell defined by the super-saturation gradient around a given bubble starts to interact with its neighbors, thereby canceling the gradients, as illustrated in the model by Proussevitch et al. (1993). The influence of porosity is therefore confined to the latest stages of the decompression (at low pressure and high porosity), when there is competition between the large decompression rate, which forces disequilibrium degassing, and small bubble spacing, which reduces the length over which water must diffuse.

Our experiments show the effect of disequilibrium decompression rate starting at high pressure (100 MPa). What happens if the decompression starts at lower pressure? We have seen that our experiments, even if decompressed at high rate, are able to reach equilibrium at low pressure (Fig. 1.2). It is possible, however, that a melt suddenly decompressed from low pressures at a high rate (e.g., 50 MPa) could reach the surface out of equilibrium. This is possible because the fast rate occurs only after the critical super-saturation has been reached, as supported by the analytical model of Barclay et al. (1995). Unfortunately, the high porosities involved (> 60 vol.%) make experimental confirmation difficult because the measurement error on porosity increases significantly with porosity value (Table 1.1).

Connectivity

The connection of a few bubbles does not necessarily create a permeable medium; permeability develops only when long bubble chains reach a free surface. If bubbles are large compared to the sample size, however, the chains are only a few bubbles long, and affect the permeability of the sample. This undesirable effect occurs when the ratio of sample diameter to average bubble radius is less than 10 (Blower 2001). In our experiments, this ratio varies between ~100 when connectivity starts and ~20 when connectivity is complete. Thus, the connection of several tens of bubbles is necessary to create an open network in our runs, which is appropriate to study the long-range connectivity in magmatic liquids.

In our experiments, similarly sized bubbles seem to coalesce in two phases. During the first phase, neighboring bubbles start to deform during growth, creating a planar film of liquid between them (Fig. 1.9). The second phase occurs when the thinning film between the bubbles fails. Our smallest measured film thickness is on the order of 1 μm (G303), which suggests that the film disrupts when it reaches a thickness less than 1 μm (Klug and Cashman 1996; Navon and Lyakhovsky 1998). In addition, the film fails when its area is comparable to the cross-sectional area of the bubbles. The newly coalesced bubble presents a deformed shape with low curvature surface. We did not observe the relaxation of coalesced bubbles to spherical shape, most likely because the time needed for such relaxation is on the order of hours at the viscosities considered here (Toramaru 1995).

We observe that bubble coalescence produces a power-law BSD (Fig. 1.6c). Previously, two opposing mechanisms have been proposed to explain the formation of a power-law BSD: cascading coalescence (Gaonac'h et al. 1996) and continuous nucleation (Blower et al. 2001). While the former is accepted for low-viscosity magmas, the latter has been proposed to explain natural size distributions in high-viscosity systems. In our experiments, bubbles did not continuously nucleate during decompression below 100 MPa, as shown by the decrease in number densities with lower pressure and the unimodal size distribution observed in the closed degassing runs. Instead, the concurrence of bubble coalescence (Fig. 1.9) with the decrease of number densities with lower pressure and the shift from Gaussian to power-law size distributions in the open degassing runs are more consistent with cascading coalescence. These observations suggest that cascading coalescence may be applicable to high-viscosity melts.

Beyond supporting a particular mechanism of coalescence, we believe our observations shed light on three other aspects of this process. First, coalescence generates broad bubble size distributions with large bubbles coexisting with bubbles 20 times smaller (Fig. 1.6c). Second, the observed power-laws, although limited to one order of magnitude, seem to be characteristic of *ongoing* coalescence. Third, it is likely that high porosities were achieved even at low decompression rates (e.g., 85 vol.% for PPE11, Table 1.2), because the amount of gas that could escape was finite, given the finite volume of the capsule and the limited capacity of absorption of the anhydrous material. This is consistent with the fact that the completely connected runs are the result of a single event of pairing coalescence, which produces a new BSD (e.g., PPE11 in Fig. 1.6a). As a result, bubbles would collapse to the observed distorted shapes after releasing a

fraction of their gas, and the system would be ready for a second coalescence event. Thus, any initial BSD is likely to be obscured by the succession of processes (variable amounts of coalescence, shear, fragmentation, post-fragmentation processes) that occur during magma ascent, limiting in our view the usefulness of interpretations given to BSD based upon natural samples.

Perhaps more interesting is the comparison of BSD between closed degassing runs and the equivalent open degassing runs at low coalescence, which both produce similar Gaussian shapes (Fig. 1.6b). For comparison, we correct the difference in median bubble diameter ($\sim 17 \mu m$) between the runs, which results from differing bubble number densities. The BSD of the closed degassing run is narrow, with a standard deviation less than 20%, and no measured bubbles below 35 μm or above 88 μm. In contrast, the BSD of the open degassing run has a deviation greater than 30% with bubbles as small as 14 μm, and as large as 147 μm. Whereas the larger bubbles are produced by coalescence, the smaller bubbles could result from either nucleation of new bubbles, by-products of coalescence, or hindered growth. The occurrence of a new nucleation event during decompression is unlikely, because of the unimodality of the closed-run BSD and the low decompression rates applied. A small bubble created as by-product of coalescence would result from the closedown of the bottleneck junction between two newly coalesced bubbles of different sizes. This situation occurs when the surface tension dominates the viscous forces of the liquid, but the planar shape of the observed thin films between neighboring bubbles does not favor this hypothesis. Experimental work on the interaction of bubbles with large size difference (ratio 1:4) shows that the concentration gradient field set by a large bubble tends to hinder and even reduce the size of smaller neighboring bubbles (Larsen and Gardner 2000). The size ratio between the small bubbles and their coalesced neighbors is on the order of 1:100 in our experiments. Thus, hindered growth seems the most likely process to control the apparent small bubbles.

We can use our experiments to identify some of the parameters on which on-going connectivity depends. We have seen that connectivity is time dependent, regardless of decompression rate. Most likely, connectivity is incomplete for the faster decompression rate because the time allowed for connection decreases as decompression rate increases whereas the time needed for bubbles to connect into long chains is finite. The early coalescence observed in

the upper part of the samples can be linked to the catalyzing role of shear on coalescence (Stasiuk et al. 1996).

A perhaps more fundamental problem is to identify the cause(s) of coalescence in the open degassing runs. The importance of viscosity and the spatial arrangement of bubbles as controlling factors of coalescence and permeability have been discussed by many authors (e.g., Proussevitch et al. 1993; Gaonac'h et al. 1996; Blower 2001). Viscosities are expected to be similar for both open and closed degassing samples, but coalescence is manifest only in the open degassing set. Our experiments generate similar BSD and BND at high pressure for both sets (Fig. 1.6b). Hence, we expect similar spatial arrangement of bubbles, as well as similar nucleation and growth kinetics. The major difference between the two sets seems to be the volatile concentration gradient at the sample free surface that extends on a much larger scale than the average bubble diameter. The effect of this concentration gradient on coalescence will be the object of a further study.

Implications for volcanic eruptions

Conduit flow model

Water exsolution into bubbles drives bubble growth, and whether exsolution occurs in equilibrium influences conduit flow dynamics. Although one study explored the consequence of disequilibrium degassing on bubble overpressure (Melnik 2000), no quantitative assessment of the dynamic effects of disequilibrium has been performed. Qualitatively, in disequilibrium the density decrease and viscosity increase caused by bubble growth are diminished, which reduce the decompression rate and flow acceleration. Our experimental results for closed degassing allow a quantification of the decompression rates in which equilibrium is maintained. We have thus used a one-dimensional model of magma ascent to explore further the consequences of disequilibrium degassing. Details of the model are given in the *Appendix*.

Our model of magma ascent assumes steady, isothermal, and homogeneous flow in a vertical cylindrical conduit (e.g., Wilson 1980). We solve the momentum equation along the conduit as magma rises, allowing viscosity to vary (Dobran 1992; Papale and Dobran 1993; Woods 1995; Mastin and Ghiorso 2000). We develop empirical relations between pressure, decompression, and porosity for each regime of bubble growth (Fig. 1.4), thus allowing disequilibrium degassing.

Results

The comparison between a run of the model with forced equilibrium degassing and with disequilibrium degassing according to our empirical relations is shown in Fig. 1.10. Initial conditions for both runs are the same as in the experimental sets (825 °C, 150 MPa, water-saturated, 2154 kg m^{-3} from Mastin and Ghiorso 2000). A representative mass flux (2.19×10^6 kg s^{-1} for 20-m diameter conduit) was determined by running a similar 1D equilibrium-degassing model (*Conflow*, Mastin and Ghiorso 2000) that simulates flow conditions after fragmentation and matches a non-choked boundary condition at atmospheric pressure at the vent. In the equilibrium degassing run, we note deviations from lithostatic pressure, strong accelerations at high porosities (e.g., 4.7 m s^{-2} at 60 vol.%; 30 m s^{-2} at 70 vol.%), and associated large decompression rates (e.g., 15.4 MPa s^{-1} at 60 vol.%; 47.6 MPa s^{-1} at 70 vol.%), as found in similar works (Dobran 1992; Papale 1999; Mastin and Ghiorso 2000). As expected, disequilibrium degassing greatly reduces deviations from lithostatic pressure, produces only modest accelerations at high porosities (e.g., 0.97 m s^{-2} at 60 vol.%; 5.4 m s^{-2} at 70 vol.%), and greatly reduces decompression rates. Indeed, at porosities above 60 vol.%, decompression rates are reduced by an order of magnitude. These reductions of flow acceleration and decompression rate are more important if the values are compared at a given pressure instead of a given porosity.

Fragmentation depths defined by porosity are commonly used by conduit flow models (e.g., Jaupart and Allegre 1991; Mastin and Ghiorso 2000). We note that the fragmentation depth defined as such occurs significantly shallower with disequilibrium degassing (1 km higher in Fig. 1.10). We also note that an estimate of the effect of delayed nucleation (or melt super-saturation, Woods 1995) had a similar effect. Fragmentation depth as defined by a specific value of porosity (e.g., 67-80 vol.%: Sparks 1978; ~64 vol.%: Gardner et al. 1996; 75 vol.%: Mastin and Ghiorso 2000) is thus highly sensitive to the rate of the different processes occurring in the conduit.

The introduction of disequilibrium degassing in the conduit flow model induces a drastic reduction of the deviation from lithostatic pressure, flow acceleration, and decompression rate at high porosities. In other words, flow conditions near fragmentation are not as extreme as previously thought (Dobran 1992; Sparks et al. 1994), and our model allows us to quantify the consequences of this change for three different fragmentation criterions. First, in the case of sudden decompression of highly viscous magma (e.g., dome failure), fragmentation has been

experimentally determined to require a pressure drop on order of 10^2-10^4 MPa s^{-1} with a magma viscosity between 10^8 and 10^{10} Pa s (Alidibirov and Dingwell 2000). We predict both decompression rates and viscosities one to two orders of magnitude *below* the required values, confirming the inapplicability of this fragmentation criterion in the case of a conduit-driven eruption. Second, overpressure in the bubble has been proposed to be the cause for fragmentation (Navon and Lyakhovsky 1998; Zhang 1999; Melnik 2000; Alidibirov and Dingwell 2000). Melnik (2000) uses a working value of 10 bar, arguing the exact overpressure to be secondary because of its exponential increase above 60 vol.% porosity. Using the Rayleigh-Lamb equation (equation 6 in Melnik 2000), we calculated with the initial conditions used in Fig. 1.10 that an overpressure of 10 bar is reached at 87 vol.% porosity in the equilibrium degassing case, and at 83 vol.% in the disequilibrium case. We also observe that the exponential behavior is similar in both cases. Fragmentation by bubble overpressure thus gives similar results between equilibrium and disequilibrium degassing, yet at values much greater than for most pumice vesicularities (Gardner et al. 1996). The third criterion, fragmentation based on strain rate (e.g., Papale 1999), uses a mathematical formulation equivalent to bubble overpressure (Melnik 2000), but with different physical variables. Using the elastic modulus given by Papale (1999), we calculated with the initial conditions used in Fig. 1.10 that magma viscous dissipation is overcome at 80 vol.% porosity in both equilibrium and disequilibrium degassing cases. Thus, despite significant changes in flow conditions near fragmentation, the strain-rate fragmentation criterion is insensitive to the degassing style.

The robustness of our empirical approach of disequilibrium degassing can be assessed by comparing the effects produced by two independent sets of internally consistent data. For example, the decompression experiments of Gardner et al. (1999) were run under similar conditions as our closed degassing experiments. High-silica rhyolite with low crystal content (< 1 vol.%) was heated at the same temperature (825 °C) and linearly decompressed at various rates. The higher initial confinement pressure (200 MPa) allows a qualitative extension of our model to a broader range of initial conditions. Keeping in mind that the Gardner et al. (1999) decompressions start from initial, water-saturated pressure, and therefore that these runs include nucleation kinetics, we can extend the empirical formulation of the slow growth rate regime (Equ. (A11)). A regression including both experimental sets gives a coefficient (A_z) 20 % higher than the one determined from 150 MPa, and slightly increases the correlation coefficient (Table 1.3).

The regression of both sets on the boundary between the slow and fast growth regimes (Equ. (A14)) changes the coefficients (a_i and b_i) by less than 1 %, and slightly lowers the correlation coefficient (Table 1.3). The extension of the comparison to the fast growth regime is not possible due to the lack of data towards lower pressures for runs initiated at 200 MPa. Runs of the disequilibrium model with identical initial conditions, but with the coefficients determined from both data sets, are indistinguishable on the scale of Fig. 1.10. Thus, our empirical approach shows little sensitivity to initial confining pressure, nucleation kinetics at low crystal volume fraction, and small differences in melt composition.

The effect of connectivity

In a volcanic conduit, the creation of an open network would allow gas to escape from the magma. The ensuing diminution of porosity would reduce flow acceleration and possibly lead to effusive eruption (Eichelberger et al. 1986; Jaupart and Allegre 1991). On the other hand, the high porosities needed for fragmentation may only be reached if bubble connection is incomplete. Thus, it seems that fast decompression rates are required for explosive eruption (see sections *Open degassing runs* and *Connectivity*). We therefore used the conjunction of our model and the experimental results on connectivity to assess the transition between effusive and explosive regimes.

We performed numerical runs varying only the initial ascent speed of magma (Fig. 1.11), and superimposed the results of the connectivity experiments. From the open degassing experiments, we consider that connectivity is rate-independent, begins at 32 MPa (43 vol.% porosity in equilibrium), and is complete after 180 s. We set the fragmentation porosity to 64 vol.% (Gardner et al. 1996). If the magma reaches 64 vol.% porosity more than 180 s after reaching 43 vol.%, then it erupts effusively.

We find that the critical ascent rate is modest, 0.35 m s^{-1}, which corresponds to a mass flux of 2.4×10^5 kg s^{-1}, and that only runs below 0.30 m s^{-1} occur completely in the equilibrium-degassing regime. At those conditions, a variation of 0.1 m s^{-1} reduces or expands the time allowed for complete connection by about one minute, with a roughly linear dependence between initial ascent rate and connectivity completion. Although we set the fragmentation porosity to 64 vol.%, raising it to the commonly used value of 75 vol.% (Sparks 1978) would only increase slightly the initial magma ascent rate, but not change this linear dependence. This dependence between ascent

rate and connectivity suggests that the transition from effusive to explosive regime is very sensitive to initial ascent rate.

Because our model does not allow the gas to escape from the magma, the numerical runs are maximum estimates of ascent speeds for open degassing systems. The effect of connectivity, however, can be assessed with an open-system conduit flow where the gas can flow within bubble chains (Yoshida and Koyaguchi 1999). After adjusting the parameters of the model (Equ. 37 in Yoshida and Koyaguchi 1999) to match our values of porosity and pressure at the onset of connectivity, the porosity reached at fragmentation pressure (~17 MPa) if the gas escapes from the bubbles is 51 vol.% instead of the 64 vol.% value we imposed. The magma takes about one minute less (76 s) to reach the corrected 51 vol.% porosity. The linear relationship between ascent rate and connectivity indicates that our closed-degassing model overestimates the critical ascent rate by 0.1 m s^{-1}, leading to a corrected rate of 0.25 m s^{-1}. This corrected estimate is still a minimum, however, because the progression of connectivity is buffered by the decrease in porosity caused by gas escape, as magma permeability is a function of porosity (Blower 2001). Therefore, the critical ascent rate lies between 0.25 and 0.35 m s^{-1}, and our simplified model correctly shows that the transition between explosive and effusive regimes is sensitive to small differences in initial ascent rate.

Superimposing the results of the open degassing experiments to our model leads to two additional conclusions. First, the assumption of closed-system for conduit model can be applied at large magma ascent speeds and high mass fluxes (e.g., Plinian eruptions), but should be restricted to high pressures (> 32 MPa) and low gas volume fractions (< 43 vol.%) at low ascent speeds (e.g., lava dome). Second, our estimate of 43 vol.% porosity for the onset of connectivity is a maximum, because the shear present in the conduit enhances the efficiency of coalescence, which increases the time for gas to escape. The time scale of 180 s given for connectivity is thus a maximum, and hence flow conditions near fragmentation may significantly be affected by connectivity and gas escape.

Conclusions

Decompression experiments performed on rhyolitic melt hydrated at 150 MPa and sub-liquidus temperature lead us to define three distinct bubble growth regimes. An *equilibrium regime* occurs when the melt initially decompresses slow enough (< 0.1 MPa s^{-1}) to allow water to completely

diffuse from melt to bubbles. The *slow rate regime* occurs when the melt decompresses faster than equilibrium (> 0.2 MPa s^{-1}). In this regime, porosity evolves linearly with pressure, regardless of decompression rate. A *fast rate regime* occurs when the super-saturation reaches a critical value, which does depend on decompression rate, and accelerates bubble growth. The fast growth diminishes the porosity deviation from equilibrium linearly with pressure decrease.

The consequences of the three growth regimes on conduit flow dynamics were assessed by a one-dimensional modeling of magma ascent fitted by the experimental data. Compared to previous models that assume equilibrium degassing of the melt during ascent, the introduction of disequilibrium degassing reduces the deviation from lithostatic pressure by ~ 25 %, the acceleration at high porosities (> 50 vol.%) by a factor 5, and the associated decompression rate by an order of magnitude. Importantly, flow conditions near fragmentation are not as extreme as previously thought. Comparison with other published decompression experiments (Gardner et al. 1999) shows that our empirical approach is valid for rhyolitic ($10^4 - 10^7$ Pa s) melts with low crystal contents (< 1 vol.%) stored in the upper crust (< 10 km).

Experiments run under open degassing conditions show that bubble connectivity starts around 43 vol.% porosity, regardless of decompression rate. Connectivity is time-dependent and occurs in a matter of minutes (~ 180 s). Introduction of these results into our model shows that the transition between explosive and effusive regime is sensitive to small variations of initial magma ascent speed (on the order of 0.01 m s^{-1}). The assumption of closed-system for conduit flow models is restricted to porosities lower that 43 vol.%, but can be extended to higher porosities in the case of high mass fluxes. Flow conditions near fragmentation, however, may significantly be affected by connectivity and gas escape.

Acknowledgments

Table 1.1 Experimental conditions for closed degassing experiments.

run[a]	decompression rate[b] (MPa s^{-1})	quench pressure (MPa)	porosity[c] (vol.%)	bubble mean diameter[c] (μm)	number of bubbles	BND[d] ($\times 10^5$ cm^{-3})
ABG1	-	100	5.6 (0.2)	35 (7)	149	18
ABG6	0.1	80	13.3 (1.1)	60 (14)	173	10
ABG4	0.15	80	6.4 (0.7)	34 (7)	170	29
ABG2	0.1	60	21.8 (0.8)	60 (11)	127	17
ABG7	0.15	60	17.5 (1.3)	49 (9)	162	25
ABG8	0.1 (100-60) 0.15 (60-40)	40	33.0 (2.3)	67 (16)	165	17
ABG3	0.1 (100-60) 0.2 (60-40)	40	26.9 (4.5)	103 (16)	163	4
ABG9	0.1 (100-60) 0.15 (60-30)	30	49.7 (2.3)	109 (22)	145	6
ABG11	0.1 (100-60) 0.15 (60-40) 0.2 (40-30)	30	34.5 (2.7)	71 (13)	154	16
ABG20	0.5	90	5.5 (1.2)	34 (7)	169	22
ABG14	0.5	80	6.7 (0.2)	38 (6)	152	22
ABG25	0.5	70	12.3 (1.4)	61 (11)	157	91
ABG15	0.5	60	19.1 (1.3)	63 (9)	163	14
ABG16	0.5	50	23.9 (0.4)	71 (8)	167	11
ABG30	0.5	30	44.2 (0.8)	60 (11)	145	35
ABG32	0.5	10	78.8 (1.7)	140 (32)	48	5
ABG26	1	70	10.4 (0.9)	36 (7)	193	40
ABG27	1	60	17.0 (1.1)	35 (8)	167	56
ABG28	1	50	23.5 (1.2)	56 (8)	163	25
ABG31	1	40	29.3 (1.2)	51 (12)	167	15
ABG29	1	30	42.2 (1.2)	77 (14)	61	32
ABG33	10	40	22.0 (0.8)	59 (11)	183	18

[a] All runs were hydrated at 825 °C for 5 days.
[b] When applicable, decompression rates are given with the corresponding pressure ranges in parenthesis.
[c] Porosities and bubble mean diameters are given with ± 1 σ in parenthesis.
[d] BND are bubble number densities.

Table 1.2 Experimental conditions for open degassing experiments.

run[a]	decompression rate (MPa s^{-1})	quench pressure (MPa)	porosity[b] (vol.%)	bubble mean[b] diameter (μm)	number of bubbles	BND[c] ($\times 10^5$ cm^{-3})
PPE6	0.025	60	39.2 (2.0)	176 (39)	27	1.2
PPE2	0.025	44	46.1 (1.9)	218 (57)	39	0.6
PPE4	0.025	40	51.2 (4.8)	111 (16)	127	5.8
PPE5	0.025	36	52.8	226 (71)	27	0.5
PPE7	0.025	34	63.2	143 (33)	89	3.8
PPE1	0.025	30	30.2 (8.1)	124 (119)	37	0.4
PPE10	0.025	28	62.3 (10.1)	302 (102)	18	0.4
PPE11	0.025	24	85.3 (2.6)	385 (152)	12	0.2
G318	0.1	36	44.0	106 (49)	61	5.4
G322	0.1	30	41.3	90 (108)	50	0.9
G321	0.1	24	43.3 (4.7)	81 (15)	135	13.7
G323	0.1	18	50.1	113 (62)	92	3.0
G300	0.5	30	35.2	77 (25)	107	11.0
G303	0.5	25	42.4 (4.8)	62 (42)	136	8.9
G327	0.5	20	52.9 (4.7)	65 (52)	152	6.8
G328	0.5	15	62.2 (2.0)	72 (77)	166	3.6

[a] All runs were hydrated at 825 °C for 5 days.

[b] When available, porosities and bubble mean diameters are given with $\pm$ 1 σ in parenthesis.

[c] BND are bubble number densities.

Table 1.3 Empirical constants.

	A_z	R^2	a_1	b_1	R^2	a_2	b_2	R^2
this study	-5.3×10^{-6}	0.73	0.256	1.567	0.95	2.36×10^{-11}	6.46×10^{-10}	0.99
this study & Gardner et al. (2000)	-6.8×10^{-6}	0.98	0.258	1.549	0.75	n.a.	n.a.	n.a.
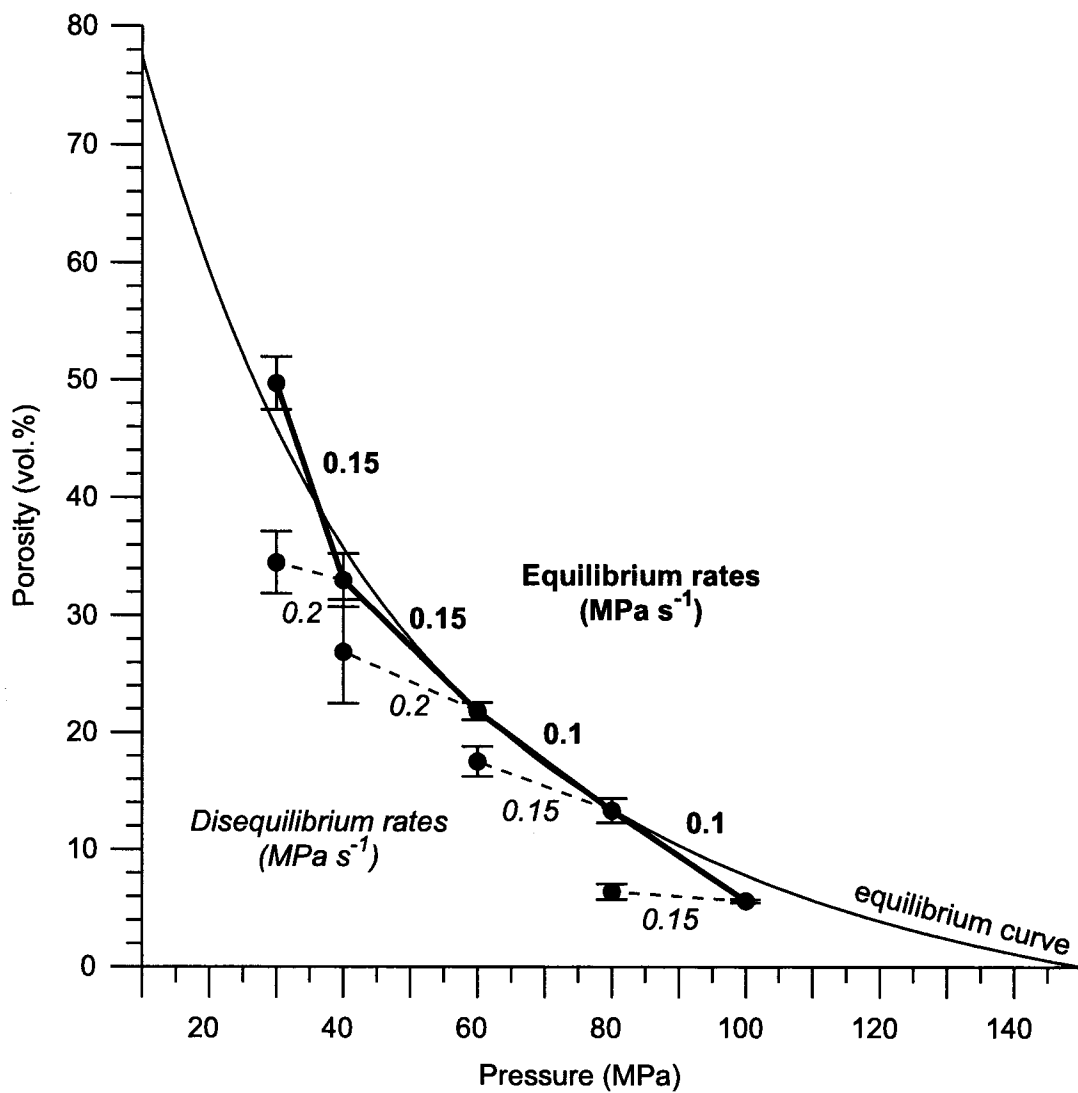
Figure 1.1 Porosity as a function of quench pressure for variable decompressions rates. Dashed lines indicate disequilibrium degassing over a given pressure interval, and solid lines indicate equilibrium degassing over the interval. The equilibrium degassing porosity curve is calculated from Equ. (A7) (see text for details).
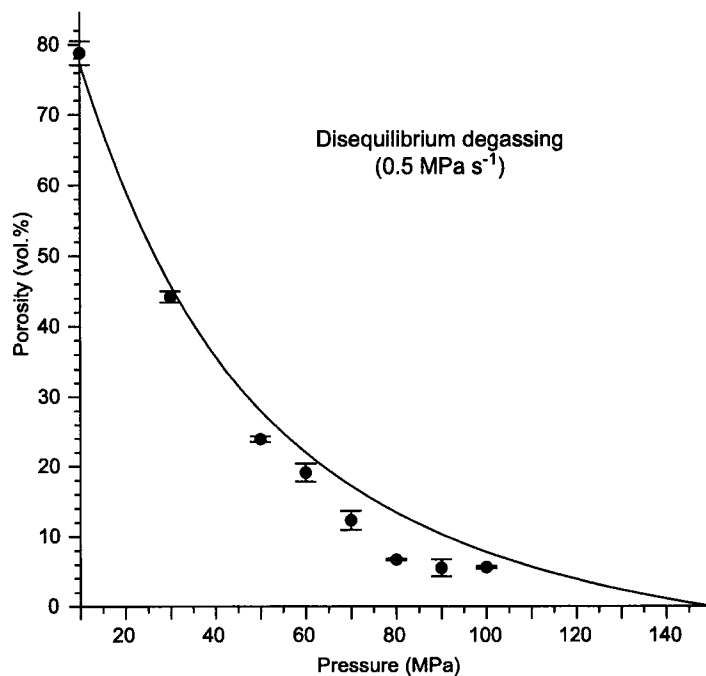
Figure 1.2 Porosity as a function of quench pressure for a constant decompression rate of 0.5 MPa s^{-1}. The imposed rate forces disequilibrium degassing, as illustrated by the deviation of the sample porosities from the equilibrium curve (calculated from Equ. (A7)).
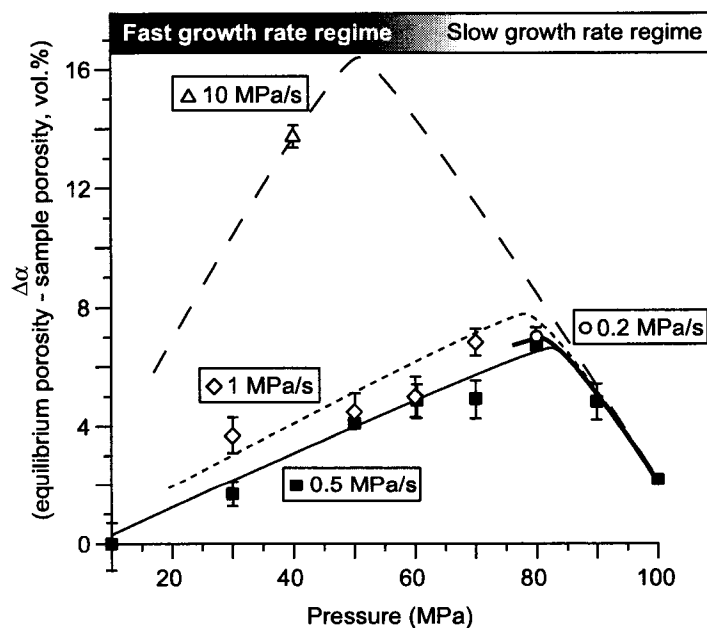
Figure 1.3 Porosity deviation from equilibrium degassing ($\Delta\alpha$) for various linear decompression rates. Error bars are omitted when smaller than the symbol size.
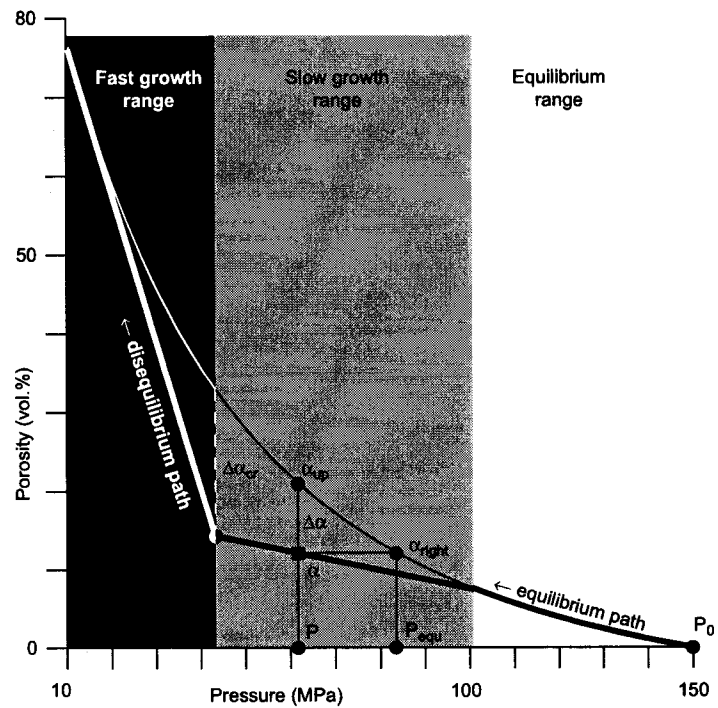
Figure 1.4 Definition of the variables used in the description of disequilibrium degassing runs and in the conduit flow model.
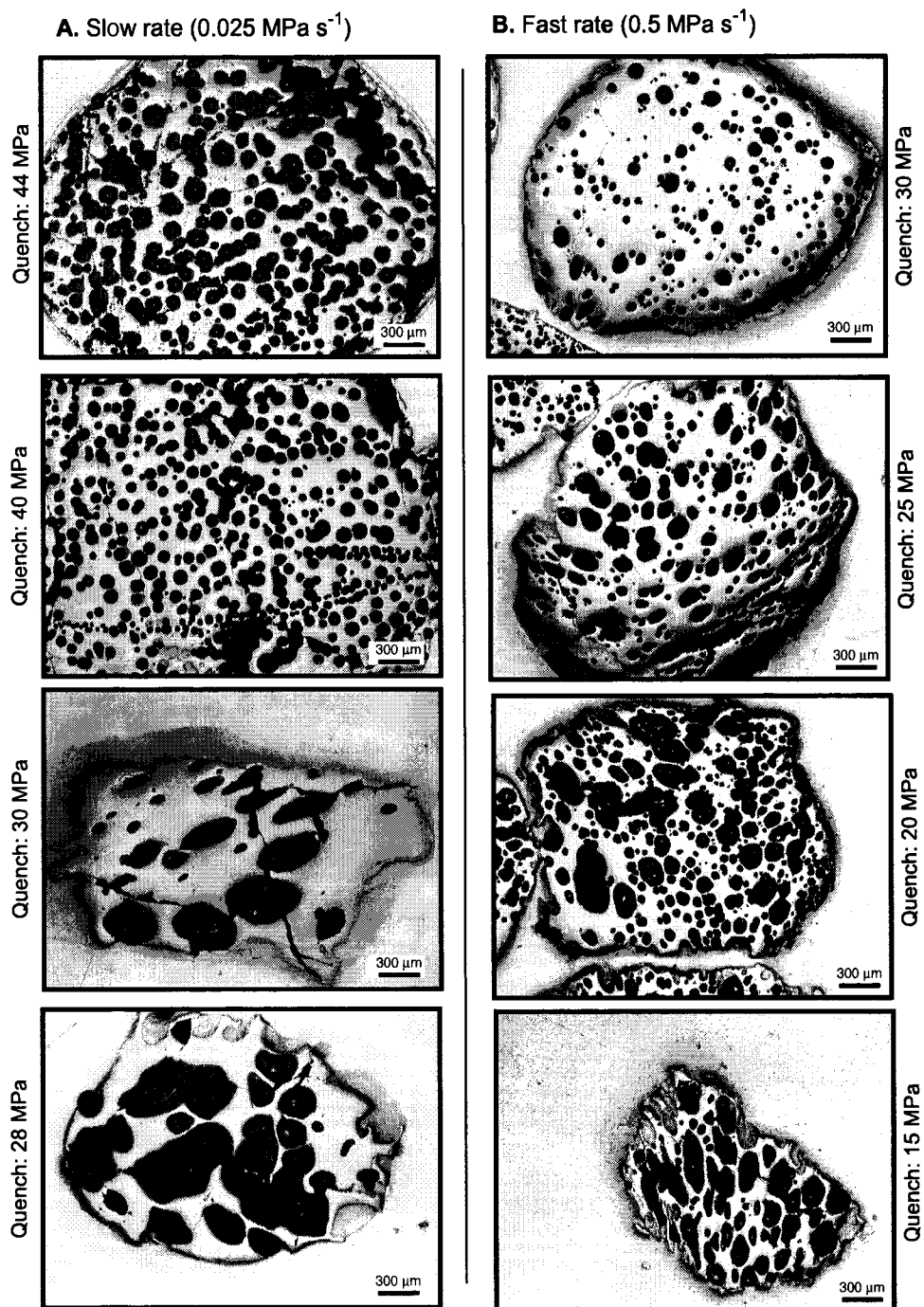
Figure 1.5 Microphotographs of thin sections in reflected light showing decompression runs with open-degassing conditions. **a.** Linear decompression rate of 0.025 MPa s^{-1}. Connectivity is responsible for the textural change occurring between 40 and 30 MPa. **b.** Linear decompression rate of 0.5 MPa s^{-1}.
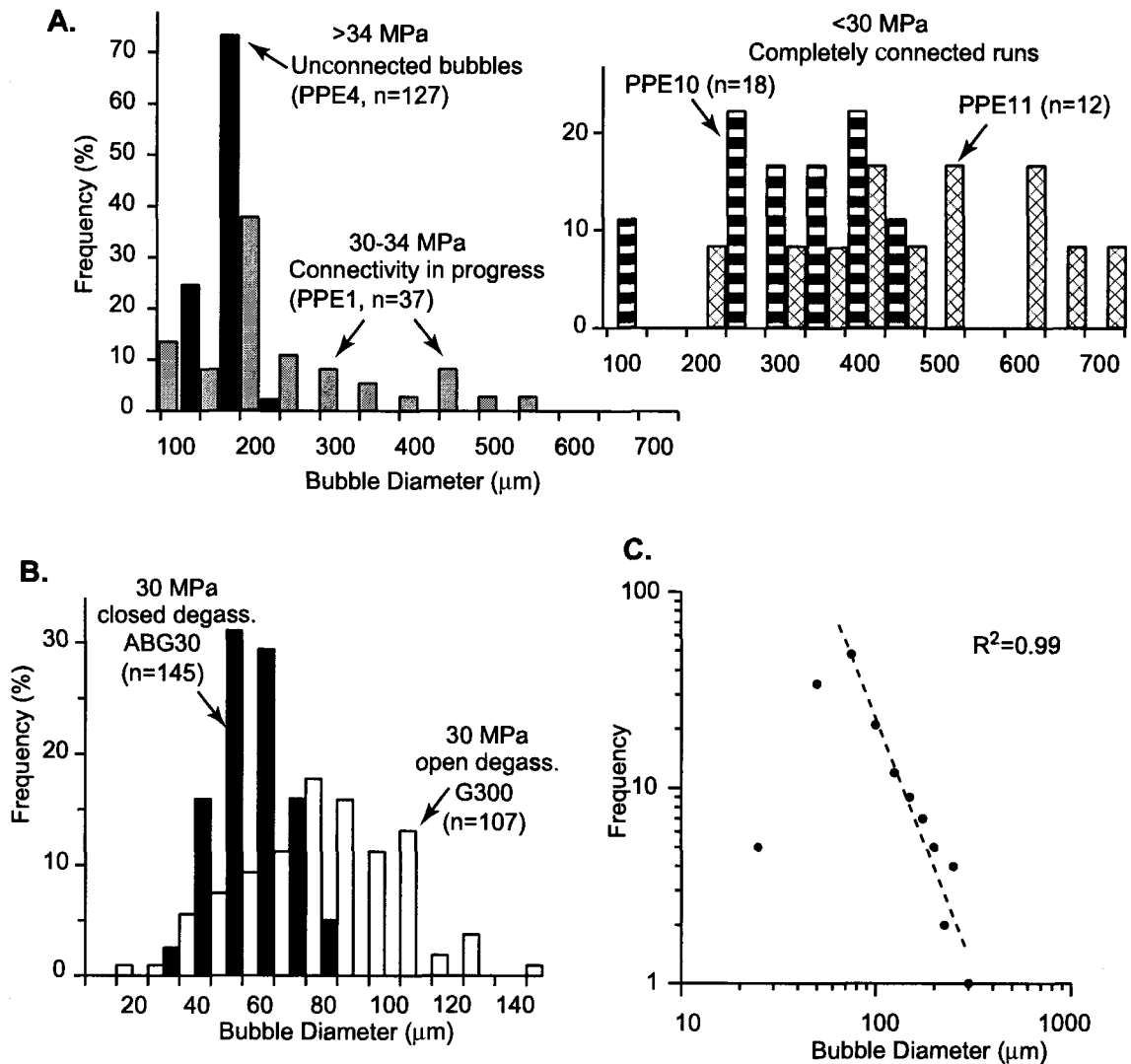
Figure 1.6 Bubble size distributions (BSD) of open degassing experiments showing the effects of coalescence. **a.** Coalescence from inception (PPE4) to in-progress (PPE1) to completion (PPE10) at low decompression rate (0.025 MPa s^{-1}). Note the few changes induced by further decompression after complete connection (PPE11), and the low bubble count of connected sample due to large bubbles. **b.** Open degassing conditions produce broader distributions (G300, 0.5 MPa s^{-1}, median diameter = 77 μm, σ = 25, BND = 11×10^5 cm^{-3}) than closed degassing conditions (ABG30, 0.5 MPa s^{-1}, median diameter = 60 μm, σ = 11, BND = 35×10^5 cm^{-3}). **c.** On-progress coalescence creates large bubbles and produces a power-law coarse-tail distribution (G327, 0.5 MPa s^{-1}).
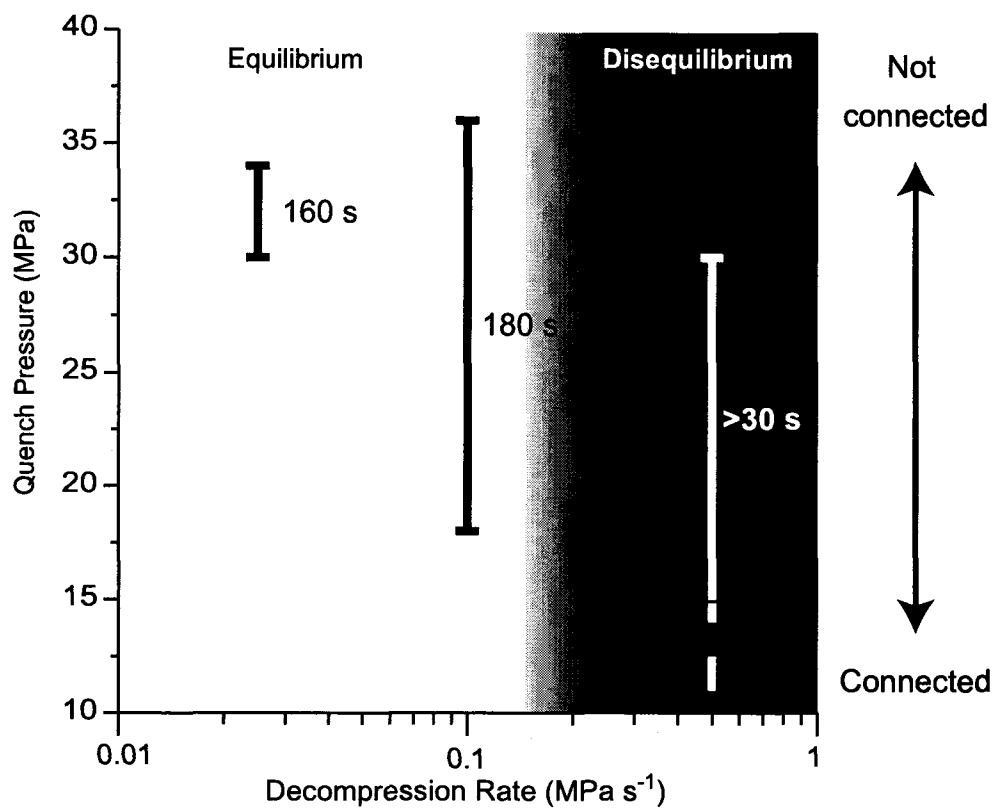
Figure 1.7 Coalescence start and completion in function of the quench pressure. Also shown are time estimates to complete connectivity for various decompression rates.

Figure 1.8 Reflected light microphotograph of an open degassing run showing the catalyzing effect of shear on coalescence. Note that the large, coalesced bubbles are restricted to the upper half of the photograph. The photograph corresponds to the upper 2 mm of the sample (G318, Table 1.2).

Figure 1.9 Typical bubble pair shortly before coalescence. Note the planar shape of the thin separation wall between the bubbles (G303, Table 1.2).
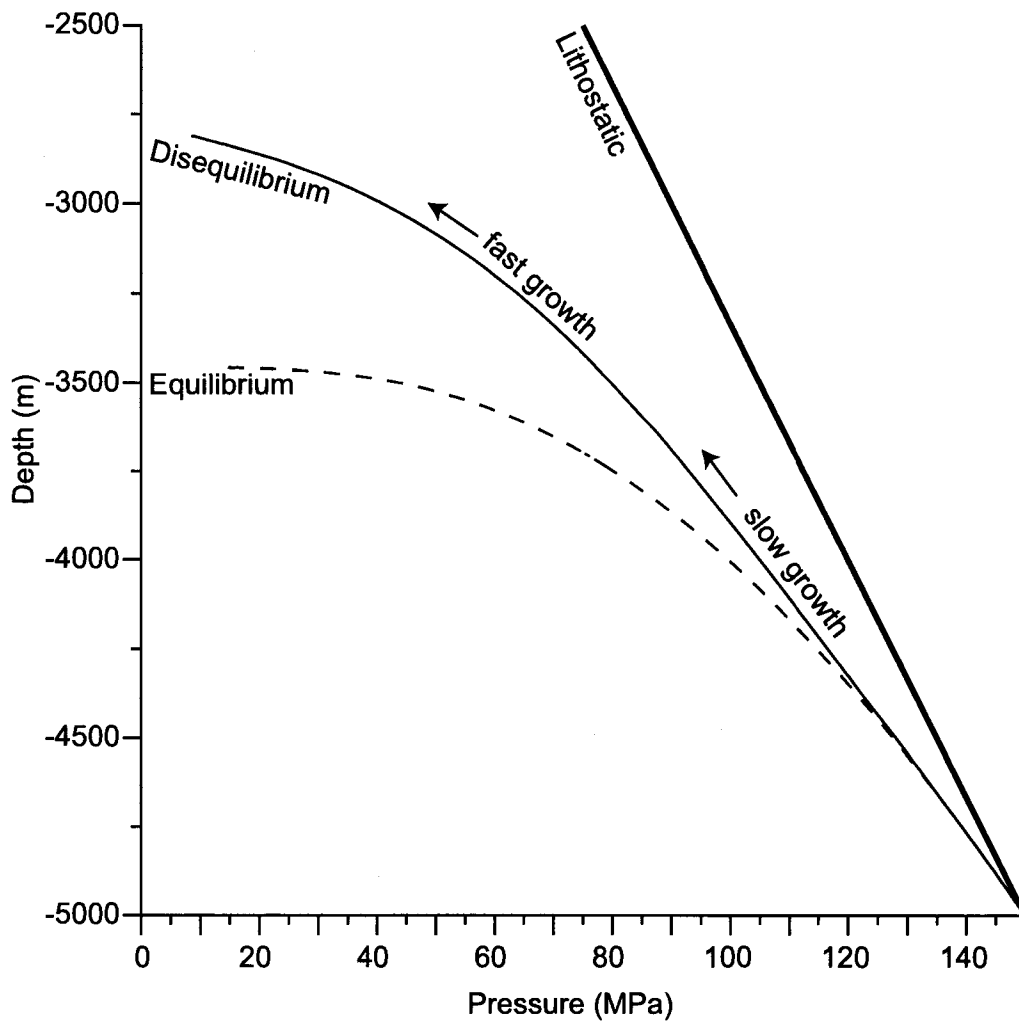
Figure 1.10 Comparison of pressure-depth variations of one-dimensional conduit flow models with and without equilibrium degassing. Initial conditions are the same for both runs: $P = 150$ MPa, $\rho_l = 2154$ kg m^{-3}, $T = 825$ °C, $Q = 2.19\times10^6$ kg s^{-1}, $R = 10$ m. The solid line represents equilibrium degassing, the stippled line disequilibrium degassing, and the thick line the lithostatic pressure gradient.
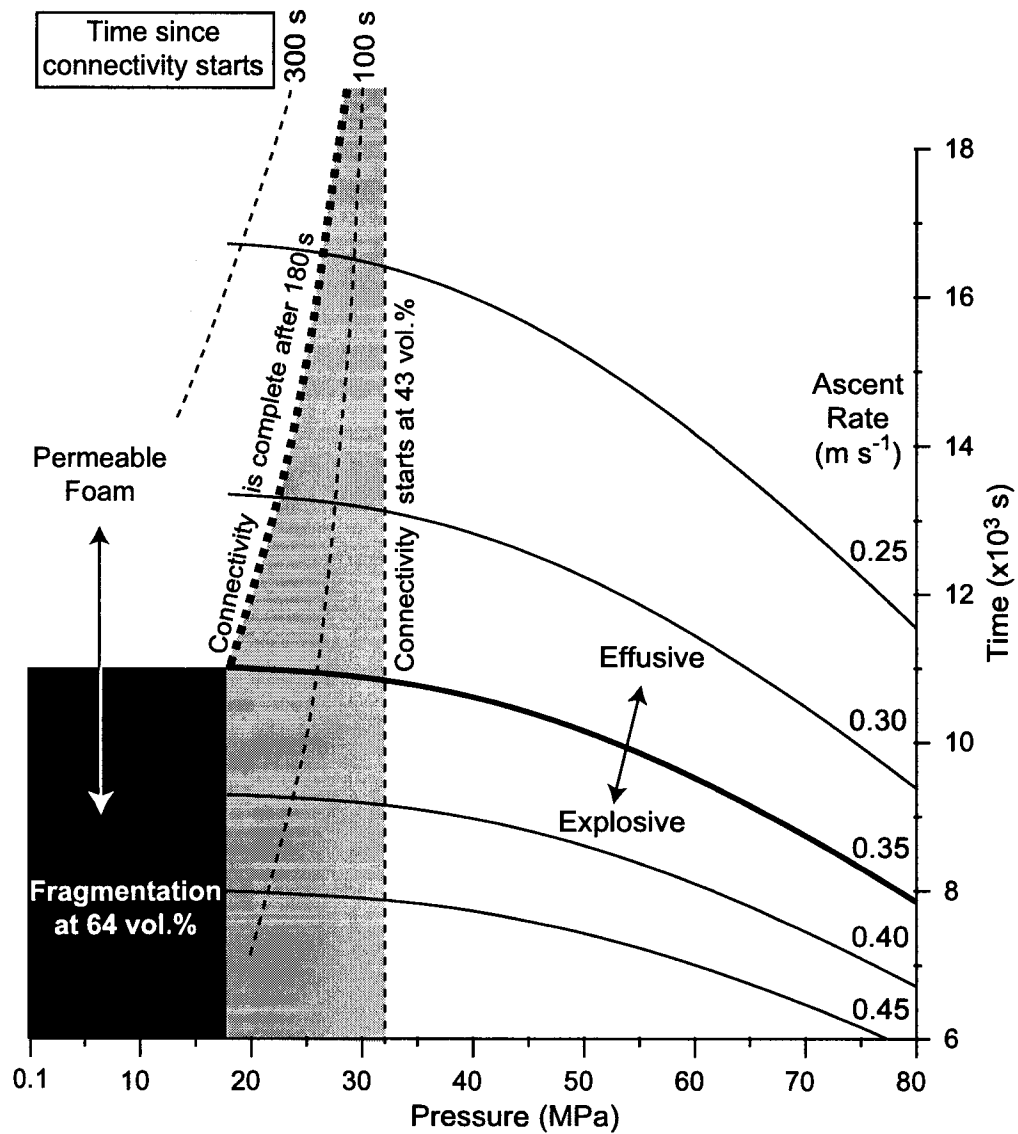
Figure 1.11 The effect of magma initial ascent rate on the transition between effusive and explosive eruption. Values of the *y-axis* correspond to the time since the beginning of magma ascent. Initial conditions are: $P = 150$ MPa, $\rho_l = 2154$ kg m^{-3}, $T = 825$ °C, $R = 10$ m, and bubble connectivity occurs at 43 vol.% porosity (32 MPa) and is complete after 180 s. The magma will fragments at ~64 vol.% porosity only if there is gas remaining, i.e., if connectivity is incomplete.
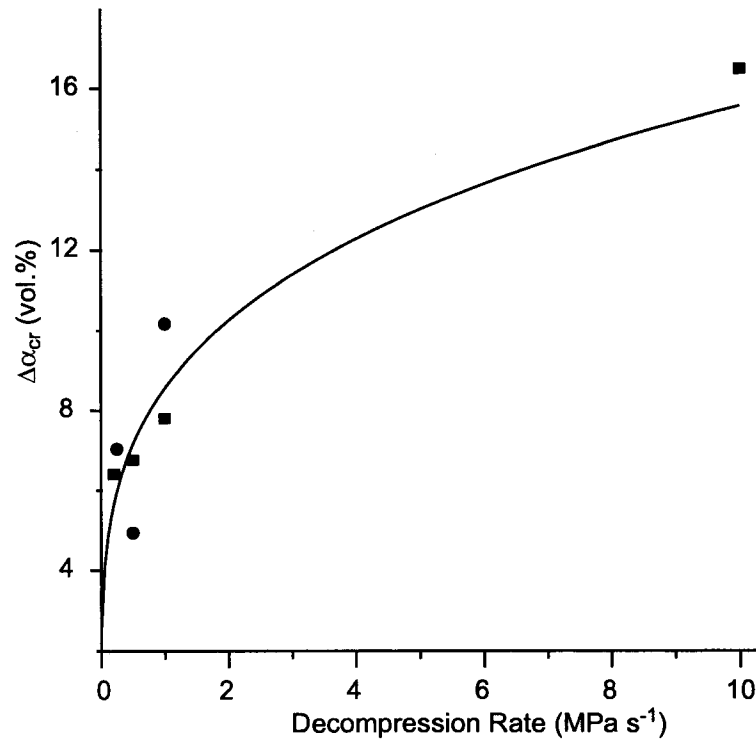
Figure 1.A1 Nonlinear regression of $\Delta\alpha_{cr}$ (maximum porosity deviation from equilibrium degassing) in function of the decompression rate. Circles are data from Gardner et al. (1999) and squares are data from this study.

Appendix 1

In our one-dimensional model of magma ascent, flow properties are averaged across the cross-sectional area of the conduit at any given depth. We assume that the flow is isothermal and homogeneous (i.e., bubbles rise at the same speed as the magma), the conduit is a vertical cylinder with impermeable rigid walls, and the gas phase is H_2O. In similar experimental conditions, Gardner et al. (1999) showed that bubble growth by expansion to lower pressure account for a small fraction ($\sim$ 5 %) of the total growth. Thus, we assume bubble growth to be caused solely by water diffusion into the bubble. We consider that the mass flux Q remains constant, so that:

$$Q = \rho \pi r^2 v \qquad\qquad\qquad (A1)$$

where ρ is the mixture density, v its speed, and r the conduit radius (see Table 1.A1 for symbol definition). Conservation of mass and momentum are solved along the conduit as magma rises:

$$\frac{d(\rho v)}{dz} = 0 \tag{A2}$$

$$\rho v \frac{dv}{dz} = -\frac{dP}{dz} - \rho g - \rho v^2 \frac{f}{r} \tag{A3}$$

where P is the magma pressure, g the acceleration of gravity, and f a friction factor function of the Reynolds number Re:

$$f = \frac{16}{Re} + 0.0025 = \frac{16\mu}{2r\rho v} + 0.0025 \tag{A4}$$

where μ is the magma viscosity, which is calculated according to Hess and Dingwell (1996). Viscosity increases as water is exsolved into the bubbles, and, when they are in equilibrium with the liquid, the solubility law gives the weight fraction x of water remaining in the liquid:

$$x = \kappa\sqrt{P} \tag{A5}$$

with Henry's constant $\kappa = 3.44\times10^{-6}$ kg$^{0.5}$ m$^{0.5}$ s^{-1} determined from the best-fit parameters of the second-order polynomial regression with intercept at zero (Equ. (A5)) of our experimental set in equilibrium (Table 1.1). The difference with the value determined by Mangan and Sisson (2000) for the same PCD rhyolite (4.15×10^{-6}) is mainly due to the form of the regression equation they used (non-zero intercept second order polynomial regression). The mixture density ρ is calculated using the perfect gas law:

$$\rho = \alpha\rho_g + (1-\alpha)\rho_l = \alpha\frac{M}{RT}P + (1-\alpha)\rho_l \tag{A6}$$

Where ρ_l is the liquid density, ρ_g is the gas density, α its volume fraction, M is the water molecular weight, T the mixture temperature, and R the universal gas constant. The gas volume fraction at equilibrium α_{up} (Fig. 4) is calculated from the difference between the maximum amount of water that can be dissolved in the magma at a given pressure P and the original water content at the initial pressure P_0:

$$\alpha_{up} = \frac{\beta}{MP + \beta} \quad\text{with}\quad \beta = RT\rho_l\kappa\left(\sqrt{P_0} - \sqrt{P}\right) \tag{A7}$$

From Equs. (A6) and (A7), we deduce that the mixture density ρ is only function of the pressure P. The variation of ρ with depth could therefore be written:

$$\frac{d\rho}{dz} = F(P)\frac{dp}{dz}$$

(A8)

One can recast Equs. (A2),(A3), and (A8) as:

$$\frac{dp}{dz} = \left[-\rho g - \frac{\rho v^2 f}{r}\right]\left[1 - v^2 F(P)\right]^{-1}$$

(A9)

The function $F(P)$ has to be determined for each experimentally determined regime: equilibrium, slow growth, and fast growth (Fig. 4). Equ. (A9) is then solved using a fourth-order Runge-Kutta algorithm with a constant distance step of 0.5 m below 50 vol.% porosity and 0.05 m above.

In the equilibrium regime, $F(P)$ can be readily determined from the derivation of Equ. (A6) with respect to z, replacing α by its expression α_{up} at equilibrium (Equ. (A7)):

$$F(P) = \left[\frac{\rho_l \kappa}{M}(\beta + \rho_l RT)\left(\frac{\sqrt{P_0}}{P^2} + \frac{1}{2P^{3/2}}\right) - \frac{\beta \rho_l \kappa}{2MP^{3/2}}\right]\bigg/\left(\frac{\beta}{MP} + 1\right)^2$$

(A10)

Experimental data (Fig. 1) show that the critical decompression rate between the equilibrium and the slow growth regimes varies between 0.125 MPa s^{-1} at high pressure and 0.175 MPa s^{-1} at low pressure. A unique median value of 0.15 MPa s^{-1} has been used to determine the boundary between the two regimes.

The slow growth regime is a linear function of α and P (Fig. 3; see Table 1.3 for empirical constant value):

$$\frac{d\alpha}{dz} = A_z \frac{dp}{dz}$$

(A11)

Hence, $F(P)$ is given by the derivation of Equ. (A6) with respect to z using Equ. (A11):

$$F(P) = \frac{M}{RT}(A_z P + \alpha) - A_z \rho_l$$

(A12)

In this regime, the melt viscosity is calculated from the water content at P_{right} (Equ. (A5), Fig. 4), because the amount of water in bubbles at a given pressure corresponds to the equivalent equilibrium value α_{right}. P_{right} is obtained using Equ. (A7):

$$MP_{right}\alpha_{right} + TR\kappa\rho_l\left(\alpha_{right} + 1\right)\left(\sqrt{P_{right}} - \sqrt{P_0}\right) = 0 \tag{A13}$$

The boundary between the slow growth and the fast growth regimes is reached when the difference between the disequilibrium (α) and the equilibrium (α_{up}) porosities $\Delta\alpha$ is greater than a critical value $\Delta\alpha_{cr}$ (Fig. 4). The relation between $\Delta\alpha_{cr}$ and the decompression rate is given by the nonlinear regression:

$$\ln(\Delta\alpha_{cr}) = a_1 \ln\left(\frac{dP}{dt}\right) + b_1 \tag{A14}$$

Experimental data were used for the regression when available and interpolated between the slow and fast growth curves when no data point fell on $\Delta\alpha_{cr}$ (Figs. 3 and A1). The nonlinear form of Equ. (A14) has been preferred over a linear form to ensure a realistic (asymptotic) behavior of the critical porosity at large decompression rates.

In the fast growth regime, $\Delta\alpha$ is given by the linear regression for each decompression rate (Fig. 3). We use the differential form:

$$\frac{d\Delta\alpha}{dz} = G(P)\frac{dP}{dz} - A_s\frac{dP}{dz} \tag{A15}$$

where A_s varies in function of the decompression rate according to:

$$A_s = a_2\frac{dP}{dt} + b_2 \tag{A16}$$

and $G(P)$ is the derivative of Equ. (A7) with respect to z:

$$\frac{d\alpha_{up}}{dz} = \left[\left(-\frac{MRT\rho_l\kappa\sqrt{P}}{2} - \beta M\right)\bigg/(MP+\beta)^2\right]\frac{dP}{dz} = G(P)\frac{dP}{dz}$$

Hence, the porosity is again a sole function of pressure, and the derivative of α with depth becomes:

$$\frac{d\alpha}{dz} = \frac{dP}{dz}[G(P) - \Delta\alpha]$$

(A17)

We can therefore derive Equ. (A6) with respect to z using Equs. (A15) and (A17) to get $F(P)$:

$$F(P) = (G(P) - A_s)\left(\frac{M}{RT}P - \rho_l\right) - \alpha\frac{M}{RT}$$

(A18)

Melt super-saturation and bubble spacing are the main controls of bubble growth rate in disequilibrium (see section *Regimes of Bubble Growth*). The differential form of Equ. (A15) allows a melt to reach atmospheric pressure super-saturated, assuming that the former process dominates. The alternate possibility is to force $\Delta\alpha$ to vanish at atmospheric pressure, which correspond to the control of the latter process. We use the former possibility because we expect super-saturation possible at large decompression rates.

Table 1.A1 Symbols and constants.

Q	magma mass flux ($m^3\ s^{-1}$)
V	magma velocity ($m\ s^{-1}$)
R	conduit radius (m)
ρ	magma bulk density ($kg\ m^{-3}$)
ρ_l	liquid density ($kg\ m^{-3}$)
ρ_g	gas density ($kg\ m^{-3}$)
Z	vertical position along the conduit (m)
P	magma pressure (Pa)
μ	magma dynamic viscosity (Pa s)
G	gravity acceleration (9.81 $m\ s^{-2}$)
Re	Reynolds number
F	friction factor function of Re
M	water molecular weight ($18\times10^{-3}\ kg\ mol^{-1}$)
T	magma temperature (°K)
R	universal gas constant ($8.3144\ J\ mole^{-1}\ °K^{-1}$)
κ	Henry's diffusivity constant ($3.44\times10^{-6}\ kg^{0.5}\ m^{0.5}\ s^{-1}$)
α	gas volume fraction
x	water weight fraction

References

Alidibirov M, Dingwell, DB (2000) Three fragmentation mechanisms for highly viscous magma under rapid decompression, J Volcanol Geotherm Res 100:413-421

Barclay J, Riley DS, Sparks RSJ (1995) Analytical models for bubbles growth during decompression of high viscosity magmas, Bull Volcanol 57:422-431

Blower JD (2001) Factors controlling permeability-porosity relationships in magma, Bull Volcanol 63:497-504

Blower JD, Keating JP, Mader HM, Phillips JC (2001) Inferring volcanic degassing processes from vesicle size distributions, Geophys Res Let 28:347-350

Dobran F (1992) Nonequilibrium flow in volcanic conduits and application to the eruptions of Mt. St. Helens on May, 18, 1980, and Vesuvius in AD 79, J Volcanol Geotherm Res 49:285-311

Eichelberger JC, Carrigan CR, Westrich HR, Price RH (1986) Non-explosive silicic volcanism, Nature 323:598-602

Gaonac'h H, Lovejoy S, Stix S, Scherzter D (1996) A scaling growth model for bubbles in basaltic lava flows, Earth Planet Sci Lett: 139:395-409

Gardner JE, Thomas RME, Jaupart C, Tait S (1996) Fragmentation of magma during Plinian volcanic eruptions, Bull Volcanol 58:144-162

Gardner JE, Hilton M, Carroll MR (1999) Experimental constraints on degassing of magmas: isothermal bubble growth during continuous decompression from high pressure, Earth Planet Sci Lett 168:201-218

Gardner JE, Hilton M, Carroll MR (2000) Bubble growth in highly viscous silicate melts during continuous decompression from high pressure, Geochim Cosmochim Acta 64:1473-1483

Hess K-U, Dingwell DB (1996) Viscosities of hydrous leucogranitic melts: A non-Arrhenian model, Am Mineralogist 81:1297-1300

Jaupart C, Allegre C (1991) Gas content, eruption rate and instabilities of eruption regime in silicic volcanoes, Earth Planet Sci Lett 102:413-429

Klug C, Cashman KV (1996) Permeability development in vesiculating magmas: implications for fragmentation, Bull Volcanol 58:87-100

Larsen JF, Gardner JE (2000) Bubble-bubble interactions in rhyolitic melts: applications to the evolution of bubble size distributions, Earth Planet Sci Lett 180:201-214

Lyakhovsky V, Hurwitz S, Navon O (1996) Bubble growth in rhyolitic melts: experimental and numerical investigation, Bull Volcanol 58:19-32

Mangan M, Sisson T (2000) Delayed, disequilibrium degassing in rhyolite magma: decompression experiments and implications for explosive volcanism, Earth Planet Sci Lett 183:441-455

Mastin LG, Ghiorso MS (2000) A numerical program for steady-state flow of magma-gas mixtures through vertical eruptive conduits, Open-File Report of the USGS, pp 1-53

Melnik OE (2000) Dynamics of two-phase conduit flow of high-viscosity gas-saturated magma: large variations of sustained explosive eruption intensity, Bull Volcanol 62:153-170

Navon O, Lyakhovsky V (1998) Vesiculation processes in silicic magmas, in: Gilbert JS, Sparks RSJ (eds), The physics of explosive volcanic eruptions, Geol Soc Spec Pub, London, 145:27-50

Papale P, Dobran F (1993) Modeling of the ascent of magma during the Plinian eruption of Vesuvius in AD79, J Volcanol Geotherm Res 55:101-132

Papale P (1999) Strain-induced magma fragmentation in explosive eruptions, Nature 397:425-428

Proussevitch AA, Sahagian DL (1998) Dynamics and energetics of bubble growth in magmas: Analytical formulation and numerical modeling, J Geophys Res 103:18223-18251

Proussevitch AA, Sahagian DL, Anderson AT (1993) Dynamics of diffusive bubble growth in magmas: Isothermal case, J Volcanol Geotherm Res 98:22283-22307

Sparks RSJ (1978) The dynamics of bubble formation and growth in magmas: a review and analysis, J Volcanol Geotherm Res 3:1-37

Sparks RSJ, Barclay J, Jaupart C, Mader HM, Phillips JC (1994) Physical aspects of magma degassing I. Experimental and theoretical constraints on vesiculation, in: Carroll MR, Holloway JR (eds) Volatiles in magmas, Rev Mineralogy 30:413-445

Stasiuk MV, Barclay J, Carroll MR, Jaupart C, Ratte JC, Sparks RSJ, Tait SR (1996) Degassing during magma ascent in the Mule Creek vent (USA), Bull Volcanol 58:117-130

Toramaru A (1989) Vesiculation process and bubble size distributions in ascending magmas with constant velocities, J Geophys Res 94:17523-17542

Toramaru A (1995) Numerical study of nucleation and growth of bubbles in viscous magmas, J Geophys Res 100:1913-1931

Westrich HR, Eichelberger JC (1994) Gas transport and bubble collapse in rhyolitic magma: an experimental approach, Bull Volcanol 56:447-458

Wilson L (1980) Relationships between pressure, volatile content and ejecta velocity in three types of volcanic explosion, J Volcanol Geotherm Res 8:297-313

Woods AW (1995) The dynamics of explosive volcanic eruptions, Rev Geophysics 33:495-530

Yoshida S, Koyaguchi T (1999) A new regime of volcanic eruption due to the relative motion between liquid and gas, J Volcanol Geotherm Res 89:303-315

Zhang Y (1999) A criterion for the fragmentation of bubbly magma based on brittle failure theory, Nature 402:648-650

CHAPTER 2: RECONCILING PYROCLASTIC FLOW AND SURGE: THE MULTIPHASE PHYSICS OF PYROCLASTIC DENSITY CURRENTS[*]

Abstract

Two end-member types of pyroclastic density current are commonly recognized: pyroclastic surges are dilute currents in which particles are carried in turbulent suspension and pyroclastic flows are highly concentrated flows. We provide scaling relations that unify these end-members and derive a segregation mechanism into basal concentrated flow and overriding dilute cloud based on the Stokes number (S_T), the Stability factor (Σ_T) and the Dense-Dilute condition (D_D).

We recognize five types of particle behaviors within a fluid eddy as a function of S_T and Σ_T: (1) particles sediment from the eddy, (2) particles are preferentially settled out during the downward motion of the eddy, but can be carried during its upward motion, (3) particles concentrate on the periphery of the eddy, (4) particles settling can be delayed or "fast-tracked" as a function of the eddy spatial distribution, and (5) particles remain homogeneously distributed within the eddy. We extend these concepts to a fully turbulent flow by using a prototype of kinetic energy distribution within a full eddy spectrum and demonstrate that the presence of different particle sizes leads to the density stratification of the current. This stratification may favor particle interactions in the basal part of the flow and D_D determines whether the flow is dense or dilute. Using only intrinsic characteristics of the current, our model explains the discontinuous features between pyroclastic flows and surges while conserving the concept of a continuous spectrum of density currents.

Introduction

Pyroclastic density currents are rapidly moving mixtures of hot volcanic particles and gas that flow across the ground under the influence of gravity. These multiphase flows consist of particles of various sizes and densities, and a strongly buoyant gas phase. The complex interplay between sedimentation and entrainment, the difficulty of direct observations, and the absence of a direct

---

record of the internal flow structure, makes the study of pyroclastic density currents challenging. The resulting geologic literature is extensive, complex, and sometimes contradictory.

The deposits of pyroclastic density currents vary from stratified to massive. Stratified facies commonly exhibit sedimentary bedforms and the deposit is often weakly controlled by topography, generally mantling the landscape. Massive facies are poorly sorted, often structureless, and pond into depressions. The recognition of these facies has motivated two end-member models of pyroclastic density currents (e.g., [1,2]). Stratified facies are proposed to be the products of a dilute suspension called *pyroclastic surge,* in which particles are carried in turbulent suspension and in a thin bed-load layer. The generally thicker massive facies are the result of highly concentrated *pyroclastic flows* [3].

Mechanical models for both end-members have been developed, based on different assumptions of the physics of the flow. Surge models are assumed to have negligible particle interactions, particle homogenization by turbulence, an exponential sedimentation law, and are often restricted to a single particle size (e.g., [4-6]). Whereas there is little debate that deposition in surge occurs by aggradation, in a layer-by-layer fashion, it is unclear whether pyroclastic flows freeze en masse or gradually sediment particles. Arguments for en masse deposition include the poorly sorted nature of deposits and the common presence of coarse-tail grading of lithics and/or pumices [7,8]. Sedimentation by freezing implies that the deposit is directly representative of the dynamical state of the moving flow, and this has motivated analogies between pyroclastic flow and hydraulic current or sliding bloc (e.g., [9,10]). Arguments for deposition by aggradation include the existence of compositionally distinct units within some massive deposits and the particle fabric of flow units [11-13]. Considering pyroclastic flows as rapid granular flow is consistent with aggradation [e.g., 14] and some granular models have recently been applied successfully [e.g., 15,16]. However, any unification of the end-members is difficult because the assumptions implicit in each model are incompatible.

Hence, whether pyroclastic flows and surges represent two truly distinct phenomena remains unresolved. The density discontinuities reproduced in experiments of fluidization [17] and high-speed two-phase flow decompression [18], as well as the marked facies diversity of the deposits, are cited in support of a discontinuity between flow and surge. However, deposits composed of a mixture of the two facies, such as the Mt. Pelée 1902 nuée ardente or the Mt. St Helens 1980

blast, motivated a reconsideration of the relationship between the two types [2]. Advocates for a continuous spectrum of density currents proposed that *surges* are density stratified [7,19-21]. They hypothesize that the concentrated base of such a stratified surge can sometimes generate dense underflows that produce the massive deposits characteristic of pyroclastic flows [11,22]. For example, Druitt [21] explains the whole spectrum of facies observed in the 1980 Mt. St Helens lateral blast deposit using the continuum approach. Recently, visual observations of flow separation at Montserrat [23,24] and Unzen [25] helped to connect processes and related deposits.

Recognizing the paradox inherent in the concept of a continuous spectrum between pyroclastic flows and surges and the basic assumptions commonly used in their modeling, we propose a unifying mechanical model that identifies flows and surges as two entities coexisting in pyroclastic density currents. Our approach accounts for the complexity in the dynamics of multiphase flow introduced by turbulence, and is based on scaling relations of the dominant mechanisms that occur in the currents. Our model focuses on the interplay between particles and turbulence in the absence of particle-particle interaction, and proposes a threshold criterion between dense and dilute conditions, from which the coexistence of surge and flow is derived. We adopt a Lagrangian-Eulerian approach in the dilute regime, however a complete development of a mechanical model of dense granular flow is beyond the scope of this paper.

The idea of linking flows and surges has already been proposed in the literature. While most authors present conceptual models based on geological evidence (e.g., [21,25-29]), few have addressed the fluid mechanics aspect of the problem (e.g., [20,30,31]). Mechanical models of surges assume that turbulence homogenizes the vertical distribution of pyroclasts [5,32,33]. The sedimentation of each class size of particle within the flow/surge is described by the ratio of the particle terminal fall velocity, U_T, and some Eulerian time scale of the flow. The time scale could be given by the horizontal speed of a given volume within the surge [20,33], or by the flow thickness if no velocity gradient within the flow is assumed [5,32]. Coarse particles are calculated to sediment faster than finer ones, and their increased concentration at the base of the surge generates dense underflows [20].

Our approach relaxes the ad hoc assumption that particles are homogenized and defines dimensionless numbers based on the Lagrangian characteristics of the flow, which allows a refinement of the understanding of particle gathering and dispersal by turbulence. The

homogenization of particle distribution is a consequence of the gas phase and the pyroclasts being in dynamic equilibrium when the particles are sufficiently "small". Noting that no quantitative estimate of critical particle size has been given, we question the assumption of homogenization when applied to the whole spectrum of pyroclastic density currents. We expect that the largest clasts can significantly affect the current dynamics and can decouple from the gas phase. By invoking a Lagrangian formulation, we quantify the critical size above which turbulence segregates particles and organizes them within the density current. Turbulence generates unsteady variations of the flow field while gravity sets a steady downward forcing on particles; they cannot be considered as two separate mechanisms that add linearly: their *simultaneous* consideration is necessary [34,35].

Neri and Macedonio [31] recognized the crucial effect of particle size on the dynamics of the flow using a three-phase model of collapsing volcanic columns. They point out that introducing two particle sizes (10 and 200 μm) changes dramatically the behavior of the flow. Motivated by the fact that pyroclastic deposit grain size distributions commonly encompass from −6 to 6 ϕ (6.4 cm to 156 μm), we feel there is a need to assess the role that the whole range of particles size has in the dynamics of the pyroclastic density currents. The proposed model is based on simple dimensionless numbers and is viewed as a first approach to these complex flows.

Segregation model: principles and assumptions

A pyroclastic density current is a fully turbulent parallel shear flow of gas with a significant load of particles with a wide range of sizes and densities. The flow is bounded by the ground at the bottom and by a free surface at the top, and the turbulence generates eddies of various sizes and speeds. In the fully turbulent regime, scalar quantities such as chemical components or temperature are well mixed, but separate phases in the flow such as particles are not necessarily well mixed, forming what has been recognized as 'mesoscale structures' [36]. To understand the interplay between these particles and the turbulence, consider only one given eddy within this spectrum. The acceleration of a sphere in a nonuniform flow is given by the Basset-Boussinesq-Oseen (BBO) equation derived by Maxey and Riley [37], which is the summation of the various forces acting on the particle (see *Appendix*). Following the truncation of the BBO equation by Raju and Meiburg [34], the Lagrangian formulation of a particle motion is, in dimensionless form:

$$\frac{dv}{dt} = \frac{u(t) - v(t)}{S_T} + \frac{e_g}{F_R^2} \tag{1}$$

Where $u(t)$ is the gas velocity, $v(t)$ the particle velocity, e_g the unit vector in gravity direction (see Table 2.1 for symbol definition). The Stokes number S_T and the particle Froude number F_R are given by:

$$S_T = \frac{t_v}{f} \frac{\Delta U}{\delta} = \frac{1}{f} \frac{\Delta \rho d^2}{18\mu} \frac{\Delta U}{\delta} \tag{2}$$

$$F_R = \frac{\Delta U}{\sqrt{g \delta}} \tag{3}$$

Where $\Delta\rho$ is the density difference between the particle and the gas ($\Delta\rho \approx \rho_p$, with ρ_p being the particle density), d is the particle diameter, μ is the gas dynamic viscosity, ΔU is the eddy rotation speed, δ its diameter, t_v is the response time of particles (Equ. (A2)), f is a drag factor function of the particle Reynolds number Re_p (Equ. (A3)), and g is the acceleration of gravity. Our approach is predicated on the statement that the interaction of particles with this eddy can be understood with two concepts: the Stokes number (S_T) and the Stability factor (Σ_T), which is a ratio of Stokes and Froude numbers.

S_T measures the coupling between gas and particles and is the ratio of the response time of particles t_v (particle reaction to unsteady forcing by gas turbulence), and a time scale of gas motion (eddy rotation time in turbulent flows). S_T controls a self-organization of the particles within an eddy, concentrating or dispersing particle as a function of their density and/or size; small enough particles follow the eddy motion whereas large enough particles are not be affected by the eddy [35]. If $S_T \ll 1$, particles couple with the gas. If $S_T \sim 1$, particles tend to travel at the eddy periphery, possibly escaping from its gyratory motion. Thus, particles with S_T near unity tend to gather at the eddy periphery [38]. If $S_T \gg 1$, particles decouple from turbulence, and particle motion is not governed by the gas phase.

Σ_T assesses the steady gravitational forcing on particles and is a measure of the particle residence within an eddy. We define Σ_T as the ratio of the terminal fall velocity U_T and the eddy rotation velocity ΔU.

$$\Sigma_T = \frac{\rho_p g\, d^2}{18\mu\, f\, \Delta U} = \frac{S_T}{F_R^2} = \frac{U_T}{\Delta U} \tag{4}$$

If $\Sigma_T \gg 1$, particles are influenced by gravity and tend to sediment from the eddy. If $\Sigma_T \ll 1$, particles are influenced by the eddy motion and tend to stay within it (R. Breidenthal, unpub. experimental results). The Stability factor predicts the migration towards the base of the eddy of large and/or dense particles.

Eddy mechanisms

The simultaneous consideration of S_T and Σ_T with the conditions listed in Table 2.1 leads to the recognition of five regions within a continuum of particle behaviors (Fig. 2.1). In the *Fall* zone ($\Sigma_T \gg 1$, $S_T > 1$), particles sediment from the eddy. We define that the lower boundary of the *Fall* zone is reached when ΔU is 30 % superior to U_T (log (Σ_T) = 0.5). In the *Unroll* zone ($\Sigma_T \sim 1$, $S_T > 1$), particles are preferentially settled out where the vertical component of ΔU is maximal downward but can be carried during the upward motion of the eddy. Particle transport becomes asymmetric; the eddy "unrolls" the range of particle sizes lying in this zone. We define that the lower boundary of this asymmetric transport is reached when U_T is 30 % inferior to ΔU (log (Σ_T) = -0.5). In the *Margins* zone ($\Sigma_T < 1$, $S_T \sim 1$), particles concentrate on the periphery of the eddy. Following Hogan and Cuzzi [38], we set the boundary at $S_T = 1$. In the *Turbulent Sedimentation* zone ($\Sigma_T \sim 1$, $S_T < 1$), particle sedimentation is modified by the turbulence structure. Particles settling can be delayed or "fast-tracked" as a function of the eddy spatial distribution [39]. In the *Homogenous Transport* zone ($\Sigma_T \ll 1$, $S_T \ll 1$), particles remain homogeneously carried within the eddy. Since particles in the *Homogenous Transport* zone are dynamically "attached" to the gas, we can assume that the flow satisfies the criteria for the application of mixture theory. The flow can be considered as a heavy gas, with a total density equal to the gas density plus the particle load of the *Homogenous Transport* zone. We define this condition as "particle homogenization". According to the boundaries defined above, the conditions $S_T = 1$ and $\Sigma_T < 1$

define the critical size above which the homogenization assumption no longer holds. Figure 2.1 shows the pattern of particle behavior defined by a 10-m wide eddy spinning up to 50 m/s. We choose this relatively small size to account for the reducing effect of the density stratification on eddy sizes (see *2.3 The density profile*). Using the limits between the domains in a quantitative fashion, these conditions would define a median critical size of 0.75 ϕ (0 ϕ at 20 m/s and 1.5 ϕ at 50 m/s). The change of eddy size of an order of magnitude will influence the median critical size by a factor 3.5 (Fig. 2.2).

The kinetic energy spectrum

The concepts developed for one eddy can be extended to a fully turbulent flow by using a prototype of the kinetic energy distribution within a full eddy spectrum. Eddies generated by turbulence are represented by a kinetic energy spectrum in Fourier space. The dimension of one eddy can be expressed as a wave number κ and its rotational speed as the kinetic energy per unit mass:

$$E(\kappa)\kappa = \frac{1}{2}\Delta U^2(\kappa) \tag{5}$$

$$\kappa = \frac{4\pi}{\delta} \tag{6}$$

Where $E(\kappa)$ corresponds to the kinetic energy spectrum in Fourier space integrated over a three-dimensional vortex of radius κ and $\Delta U(\kappa)$ is the characteristic speed of this vortex [40]. This spectrum describes how the energy is transferred from the injection frequency κ_i to (1) the smaller scale (higher wave numbers) at a rate $\varepsilon \sim \kappa^{-5/3}$ (Kolmogorov's law of decay) and (2) to the larger scale at a rate $\sim \kappa^4$ [40]. The largest possible scale is on the order of the flow height for incompressible flows, and the smallest scale we consider is on the order of the particle size. The total kinetic energy is related to $E(\kappa)$ by:

$$\frac{1}{2}U_{rms}^2 = \int E(\kappa)\,d\kappa \tag{7}$$

Where U_{rms} is the root-mean-square velocity of the gas. Given a prototype of $E(\kappa)$, the five domains of particle behavior defined above can be transposed from a ΔU-δ space to an E-κ space

for any specific particle size (Fig. 2.3). In a first approach, we use the prototype of energy spectrum for a free decaying three-dimensional isotropic turbulence described by Métais and Lesieur [41], noting that spectrum prototypes for shear flow have a similar form [42]:

$$E(\kappa) = A\kappa^8 e^{-4\left(\frac{\kappa}{\kappa_i}\right)^2} \tag{8}$$

Equation (7) gives $A \cong 44U_{rms}^2 / \kappa_i^9$ and the space transposition can be done with Equs. (5)-(8). The dynamic behavior of particles of a specific size within a flow can henceforth be characterized for a given kinetic energy spectrum (Fig. 2.3B).

In the *Eddy Mechanisms* section, we have characterized particle behavior in a single eddy. The extension to a full spectrum of eddies allows us to relate the size of eddies to their speed (Equ. (8) and Fig. 2.3B), and enables us to understand the behavior of all particle sizes in a full spectrum of turbulence (Fig. 2.4, with the same turbulent conditions as Fig. 2.3B). Integration of Equ. (8) shows that 90% of the kinetic energy is contained between $^3/_2$ κ_i and $^2/_3$ κ_i (bold part of the δ-axis in Fig. 2.4). The largest eddies contain therefore most of the kinetic energy and will dominate the particle transport.

When using the spectrum prototype (Equ.(8)), we assume negligible momentum exchange between gas and particles, and no particle-particle interactions. However, the spectrum of turbulence is likely to be modified by the particles. It has been shown that large particles with high Re_p create a wake that increases the amount of turbulence, whereas small particle dampen turbulence [e.g., 43], and Elghobashi [44] proposed that this turbulence modulation is a function of S_T. Since the modulation is generated over the length scale of the particle, ε will depart from the Kolmogorov decay. Unfortunately, no generalized prototype for inhomogeneous, particle-laden flow is yet available, but a coupled Lagrangian-Eulerian approach would allow modulating the spectrum in function of the particle load.

The density profile

Consider again a fully turbulent parallel shear flow of gas with a random load of pyroclasts. Given both *(1)* the self-organization process controlled by S_T (unsteady effect of the turbulence) and *(2)* the gravity-driven stratification of concentration predicted by Σ_T (steady forcing of the

gravity), the emergence of density stratification within the pyroclastic density current is expected. Whereas large particles with a *Fall* behavior are expected to concentrate at the base of the current rapidly, small particles with a *Homogenous Transport* behavior are homogenized within the current and produce a constant density profile. The general *average* density profile of the flow is a summation of each particle size characteristic profile determined by their dynamic behavior.

Density gradients within horizontally stratified flows hinder vertical energy transfer and limit the maximum internal waves frequency to the Brunt-Väisälä frequency N. In our case, the stratification is mainly caused by particles with large Σ_T. Among these particles, those with small S_T are the most effective in hindering the energy transfer. Hence, the density profile can be used to connect a concentration gradient within the flow to a maximum eddy size δ_i and speed ΔU_i (Fig. 2.5):

$$N = \frac{1}{2\pi}\sqrt{-\frac{g}{\rho_0}\frac{d\rho}{dz}} = \frac{\pi \Delta U_i}{\delta_i} \tag{9}$$

From the self-organization process (S_T) and the gravity-driven particle migration (Σ_T), the concentration of (coarse and/or dense) particles is higher at the base of the flow and the concentration gradient tends to be steepest at the base. Equation (9) predicts that eddies tend to be faster and smaller in strong concentration gradients (arrows in Fig. 2.5). Eddies formed at the base of such a turbulent dilute flow have therefore an enhanced carrying capacity compared to eddies higher above the base. The stratification process allows the flow to accommodate its loading and increases its transport capacity.

Equation (9) gives the largest possible scale of eddies in the kinetic energy spectrum for density-stratified flows. In consequence, we expect the spectrum of turbulence given by Equ. (8) for a non-stratified flow to be modified by the density gradient (Fig. 2.5). The amount of shear within a stratified flow modifies also the turbulence spectrum. Qualitatively, the increase of shear raises κ_i and diminishes the turbulent decay rate towards the higher wave numbers [45]. In other words, more energy is dissipated by the larger wave number and smaller eddies take more importance in the flow dynamics, modifying the spectrum shape (arrows in Fig. 2.3B).

Interaction with topography

Salient parameters to describe the encounter of a density-stratified flow with an obstacle are the flow Froude number F_{Rflow} of the fastest mode of the undisturbed flow (upstream) and the dimensionless obstacle height H_d [46]:

$$F_{Rflow} = \frac{U_{fl}}{4NH} \qquad \text{and} \qquad H_d = \frac{h_{obs}}{H} \qquad (10)$$

Where U_{fl} is the mean flow speed, H the upstream flow height, and h_{obs} the obstacle height. F_{Rflow} indicates the flow hydraulic regime, sub- or supercritical. The F_{Rflow}-H_d space defines three main flow behaviors: crossing, blocking, and hydraulic jump. In the first case, the flow strata maintain their integrity during the crossing. In the second case, blocking of the lower parts of the flow occurs. In the third case, a regime change occurs and a hydraulic jump separates the two regimes.

The Dense-Dilute condition

The frequency of particle interactions is a key factor in flow dynamics. The Dense-Dilute condition (D_D) is a measure of the importance of particle interactions within the flow [35]:

$$D_D = \frac{t_c f}{t_v} = \frac{3 \mu f}{\rho V_{rms} d} \qquad (11)$$

Where ρ is the flow bulk density, V_{rms} the root mean square of the particle speed, f is the Reynolds number based on this velocity (Equ. (A3)), and t_c the characteristic time between particle collision given by:

$$t_c = \frac{1}{n \pi V_{rms} d^2} \qquad (12)$$

Where n is the number density of particles. The right-hand side of Equ. (11) is obtained using that $n \, \pi \, d^3 \rho_p = \alpha \rho_p \approx \rho$, with α being the volume fraction of particles. If $D_D < 1$ (dense flow), particles do not have time to respond to the gas dynamic forces before the next collision, and the dynamics of the flow is dominated by particle-particle interactions. $D_D > 1$ (dilute flow) implies non-zero inter-particle distance.

Given the density stratification and the physical limit between a dense and a dilute flow as defined by D_D, a concentration threshold may be reached in the basal part, where granular motion will dominate. It is therefore likely that the current segregates into a basal concentrated, granular flow and an overriding dilute, turbulent, and density-stratified cloud (Fig. 2.6). Short-living collisional interactions dominate the resistance stresses for the rapid granular flow regime [15], and high particle concentration suppresses turbulence-generated segregation. We therefore expect the granular flow to be composed of particles with a small D_D, either because they are not sustained by turbulence (*Fall* region), or because they are likely to gather (*Unroll* and *Margin* regions). The gathering being controlled by the transient nature of turbulence, the latter case is expected to play a minor role in the average location of the boundary. Since particles from the *Homogenous Transport* produce a constant average vertical density profile, they will be trapped in the granular flow as well, producing a poorly sorted flow. Although based on a given particle size, D_D quantifies the boundary between dense and dilute parts of the flow, because the particle size that features the lowest D_D is likely to control this boundary. Further links between collisional interaction and D_D may validate the idea that the density gradient might be so important at the boundary that a discontinuity would be formed.

Discussion

General implications

Our model predicts the maximum particle size that a turbulent flow can carry. For example, a pumice of 3.2 cm needs 10-m wide eddies to be faster than 30 m/s to travel within a dilute surge (*Unroll* zone, Fig. 2.1) and cannot be transported homogenously by a turbulent flow of gas traveling at subsonic velocities (Fig. 2.2). Products of large ash-flows can be examined using these critical sizes to assess their possible mode of transport.

We expect the segregation process caused by the interplay of S_T and Σ_T to occur whether the density current is initially inflated, as it probably is the case during a column collapse, or deflated, like in a dome collapse. In the latter case, the current is entirely granular with $D_D \ll 1$ during its initiation and may inflate by incorporating air or exsolved gases. If the mixture of particle and gas becomes such that $D_D > 1$, segregation processes will take place, without the need of an upward flux of gas (e.g., [25]).

Particles in the *Unroll* zone (e.g., pumices between 0 and –4 ϕ in Fig. 2.4A and lithics between 1 and –3 ϕ in Fig. 2.4B) are likely to travel by intermittence, whenever an eddy of the appropriate size and spin occurs in the current. The kinetic energy spectrum will evolve in time as the density current travels across the landscape, modifying particle sizes affected by the *Unroll* zone. Given the asymmetric transport of this zone and that particle collection is favored at S_T near unity, the sedimentation/deposition of these particle is likely to occur in an intermittent fashion. If the current is dilute throughout its entire thickness (surge end-member), the *Unroll* zone is expected to control particles in saltation. Since particles with low S_T and Σ_T are not sedimented, the deposits of such turbulent flows will periodically exhibit a preferential settling of particles with S_T > 1 and Σ_T ~ 1. The layered deposit of surges may therefore represent the rapid variations of the turbulent conditions within the current.

Despite the observation that the "fines-depleted flow" defined by Walker [2] includes elutriation gas pipes, we note that the smallest median size is about 1 ϕ, whereas median sizes up to –10 ϕ have been measured [47]. Whatever processes generate fines-depleted deposits, this smallest value is consistent with the critical size for tephra homogenization by turbulent flow (Fig. 2.2). In other words, particles below the critical size can very easily be reentrained by a turbulent cloud and therefore are less likely to sediment.

Pyroclastic density currents have particles of different densities, ranging commonly from 1000 kg/m^3 (pumice) to 2500 kg/m^3 (lithic). The turbulent flow illustrated in Figure 2.4 is able to transport pumice up to ~ –4 ϕ and homogenize (turbulent mixing) pumice smaller than 0 ϕ (Fig. 2.4A, arrows I and II). Lithics smaller than –3 ϕ are carried whereas lithic smaller than 1 ϕ are homogenized (Fig. 2.4B, arrows I and II). We note that a simple "hydraulic equivalence" ($\rho_p \cdot d$) is a good first-order approximation. Widely used to characterize particle suspension in turbulent flow, the Rouse number is a concept close to Σ_T, although based on an average Eulerian velocity of the flow (horizontal in our case). If this velocity is on the order of U_{rms} at κ_i, it would predict that the boundary between transport and deposition is located at Σ_T ~ 1. Since this condition is satisfied in the middle of the *Unroll* zone (Fig. 2.4), the Rouse number based on such a velocity is also a satisfying first-order approximation of the *time-averaged* behavior of the flow. However, the S_T–Σ_T framework is necessary to understand *transient* phenomenon such as particle

clustering, which are likely to control particle sorting, sedimentation, and the dense-dilute threshold.

The density profile of a given particle size derived by Valentine [20] is a sole function of the vertical velocity gradient. The Lagrangian approach reveals that the density profile is a complex function of U_{rms}, the dusty gas bulk density (as defined by the concentration of particles lying in the *Homogenous* zone), the turbulent spectrum shape, and the velocity gradients. Beyond the average density profiles proposed previously (e.g., [20,21]), our approach highlights the potential for transient high concentration of particles (*Margin* zone, $S_T \sim 1$), as large eddies are generated and dissipated continuously.

We would like to emphasize that S_T and Σ_T are important scaling parameters for experimental work. In other words, particle sedimentation cannot be well represented if these dimensionless numbers are not properly scaled. Although the comparison between sedimentary structures occurring under water and surge bedforms is tempting, it should be considered that, under equivalent conditions, S_T could vary of two orders of magnitude depending on the nature of the carrier phase (hot air viscosity is $\sim 1.5 \cdot 10^{-5}$ Pa·s at 300 °C whereas water is about 10^{-3} Pa·s at 20 °C). Moreover, the density contrast with the particles is greatly reduced with water as a carrier phase. Equation (1) is no longer valid because terms of the BBO equation neglected in the Raju and Meiburg [34] truncation cease to be negligible, and the full equation (A1) has to be used (see *Appendix*).

Hydraulic jump and blocking

Salient parameters to describe the interaction of a density-stratified flow with a relief are F_{Rflow} and H_d (Equ. (10)). A hydraulic jump generated by an obstacle or a break in slope causes a dramatic increase in the current depth and reduces its velocity. In the case of surges ($D_D > 1$), the potential effect of a hydraulic jump on the current can be represented by a sudden decrease of the flow speed and an increase of flow depth. The increase of depth ($\sim \delta_i$) narrows the saltation size range (*Unroll* zone in Fig. 2.7), and the speed reduction ($\sim U_{rms}$) lowers the maximum size the flow can transport (limit *Fall-Unroll* in Fig. 2.7). In this example, both the maximum size of particles carried and the critical size for homogenization are approximately reduced by a factor 2 (arrows I and II in Fig. 2.7). This should be expressed by an enhanced sedimentation after the jump to readjust the particle load to the new flow conditions. Experiments involving the

interaction of a density current in a water tank with a ridge confirm this increase in sedimentation (e.g., [33,48]). We predict from Fig. 2.7 that the load drop occurring at the jump between the two hydraulic regimes generates a moderately well sorted deposit coarser than the local average. Field studies describe ignimbrite lag breccia as very coarse material with a typical median size -3 ϕ and coarser, generally lithic-rich, and often devoid of fines (e.g. [2]). Although the generation of lithic-breccia by hydraulic jumps has been evoked by several authors [22,49], they do not consider the complexity introduced by the density stratification of the flow (i.e., Equ. (10)).

Flow segregation between a dilute cloud and a granular basal part is usually not recorded in deposits because of sedimentation processes occurring at the base of the current. However, when a pyroclastic current hits a barrier or sudden relief change, the lower part of the current may be blocked, whereas the upper part rides the obstacle. The dividing streamline proposed by Valentine [20] as a blocking criterion is based on experiments only valid at low Froude number [50]. Following Baines [46], we extend the concept of blocking to high Froude number and propose that it is controlled by the density gradient-dependent F_{Rflow} and the ratio of flow to obstacle height H_d. Although blocking can occur at any level of the stratified flow, the strongest density gradient occurs at the dense-dilute boundary. The granular part of the flow is therefore the most likely to be blocked. On the high side of the obstacle, a "segregated deposit" may result, consisting of layers from specific levels within the stratified flow. Fig. 2.6 illustrates the blocking of the granular part of a density current that produces stratified deposits on the topographic high.

Conclusions

We propose a segregation mechanism of pyroclastic density currents into basal concentrated, granular flows and a overriding dilute, turbulent, and density-stratified cloud based on the Stokes number (S_T), the Stability factor (Σ_T) and the Dense-Dilute condition (D_D). Our model reveals the importance of the combined unsteady effects of turbulence and steady effects of gravity. This model is able to explain the discontinuous features between pyroclastic flows and surges while conserving the concept of a continuous spectrum. From limited assumptions, the two end-members of pyroclastic density current can be derived by using *only* intrinsic characteristics of the flow considered.

Acknowledgements

Table 2.1 Symbols and constants.

p	magma pressure (Pa)
v	flow velocity (m s^{-1})
Q	mass flux (kg s^{-1})
ρ	mixture bulk density (kg m^{-3})
ρ_l	liquid density (kg m^{-3})
ρ_g	gas density (kg m^{-3})
x	water weight fraction
r	conduit diameter (m)
α	gas volume fraction
M	water molecular weight fraction (18×10^{-3} kg mole^{-1})
R	universal gas constant (8.3144 J mole^{-1} °K^{-1})
T	temperature (°K)
z	vertical distance along the conduit (m)
μ	magma dynamic viscosity (Pa s)
g	gravity acceleration (9.81 m s^{-2})
Re	Reynolds number
f	drag factor function of Re
κ	Henry's constant (3.44×10^{-6} Pa^{-1})
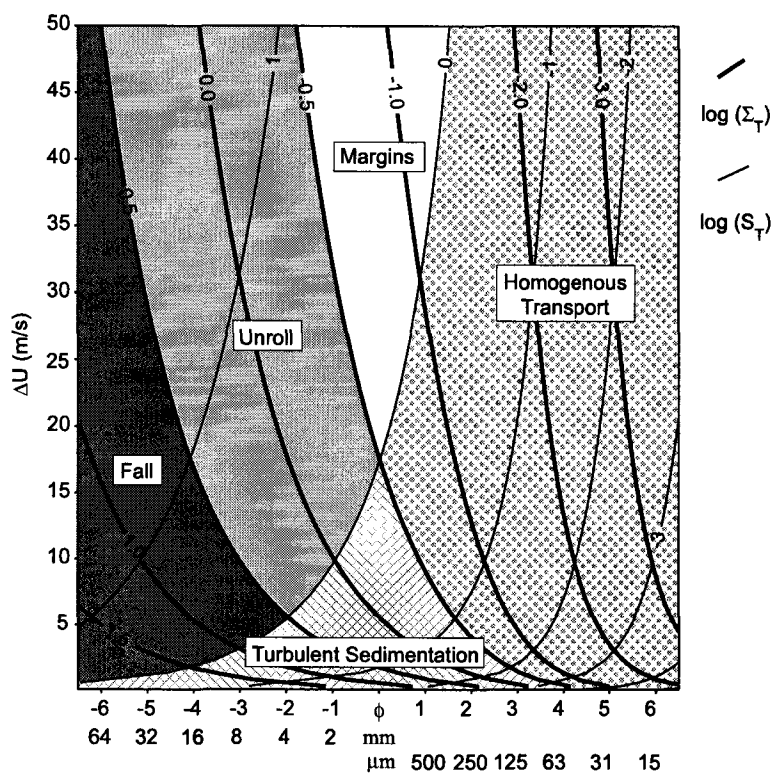
Figure 2.1 The interaction of 1000 kg/m^3 particles of various sizes (x-axis) with eddies of rotation speed ΔU (y-axis) and a diameter δ=10 m. Thin curves are Stokes numbers $\log(S_T)$ and thick curves are Stability factors $\log(\Sigma_T)$. See text for the significance of *Fall, Unroll, Margins, Homogenous Transport,* and *Turbulent Sedimentation* zones.
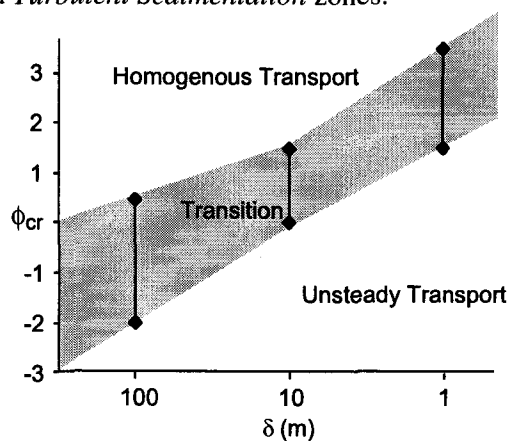
Figure 2.2 Evolution of the particle critical size with eddy size. The critical size is the upper limit of validity of particle homogenization by turbulence. The upper and lower values of the "transition" region are defined by S_T=1 and $\log(\Sigma_T)$=-0.5 within the interval 5 to 50 m/s of eddy spin velocity.
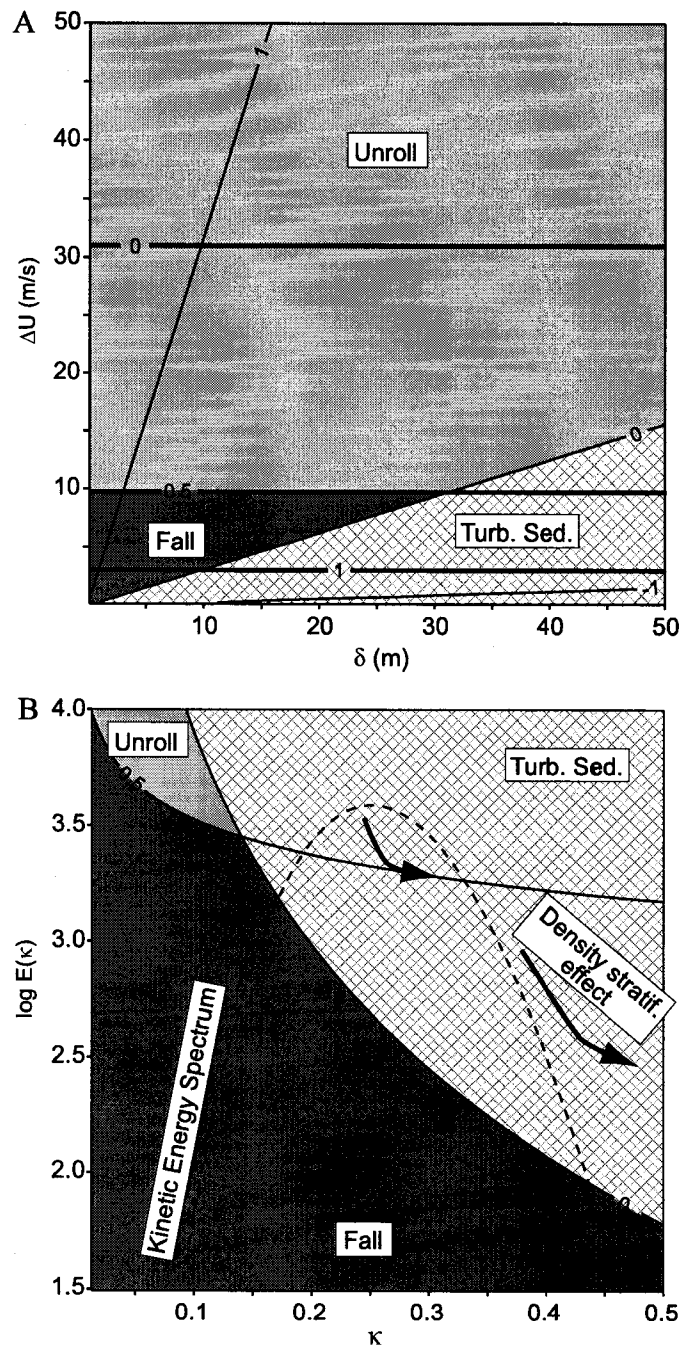
Figure 2.3 Dynamic behavior of -3 ϕ (8 mm) particles in two characteristic eddy spaces. Patterns code the particle behavior, thin curves are log(S_T) and thick curves are log(Σ_T). A. ΔU-δ space. B. E-κ space. The kinetic energy spectrum $E(\kappa)$ is calculated for κ_i= 0.25 m^{-1} and U_{rms} = 35 m/s. Arrows show the effect of density stratification on the shape of the spectrum.
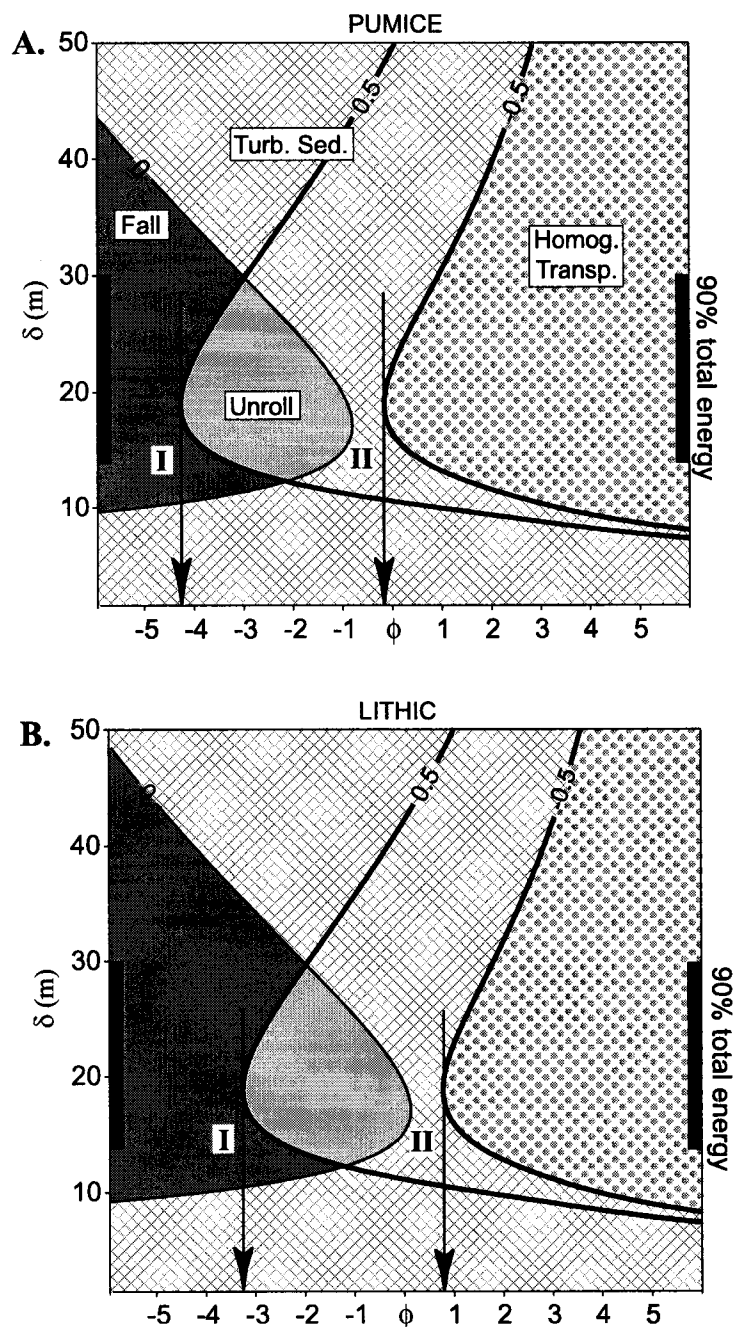
Figure 2.4 Particles behavior in the full spectrum of eddies shown in Fig. 2.3 in function of eddy size (y-axis) and particle size (x-axis). Bold parts of the y-axis correspond to 90% of the total kinetic energy. Patterns code the particle behavior, thin curves are $\log(S_T)$ and thick curves are $\log(\Sigma_T)$. Arrows I designate the maximum size transported and arrows II the maximum size homogenized (see text). A. Particles are pumices (1000 kg/m^3). B. Particles are lithics (2500 kg/m^3).
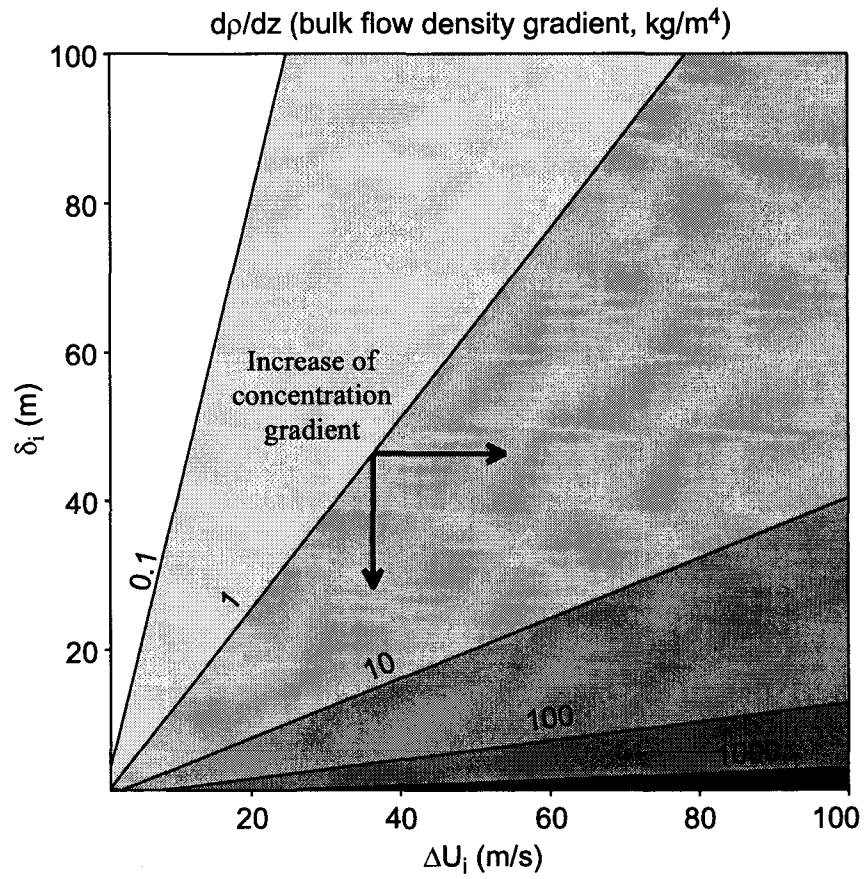
Figure 2.5 Maximum eddy size δ_i and speed ΔU_i for a given concentration gradient $d\rho/dz$ in a turbulent stratified flow. Arrows show that an increase of the concentration gradient shortens and/or accelerates the more energetic eddies.
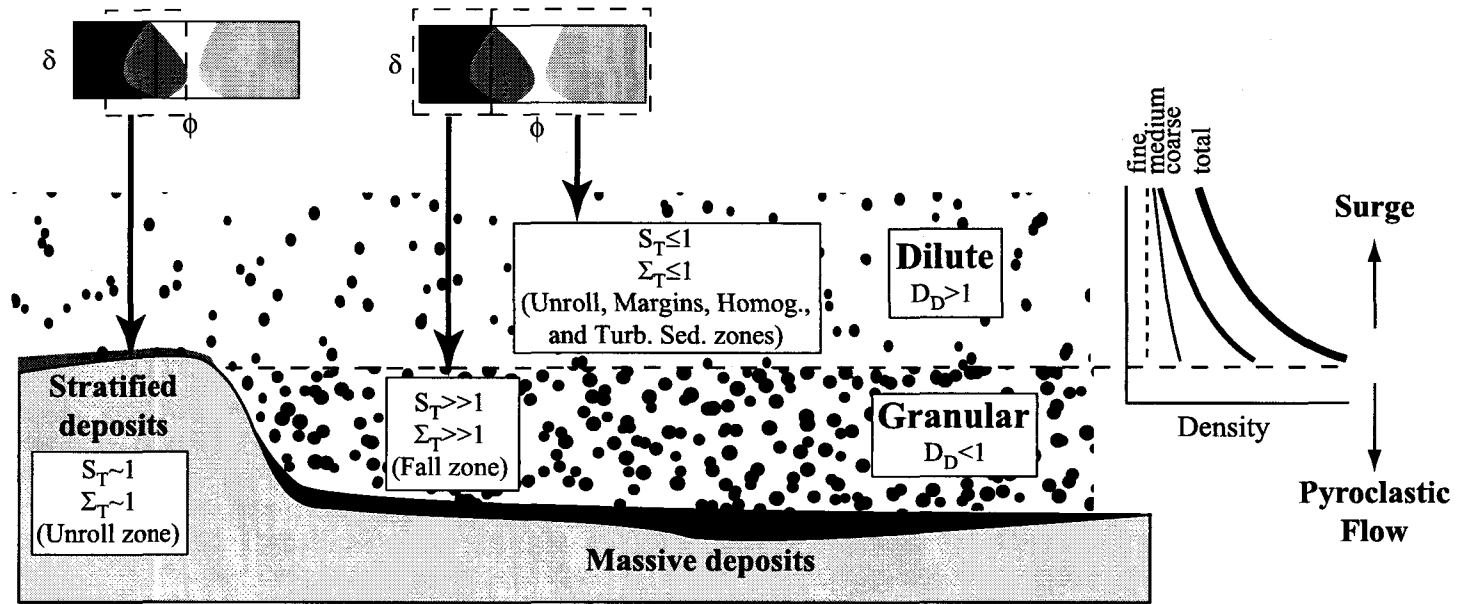
Figure 2.6: Schematic cross-section of a pyroclastic density current. The section is perpendicular to the flow direction with characteristic values of the three dimensionless numbers that govern the dynamics of the dilute part (S_T, Σ_T, and D_D). The end-member "surge" is obtained if the flow consists essentially of the dilute part, whereas the end-member "pyroclastic flow" has a very thin dilute portion. The right part shows a schematic density profile for three particle sizes in the dilute part. Note the total density is stratified due to the distribution of the coarse material, whereas the finest particles are homogenized throughout the flow thickness. The left part of the figure illustrates the overbanking of the dilute part. In this scenario, the dilute part overrides the obstacle, leaving stratified deposits on the topographic high.
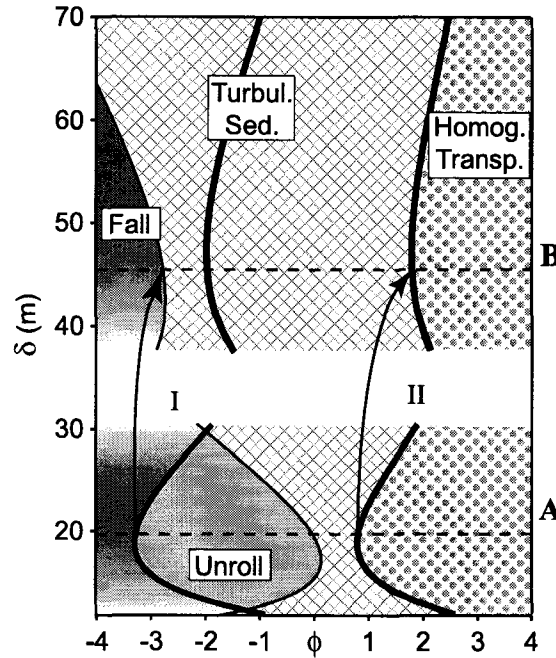
Figure 2.7 Effects of a hydraulic jump from super- to subcritical regimes on the transport capacity of a turbulent flow. Patterns code the particle behavior, thin curves are $\log(S_T)$, thick curves are $\log(\Sigma_T)$ and particle density is 2500 kg/m³. Flow conditions for stippled line A: U_{rms} = 15 m/s, δ_i = 20 m. Flow conditions for stippled line B: U_{rms} = 7.5 m/s, δ_i = 50 m.

Appendix 2

The Bassinet-Boussinesq-Oseen (BBO) equation expresses the acceleration of the spherical particle in a nonuniform flow as [35,37]:

$$\left(1+\frac{\rho_g}{2\rho_p}\right)\frac{dv}{dt}=\frac{f}{t_v}[u(t)-v(t)]+g\left(1-\frac{\rho_g}{\rho_p}\right)+\frac{3\rho_g}{2\rho_p}\dot{u}+\sqrt{\frac{9\rho_g}{2\pi\rho_p t_v}}\left[\int_0^t\frac{\dot{u}-\dot{v}}{\sqrt{t-t'}}dt'+\frac{(u-v)_0}{\sqrt{t}}\right] \quad (A1)$$

Where t_v is the particle velocity response time given by:

$$t_v=\frac{\Delta\rho d^2}{18\mu} \quad (A2)$$

and f is a drag factor valid over the entire subcritical range of particle Reynolds number ($Re_p \leq 10^5$) [51]:

$$f=1+0.15Re_p^{0.687}+\frac{0.0175}{1+42500Re_p^{-1.16}} \quad (A3)$$

With :

$$Re_p = \frac{U_T d}{\upsilon} \qquad (A4)$$

Where υ is the kinematic viscosity of the gas. Particles with a small Re_p (<10) have a drag caused by the gas viscous friction along the particle body, and $f \sim 1$. For high Re_p, the drag generated by vortices in the particle wake overcomes the viscous drag, and $f \gg 1$. The right-hand side of Equ. (A1) is the sum of the viscous, gravitational, buoyancy, virtual mass, and Basset forces acting respectively on the particle. In the case of pyroclastic density currents, the density ratio between particle and gas exceeds 10^3. It is therefore possible to truncate Equ. (A1) and use only the two first terms, namely the viscous drag and the gravity force [34]:

$$\frac{dv}{dt} = \frac{f}{t_v}[u(t) - v(t)] + g \qquad (A5)$$

Nondimensionalisation by the turbulence time scale (i.e. eddy rotation time) gives Equ. (1) [52].

References

[1]   R.A.F Cas and J.V. Wright, Volcanic successions: modern and ancient, Allen & Unwin, London, 1987.

[2]   G.P.L. Walker, Ignimbrite types and ignimbrites problems, J. Volcanol. Geotherm. Res. 17, 65-88, 1983.

[3]   R.S.J Sparks, Grain size variations in ignimbrite and implications for the transport of pyroclastic flows, Sedimentology 23, 147-188, 1976.

[4]   F. Dobran, A. Neri and G. Macedonio, Numerical simulation of collapsing volcanic columns, J. Geophys. Res. 98, 4231-4259, 1993.

[5]   M.I. Bursik and A.W. Woods, The dynamics and thermodynamics of large ash flows, Bull. Volcanol. 58, 175-193, 1996.

[6]   K.H. Wohletz and M.F. Sheridan, A model of pyroclastic surge, Geol. Soc. Amer. Spec. Paper, 177-194, 1979.

[7] R.S.J. Sparks, L. Wilson and G. Hulme, Theoretical modeling of the generation, movement, and emplacement of pyroclastic flows by column collapse, J. Geophys. Res. 83, 1727-1739, 1978.

[8] C.J.N. Wilson, The Taupo eruption, New Zealand II. The Taupo ignimbrite, Phil. Trans. R. Soc. Lond. A314, 229-310, 1985.

[9] J.E. Beget and A.J. Limke, Two-dimensional kinematic and rheological modeling of the 1912 pyroclastic flow, Katmai, Alaska, Bull. Volcanol. 50, 148-160, 1988.

[10] A.H. Levine and S.W. Kieffer, Hydraulics of the August 7, 1980, pyroclastic flow at Mount St. Helens, Washington, Geology 19, 1121-1124, 1991.

[11] M.J. Branney and P. Kokelaar, A reappraisal of ignimbrite emplacement: progressive aggradation and changes from particulate to non-particulate flow during emplacement of high-grade ignimbrite, Bull. Volcanol. 54, 504-520, 1992.

[12] M.J. Branney and P. Kokelaar, Giant bed from a sustained catastrophic density current flowing over topography: Acatlan ignimbrite, Mexico, Geology 25, 115-118, 1997.

[13] S.R. Hughes and T.H. Druitt, Particle fabric in a small, type-2 ignimbrite flow unit (Laacher See, Germany) and implications for emplacement dynamics, Bull. Volc. 60, 125-136, 1998.

[14] E.S. Calder, R.S.J. Sparks and M.C. Gardeweg, Erosion, transport and segregation of pumice and lithic clasts in pyroclastic flows inferred from ignimbrite at Lascar Volcano, Chile, J. Volcanol. Geotherm. Res. 104, 201-235, 2000.

[15] S. Straub, Self-organization in the rapid flow of granular material: evidence for a major flow mechanism, Geol. Rundsch. 85, 85-91, 1996.

[16] T. Takahashi and H. Tsujimoto, A mechanical model for Merapi-type pyroclastic flow, J. Volcanol. Geotherm. Res. 98, 91-115, 2000.

[17] C.J.N. Wilson, The role of fluidization in the emplacement of pyroclastic flows, 2: experimental results and their interpretation, J. Volcanol. Geotherm. Res. 20, 55-84, 1984.

[18] A.V. Anilkumar, R.S.J. Sparks and B. Sturtevant, Geological implications and applications of high-velocity two-phase flow experiments, J. Volcanol. Geotherm. Res. 56, 145-160, 1993.

[19] R.V. Fisher, Mechanism of deposition from pyroclastic flows, Am. J. Sci. 264, 350-363, 1965.

[20] G. Valentine, Statified flow in pyroclastic surges, Bull. Volcanol. 49, 616-630, 1987.

[21] T. Druitt, Emplacement of the 18 May 1980 lateral blast deposit ENE of Mount St. Helens, Washington, Bull. Volcanol. 54, 554-572, 1992.

[22] A. Freundt and H.-U. Schmincke, Lithic-enriched segregation bodies in pyroclastic flow deposits of Laacher See volcano (East Eiffel, Germany), J. Volcanol. Geotherm. Res. 25, 193-224, 1985.

[23] E.S. Calder, P.D. Cole, W.B. Dade, T.H. Druitt, R.P. Hoblitt, H.E. Huppert, L. Ritchie, R.S.J Sparks and S.R. Young, Mobility of pyroclastic flows and surges at the Soufriere Hills Volcano, Montserrat, Geophys. Res. Lett. 26, 537-540, 1999.

[24] R.S.J Sparks, J. Barclay, E.S. Calder, R.A. Herd, J.C. Komorowski, R. Luckett, G.E. Norton, L.J. Ritchie, B.Voight and A.W. Woods, Generation of a debris avalanche and violent pyroclastic density current on 26 December (Boxing Day) 1997 at Soufriere Hills volcano, Montserrat, in: T.H. Druitt and B.P. Kokelaar (eds) The eruption of the Soufriere Hills Volcano, Montserrat 1995 to 1999, Geol. Soc., London, Memoir. 21, 409-434, 2002.

[25] T. Fujii and S. Nakada, The 15 September 1991 pyroclastic flows at Unzen Volcano (Japan): a flow model for associated ash-cloud surges, J. Volcanol. Geotherm. Res. 89, 159-172, 1999.

[26] R.V. Fisher, Flow transformations in sediment gravity flows, Geology 11, 273-274, 1983.

[27] R.P. Denlinger, A model for generation of ash clouds by pyroclastic flows, with application to the 1980 eruptions at Mount St. Helens, Washington, J. Geophys. Res. 92, 10284-10298, 1987.

[28] E.M. Baer, R.V. Fisher, M. Fuller and G. Valentine, Turbulent transport and deposition of the Ito pyroclastic flow: determinations using anisotropy of magnetic susceptibility, J. Geophys. Res. 102, 22565-22586, 1997.

[29] T.H. Druitt, Pyroclastic density currents, in: Gilbert, J.S., and Sparks, R.S.J. (eds), The physics of explosive volcanic eruptions, Geol. Soc. Spec. Publ., London, v.145, 145-182, 1998.

[30] G.A. Valentine and K.H. Wohletz, Numerical models of plinian eruption columns and pyroclastic flows, J. Geophys. Res. 94, 1867-1887, 1989.

[31] A. Neri and G. Macedonio, Numerical simulation of collapsing volcanic columns with particles of two sizes, J. Geophys. Res. 101, 8153-8174, 1996.

[32] W.B. Dade and H.E. Huppert, Emplacement of the Taupo ignimbrite by a dilute turbulent flow, Nature 381, 509-512, 1996.

[33] A.W. Woods, M.I. Bursik and A.V. Kurbatov, The interaction of ash flows with ridges, Bull. Volcanol. 60, 38-51, 1998.

[34] N. Raju and E. Meiburg, The accumulation and dispersion of heavy particles in forced two-dimensional mixing layers. Part 2: The effect of gravity, Phys. Fluids 7, 1241-1264, 1995.

[35] C. Crowe, M. Sommerfeld and Y. Tsuji, Multiphase flows with droplets and particles, CRC Press, 1997.

[36] D.Z. Zhang and W.B. VanderHeyden, The effect of mesoscale structures on the macroscopic momentum equations for two-phase flows, Int. J. Multiphase Flow, in press.

[37] M.R. Maxey and J.J. Riley, Equation of motion for a small rigid sphere in a nonuniform flow, Phys. Fluids 26, 883-889, 1983.

[38] R.C. Hogan and J.N. Cuzzi, Stokes and Reynolds number dependence of preferential particle concentration in simulated three-dimensional turbulence, Physics Fluids 13, 2938-2945, 2001.

[39] P. Nielsen, Turbulence effects on the settling of suspended particles, J. Sediment. Petrol. 63, 835-838, 1993.

[40] M. Lesieur, Turbulence in fluids, Fluid Mechanics and its Applications, Kluwer Academic Publishers, 1997.

[41] O. Metais and M. Lesieur, Spectral large-eddy simulation of isotropic and stably stratified turbulence, J. Fluid Mech. 239, 157-194, 1992.

[42] A.M. Ahmed and S. Elghobashi, Direct simulation of particle dispersion in homogeneous turbulent shear flows, Phys. Fluids 13, 3346-3364, 2001.

[43] C.T. Crowe, On models for turbulence modulation in fluid-particle flows, Int. J. Multiphase Flow 26, 719-727, 2000.

[44] S. Elghobashi, On predicting particle-laden turbulent flows, Appl. Sci. Res. 52, 309-329, 1994.

[45] F.G. Jacobitz and S. Sarkar, On the shear number effect in stratified shear flow, Theoret. Comput. Fluid Dynamics 13, 171-188, 1999.

[46] P.G. Baines, Topographic effects in stratified flows, Cambridge University Press, 1995.

[47] M.J. Roobol, A.L. Smith and J.V. Wright, Lithic breccias in pyroclastic flow deposits on St. Kitts, West Indies, Bull. Volcanol. 49, 694-707, 1987.

[48] J. Alexander and S. Morris, Observations on experimental, nonchannelized, high-concentration turbidity currents and variations in deposits around obstacles, J. Sediment. Res. A64, 899-909, 1994.

[49] J.L. Macias, J.M. Espindola, M. Bursik and M.F. Sheridan, Development of lithic-breccias in the 1982 pyroclastic flow deposits of El Chichon volcano, Mexico, J. Volcanol. Geotherm. Res. 83, 173-196, 1998.

[50] W.H. Snyder, R.S. Thompson, R.E. Eskridge, R.E. Lawson, I.P. Castro, J.T. Lee, J.C.R. Hunt and Y. Ogawa, The structure of strongly stratified flow over hills: dividing-streamline concept, J. Fluid Mech. 152, 249-288, 1985.

[51] R. Clift and W.H. Gauvin, The motion of particles in turbulent gas streams, Proc. Chemeca '70, 14-28, 1970.

[52] J.E Martin and E. Meiburg, The accumulation and dispersion of heavy particles in forced two dimensional mixing layers. I. The fundamental and subharmonic cases, Phys. Fluids 6, 116-1132, 1994.

65

CHAPTER 3: PHYSICAL VOLCANOLOGY OF THE 2050 BP CALDERA-FORMING ERUPTION OF OKMOK VOLCANO, ALASKA*

Abstract

The 2050 ± 50 BP collapse of Okmok caldera generated pyroclasts that spread over 1000 km^2 on Umnak Island in the Aleutian Islands (USA). Geological and sedimentological data allowed us to reconstruct the eruptive dynamics of this volcanic eruption. After expelling up to 0.25 km^3 DRE of rhyodacitic Plinian air fall and 0.35 km^3 DRE of andesitic phreatomagmatic tephra, the caldera collapsed and produced the 29 km^3 DRE scoria Okmok II deposit, which is composed of valley-ponding, poorly sorted, massive facies and over bank, stratified facies with planar and cross bedding. Geological and sedimentological evidence suggests that the Okmok II deposits have been produced by a single density current that was segregated into a highly concentrated base and an overriding dilute cloud. The dense base produced the massive deposits, whereas the dilute cloud sedimented preferentially on hills as stratified deposits. The distribution of the deposits suggests that the pyroclastic current spread around Okmok in an axial symmetric fashion, encountering topographic barriers on the southwest and reaching the shoreline of Umnak on the other directions. Using the kinematic model proposed by Burgisser and Bergantz (2002), we show how the pyroclastic current decoupling was triggered by both sea entrance and topography interaction. Seawater absorbed the dense part of the current and the lithics transported by the dilute cloud. Topographical barriers noticeably decelerated both decoupled currents and favored sedimentation by partial or completed blocking. The resulting unloading of the subcritical, dilute current reduced drastically the runout distance by triggering an early buoyant lift-off.

Introduction

Okmok volcano forms the northwestern part on Unmak Island, which lies in the middle of the Aleutian volcanic chain (Alaska, USA). With a volume of 400-500 km^3, the Okmok shield is among the largest of the volcanic centers in the Aleutian arc. Okmok's predominantly basaltic

---

eruptive style was punctuated by catastrophic silicic-magma-bearing eruptions (Okmok I and II) that produced two nested, 10-km diameter calderas at the summit (Black 1975; Miller and Smith 1987). Intracaldera activity following the younger Okmok II caldera event formed numerous basaltic cones and lava flows. On-going deformation of the caldera floor has been recognized by SAR interferometry (Lu et al. 2000), and the most recent eruption was in 1997. Although numerous geologic (Byers, 1959) and geochemical observations (Byers, 1961) have been collected at Okmok, we note that most were aimed at the questions of arc petrogenesis (e.g., Kay and Kay 1994) and that the processes of specific volcanic events have to date not been explored systematically.

The focus of this study is on the latest caldera-forming eruption, Okmok II, with the goal of establishing the physical parameters related to this volcanic event. The eruption has been dated at 2050 ± 50 BP (Wolfe 2001) and covered some 1000 km^2 of the northeastern half of Umnak Island (Fig. 3.1). The products of this eruption consist of minor fall tephra overlain by voluminous, non-welded pyroclastic density current deposits. The bulk composition changes dramatically from rhyodacite in the first part of the fall deposits to basaltic andesite throughout the rest of the eruptive sequence (J. Larsen, unpub. data 2000).

In this study, we reconstruct the eruptive dynamics of the earliest phase of the eruption from geological and sedimentological data of the fall deposits, whereas data from the two facies of the pyroclastic density current deposits constrain the nature of the current. The interactions between the pyroclastic current and its surroundings (hills and sea) help us to elucidate some intrinsic characteristics of the current, such as internal particle concentration and thickness. Our conclusions on the fabric of the density current allow us to apply the Burgisser and Bergantz (2002) model (cf. Chapter 2) to illustrate its application and to validate it. This kinematic model enable us to infer the mean speed of the current at a given location and to determine whether the current was in sub- or supercritical regime using grain-size distributions and componentries from the deposits.

Methods

The topographic map was based on the 10-m resolution DEM of the USGS, and we used the geologic map of Byers (1959) for reference. Samples were localized by GPS (Table 3.A1 and Fig. 3.1). In the massive facies, the sample volume was 10×10×10 cm. Because the size of the

sampling area was limited, we also measured the 3 largest clasts over 2 m^2 around the sampling area to ensure than the sampling properly represented the coarsest sizes. For all samples, the average diameter of those clasts is at most 1 ϕ size larger than the maximum clast size from the samples. In the stratified facies, most samples were bulk samples over the entire thickness of the unit, whereas some samples were of individual layers (Table 3.A1). The coarsest sizes of the stratified facies are much smaller than the sampling volume and are thus properly represented.

Most samples were dry-sieved and counted in the field for the coarsest fraction (> -2 ϕ). The remainder of the samples was then wet-sieved in the laboratory to 4.5 ϕ in intervals of 0.5 ϕ. The finer fraction (<4.5 ϕ) was collected in 2-gallon water buckets and dried. The size distributions of the fine fraction were determined to 7 ϕ using a Spectrex IL1-1000 laser particle counter. Although the particle counter gives normalized wt.% between 4.5 and 10 ϕ, we normalized those values to sizes between 4.5 and 7 ϕ because the distilled water used to dilute the fine fraction contains impurities below 7 ϕ. We combined the particle counter and sieve data to obtain normalized grain size distribution (Table 3.A2). The error in the weight of each size fraction is estimated to be less than 0.1% for the field-sieved fraction and less than 0.05% for the finer sizes. Grain size parameters used in this study are the Iman median size M$_d$ (50 wt.%) and sorting σ (Cas and Wright 1987). Those parameters are accurate to ±0.1 ϕ. The componentry of the samples (Table 3.A3) was obtained by manually separating and weighing a statistically significant number of the different clast types for sizes coarser than 0 ϕ, and by counting 500 particles per class size with a binocular microscope for the smaller sizes down to 2 ϕ (4 ϕ for some samples). Conversion to weight fraction was done using the average weight of each particle type. Errors on the normalized proportions are on the order of 0.1%.

Stratigraphy of the Okmok II eruption

The deposits from the latest caldera-forming activity in Okmok show that there were two major eruptive phases. The first phase produced three tephra fall sequences (A, B, and C, Fig. 3.2), whereas the second generated a voluminous ignimbrite. Enough locations were found to reconstruct the distribution of the fall deposits, although the fall deposits are often buried underneath the pyroclastic current deposits. The initial fall sequence covers mostly the north of the volcano (Fig. 3.3), whereas the two other sequences occur east, extending over the nearby

Unalaska Island (Figs. 3.4 and 3.5). Because of this uneven distribution, two type sections were used to reconstruct the fall stratigraphy, and we used the method of Pyle (1989) to estimate the volumes of tephra. The first type section is located ~9 km north of the caldera rim near the shore (star symbol in Fig. 3.3), the second is located ~12 km east of the caldera rim (star symbol in Fig. 3.4). Each fall sequence has been divided in several units (A1-2, B1-2, and C1-3), the stratigraphic nomenclature of which is detailed in Fig. 3.2. This eruption produced both scoria and pumice with distinct compositions. Tan pumices, which compose the bulk part of the fall deposits, are rhyodacitic in bulk composition, whereas the black scoria, which compose the pyroclastic current deposits are basaltic andesite (J. Larsen, unpub. data 2000).

Fall deposits

The fall sequence A is the lowermost unit of the Okmok II event and consists of tan pumice lapilli with rare lithics. It commonly overlies a thick (>30 cm) soil with carbonized plant remains at the contact. We noted some carbonized weeds in their original living position within the unit A1. The fall sequence is up to 114 cm thick in the reference section (see Fig. 3.3) and can be subdivided into a reversely graded layer (A1) varying from fine ash (median grain size $M_d=0$ ϕ) to coarse lapilli ($M_d=-4.3$ ϕ), and an ungraded layer of lapilli A2 ($M_d=-1$ ϕ). Both units are well sorted ($\sigma=0.6$), and are separated by a fine ash deposit ($M_d=3.8$ ϕ) that is only present near the reference locality. The distribution map of the two layers A1 and A2 indicates a NNW dispersal axis (Fig. 3.3) with a cumulated volume of ~0.4 km^3. We indicate grain size of unit A1 at four localities, and density measurements reveal that the coarsest pumices of this unit average 500 kg m^{-3}.

The fall sequence B consists of brown pumice lapilli with fine internal layering. The sequence is up to 21 cm thick with $M_d=0.5$ ϕ in the reference section (see Fig. 3.4) and two groups of layers can be recognized based on the pumice morphology. The basal group of layers (unit B1) contains vesicular pumices with irregular shapes, similar to the ones from sequence A, whereas the upper group of layers (unit B2) consists of poorly vesicular pumices with blocky shapes. Up to 50% of these blocky pumices is vesicle-free glass. The distribution map of the two units indicates an easterly dispersal axis with a volume of ~0.05 km^3 (Fig. 3.4). We note a small amount of erosion or reworking between the sequences A and B, but there is little evidence for a significant time

break at this horizon, such as would be marked by soil development or abundant reworking by water.

Sequence C can be found on the northeast part of Umnak Island and on most of Unalaska Island, but we note its erosion from many exposed locations. The sequence is up to 20 cm thick in the reference section (see Fig. 3.4), where up to 10 layers can be recognized, with grain sizes that vary from fine ash ($M_d=3$ ϕ) to fine lapilli ($M_d=-0.5$ ϕ). Although unit C consists mainly of black scoria lapilli layers, one layer contains vitric and blocky pumice ash. All layers have rare lithics. The pumice-bearing layer delimits three groups of layers within the fall sequence C: 8 layers of scoria at the base (unit C1), the pumice layer (unit C2), and a scoria layer atop (unit C3). The distribution map of the three C units indicates an easterly dispersal axis and a volume of ~0.4 km^3 (Fig. 3.5).

Pyroclastic current deposits

The pyroclastic current deposits from the Okmok II eruption blanket the northeast part of Umnak Island, forming plateau surfaces around the volcano that are cut by modern stream channels (Fig. 3.6). These black, scoria-rich deposits generally overlie the fall sequences with a sharp contact, and occasionally present an erosive contact with underlying soil or older deposits. Most of the deposits are several tens of meters thick, massive, and poorly sorted, and comprise most of the deposit area coverage on Umnak Island. A common facies change occurs on hills and paleohighs (e.g., Idak plateau), where deposits are only up to a few decimeters, and have low angle cross-stratification or planar bedding, and improved sorting. A similar stratified facies is systematically found on Unalaska Island, where the deposit varies in thickness from one meter on its west shore to a few centimeters in the middle of the island, ~50 km from the caldera rim. Clasts composing the pyroclastic deposits can be divided in four types: juvenile scoria, lithics, crystals and glass. The black scoria is the most abundant type. Lithics comprise mostly aphyric basalt, minor basement clasts, and hydrothermally altered clasts. We separated a subset of lithics that are red, oxidized scoria frequently found in the pre-caldera stratigraphic sequence. Crystals are mostly plagioclase, with minor olivine and pyroxene. Most crystals were unbroken, and some crystals had adhering glass. Glass is mostly juvenile, but also include some aphyric basalt, from which the distinction is difficult.

The total volume of both pyroclastic facies on land is estimated at 24 km³, and the massive facies accounts for >99.9% of the total volume. Assuming a density DRE of 2500 kg m⁻³, and a deposit density of 1450 kg m⁻³ from the massive facies componentry, this volume translates into ~14 km³ DRE. The current volume of the caldera is between 40 and 60 km³. Preliminary surveys of the Okmok I deposits and the intra-caldera geology suggest that the volume of the preexisting caldera left by Okmok I is similar to the volume of infillings by post-caldera basalt and tephra. We thus assume that the overestimate of the volume of Okmok II caldera caused by the pre-existing Okmok I caldera compensate the underestimate caused by the post Okmok II infillings. The total volume of Okmok II eruption can therefore be estimated around 50 km³ (~29 km³ DRE), half of which was deposited on land.

Pyroclastic current deposits: massive facies

The thickness of the massive facies varies greatly, but the integration of visual estimates and tape measurements suggests that the thickness averages from ~ 60 m proximally to ~ 30 m at shore, at about 10 km from the caldera rim (Fig. 3.6 reports tape measurements). The top surface of the deposits forms a gently inclined plateau (Fig. 3.7), whereas the base is more irregular, revealing the jagged nature of the paleorelief. Thus, most thickness variations of the massive deposit result from the wavy paleotopography. Deposits are primary, with the exception of two regions that have been reworked (Fig. 3.6). The first region is located east of Okmok and features thick outcrops with rounded scoria, over-sized (>1 m) rounded lithic boulders, and numerous crude planar stratifications. These outcrops and several localities with thin (<1 m) volcano-sedimentary deposits suggest a subsequent reworking of the pyroclastic deposits with water on the eastern part of the island. The second region lies northwest of the caldera, where the pyroclastic deposit displays abundant red oxidized scoria with a few lithic pipes. These regions were avoided for the reconstruction of the eruptive dynamics. Although the massive facies is mostly structureless, occasional crude stratifications are observed where thickness variations are important. We note common accumulations of coarse scoria where the deposit thins to about one meter, and scarce occurrences of a thin (<10 cm) lithic-rich unit at the base on the lee side of paleohighs. On average, the massive facies have 69 wt.% of juvenile scoria, 26 wt.% of lithics, and 5 wt.% glass and crystals (Fig. 3.2), with median grain size ranging between -6 and 6 φ and

poor sorting (σ~3). Crystals are generally smaller than 1 φ and glass becomes more abundant below 0 φ, whereas scoria and lithics occur at all grain sizes.

To study local vertical variations of the massive facies, we determined the grain-size distribution and componentry of samples from the base and the top of various localities around the volcano (Fig. 3.1). Median grain sizes usually decrease by 1 φ size towards the top of the deposit with no change in sorting (Fig. 3.8). Bulk lithic contents vary of up to 20 wt.%, with no specific trend with stratigraphic position (Fig. 3.9). To examine if a particular size class is responsible for these bulk variations, we use the difference in normalized lithic proportion between two neighboring samples for a given grain size. For example, the bulk componentry of the sample AOK98 at the base of the deposit contains 17 wt.% more lithics than the sample AOK97 at the top (Fig. 3.9). The line labeled 'lithics' between these two samples indicates the arithmetic difference in lithics content between these samples for each grain size indicated on the x-axis. In other words, the data plotted at −2 φ equals the lithic content at −2 φ from the top sample 97 minus the lithic content at −2 φ from the bottom sample 98. The difference in lithic bulk content is thus caused by a higher lithic content of AOK98 between -5 and −1 φ. From the four localities represented on Fig. 3.9, we observe that the vertical variations of lithic content within the deposit are caused by the coarsest fraction of the clasts (above -2 φ). Variations of crystal and glass proportions are small, and generally affect all grain sizes.

To study radial variations of the massive facies, we analyzed grain sizes of 26 samples taken at various azimuths around the volcano from a similar distance of the caldera rim (8 to 12 km), of which we selected six representative samples for componentry determination. We selected those six samples at regular intervals of azimuth around the caldera to resolve the radial variation of componentry (locations symbolized by a triangle on Fig. 3.1). The sorting and the median size display weak variations around the volcano, and the distance from the rim controls the variations in median size rather than the azimuth (Fig. 3.10). As in the vertical sections, the small componentry changes are due to the coarse fraction (Fig. 3.11). The proportion of lithics varies between 9 and 38 wt.%, with the smaller values on the west of the volcano. We note that the lowest lithic content occurs at a locality (AOK164) that displays depletion in lithics regardless of grain size. Both this depletion and the improved sorting (σ=2.4) of this thin (2.5 m) locality reflect a frequent pattern occurring when the deposits thin because of important paleo-relief. We

indeed observe a general correlation of thinness and very crude stratification with locally better sorting in size and density within the stratigraphic column.

To study proximal-to-distal variations of the massive facies, we analyzed eleven samples from three longitudinal sections around the volcano (sections Ia-c on Fig. 3.1). In the northern section Ia, we note a decrease in median grain size of 2 ϕ units with distance from source, and no change in sorting (Fig. 3.12a). The lithic content increases by 20 wt.% with distance because of the coarse fraction, whereas the glass content rises slightly (Fig. 3.12b). In the northeastern section Ib, there is a modest decrease of median grain size of 1 ϕ unit (Fig. 3.12b). Whereas the proximal sample is moderately sorted ($\sigma=1.9$), the more distal samples display the characteristic poor sorting of the massive facies. Bulk lithic content decreases markedly (50 wt.%) with distance with variations concentrated mostly in the coarsest fraction (Fig. 3.12c). In the southern section Ic, median grain size decreases by 2 ϕ units, with no change in sorting (Fig. 3.12a). Bulk lithic contents vary by less than 25 wt.% with no systematic trend, with variations concentrated mostly in the coarsest fraction (Fig. 3.12c). In all sections, crystals and glass do not vary significantly in proportion.

In summary, the characteristics of the massive facies have similar trends regardless of azimuth despite its variable thickness. On a local scale, the base of the deposit is coarser and more variable than the top (Fig. 3.8), whereas in all sections there is a decrease in median grain size with distance from source without significant change in sorting. Lithic contents vary by about 20 wt.%, with most of the variation concentrated in the coarsest sizes (>-2 ϕ) of the distribution. Changes in componentry between the intermediate and the distal locations are irregular and remain below the vertical variations recorded at a given location.

Pyroclastic current deposits: stratified facies

The thickness of the stratified facies varies between 30 and 70 cm proximally and averages about 20 cm at ~20 km from the caldera rim (Fig. 3.6). The stratified facies is found only on tops of hills, such as Kettle Cape to the south, or elevated plateaus, such as Idak to the northeast (Fig. 3.1), and many locations display evidences of erosion. We note that these areas are exposed to the high winds common in the Aleutian Islands, and the loose nature of these relatively thin deposits account for their low preservation potential. Many thickness measurements are thus minimum

values because of erosion. It is nevertheless likely that the stratified facies thins with distance. We also note that the thickness of the stratified facies is more uniform than that of the massive facies.

The stratified facies can generally be divided in two units based on componentry. The basal unit is richer in lithics, with an average of 60 wt.% scoria, 35 wt.% lithics, and 5 wt.% glass and crystals, whereas the upper unit is richer in scoria with an average of 79 wt.% scoria, 15 wt.% lithics, and 6 wt.% glass and crystals (Fig. 3.2). Scoria and lithics occur at all grain sizes, whereas crystals are generally smaller than 1 ϕ and glass becomes more abundant below 0 ϕ.

The basal unit is generally massive and poorly sorted (σ=2) around the volcano, and varies little in grain size with distance (Fig. 3.13a). Grain size distribution show that the basal unit is generally coarser and better sorted than the upper one (Fig. 3.13b). Differences in componentry with size between the two units show that fractions coarser than –0.5 ϕ is the source of lithic enrichment (up to 30 wt.%) of the basal unit (Fig. 3.13c).

The upper unit presents alternatively planar stratification, absence of stratification, and low-angle cross bedding with gradational or sharp transitions between individual beds. No systematic variations, either vertically or horizontally, between these various patterns could be found, most likely because of the paucity of outcrops. The stratified nature of the deposits implies a large local variability of sorting and median size that depends on the exact size and position of the bulk sample. This variability can be illustrated by the change in median size of individual layers within the upper unit at Kettle Cape (Fig. 3.13b). The componentry between individual layers from the same locality does not vary significantly (Fig. 3.13d).

Relationship between massive and stratified facies

The correlation between the massive and stratified facies can be reconstructed from various locations around the volcano. The facies transition occurs systematically on the flanks of prominent ridges. The massive deposit usually thins uphill from tens of meters to meters with the occasional appearance of crude stratifications and laterally changes to stratified facies within meters. Stratigraphic correlations on the south side of Idak plateau (Fig. 3.14a) and at Hourglass Pass indicate that the massive and stratified facies are a lateral variation of the deposits, rather than a vertical succession (see the composite cross section on Fig. 3.14b). A lithic-rich unit is often present at the base of the stratified facies, but more rarely at the base of the massive facies,

where it is preserved only on the lee side of paleohighs (e.g., north of Kettle Cape). Accumulations of coarse scoria are found regularly around the volcano where the deposit thins to about one meter while remaining massive in texture. The size distribution and componentry of these accumulations display a sharp peak of coarse scoria, whereas the fine tail has a componentry similar to the main body of the massive facies (Fig. 3.15). Interestingly, a scoria accumulation near Hourglass Pass occurs at the facies transition between massive and stratified (AOK100, Fig. 3.1).

The southwestern ridges

Okmok peninsula is linked to the southwest part of Umnak Island by an isthmus with rugged topography, where altered Tertiary volcanic rocks form a succession of northwestward ridges (Byers 1959). To study the relationship between pyroclastic current deposits and topography across these ridges, we collected two transects within massive (IIa) and stratified (IIb) facies, respectively (Figs. 3.1 and 3.16a).

The massive facies is thicker than 20 m before and after the first ridge, and thins rapidly to a few meters after the second ridge. The median grain size decreases with distance at the same rate before and across the two ridges, with similar poor sorting (Fig. 3.16b). We note very little changes in componentry with distance: the lithic content oscillates by less than 10 wt.% because of the coarse fraction (Fig. 3.16c).

The stratified facies has a variable thickness of about a decimeter across the three first ridges, but thins to a few centimeters after the fourth ridge (Fig. 3.16a). The median grain size decreases slowly with distance across ridges 1-3, and diminishes rapidly after the fourth ridge, whereas the sorting remains good (σ~1.5) regardless of distance (Fig. 3.16c). The componentry does not change across the two first ridges, but we note an increase of 20 wt.% in lithics of all sizes across the third ridge and an major increase of 35 wt.% in glass clasts of all sizes (i.e. <0.5 ϕ) across the fourth ridge, at the most distal locality (Fig. 3.16d).

In summary, we note that the proximal rate of decrease in grain size is similar in both facies. Interestingly, the size distribution of the stratified facies at a given location matches the coarse half of the massive facies at the same location (Fig. 3.16b). This relationship seems true in general, because it is also verified on the north side of the Idak plateau and at Kettle Cape.

Unalaska Island

The pyroclastic deposits of the Okmok II eruption cover over half of the western part of Unalaska Island, which is separated from Umnak Island by a 8-km wide strait (Unmak Pass, Fig. 3.1). They occupy the same stratigraphic position as the ones on Umnak, directly overlying the fall deposits. These deposits vary from ~70 cm proximally to ~10 cm distally and they are generally structureless with discontinuous crude planar bedding. Unlike on Umnak Island, these stratified facies can be generally divided into a thin lithic-rich upper layer (78 wt.% scoria, 14 wt.% lithics, and 8 wt.% glass and crystals) and a lithic-poor basal layer (88 wt.% scoria, 5 wt.% lithics, and 7 wt.% glass and crystals). The distinction between the two layers is only apparent from the componentry data and cannot be ascertained in the field. Although the respective thickness of each layer is only constrained by the sampling size, we estimate the upper layer to form about a third of the total thickness. We note that some outcrops present slight post-depositional disturbances probably linked with the high void fraction of the basal layer that may favor downward migration of small, denser lithics from the upper layer. To compare trends between localities with similar path history (land or water), we separate for each layer the localities on the plateau (sections IIIa and c, Fig. 3.1) from the ones directly at shore (sections IIIb and d, Fig. 3.1).

The thickness of the basal layer decreases rapidly on the western coast (section IIIa) and thins gently across the plateau (Fig. 3.6). The grain size distribution is unimodal and the sorting improves slightly with distance (Table 3.1). The grain size decreases gently with distance both along the shore and across Unalaska's plateau, respectively (Fig. 3.17a). Interestingly, we note a sharp decrease of grain size between equidistant localities at shore (section IIIa) and on the highlands (section IIIb). The componentry of the basal layer remains remarkably constant over all locations (Fig. 3.17b).

The thickness of the upper layer is hard to survey because it has been partially removed by erosion. We note that the basal layer is always present below the upper layer except at one locality (AOK145), where only the upper layer crops out. The size distribution is bimodal (and) near the shoreline, which causes large sorting coefficients (Table 3.1), but this bimodality diminishes away from shore (Fig. 3.18). After remaining constant near the coast (section IIIc), the

median grain size decreases sharply inland (Fig. 3.19a). The componentry of the upper layer vary significantly across all grain sizes regardless of distance or location (Fig. 3.19b).

We observed that some localities near the shore, generally below 15 m in altitude, present an erosion of the stratified deposit, which is overlain by a decimeter of fine sand in turn capped by a meter of a similar layer of sand (Fig. 3.20). The two sandy units are separated by an erosive contact. The lower sand unit is well sorted ($\sigma = 0.85$) with a median size of 0.5 ϕ, whereas the upper unit is bimodal with the same mode as the lower layer plus a coarser mode of -1 ϕ. The componentry of both units is 80 wt.% lithics, 14 wt.% scoria, and 6 wt.% glass and crystals. Importantly, the sandy units contain clast types similar to the stratified deposits.

Discussion

Eruption dynamics

The thick soil underlying the fall deposits suggests that the 2050 BP Okmok II eruption occurred after a multiyear period of quiescence because soil formation is slow in Arctic region like the Aleutians Islands (J. Beget, pers. comm. 2000). Both the charred vegetation in its living position within the fall unit A1 and the preservation of the normal grading of this unit suggest that the ground was mostly free of snow at the time of the eruption. The eruption started as an increasingly vigorous Plinian column of rhyodacite, the umbrella of which was diverted to the NNW by strong winds. The distribution map shows that the vent was located in the northern part of the caldera. After a second steady pulse that produced unit A2, the column faded and the eruption stopped as indicated by the small amount of reworking between the sequences A and B. The interruption of the eruptive activity was long enough to gently rework the fresh deposit, but not sufficient to develop significant water drainage, suggesting an interval of days to months.

The second part of the eruption started from a vent located in the eastern part of the caldera with the wind blowing to the east, but the distribution map is not sufficient to indicate whether the various fall deposits originate from one or several source vents. Given the high proportion of glassy and blocky clasts, the internal discontinuous layering of the deposit, and the likely presence of abundant water within the caldera left by Okmok I, we suggest that unsteady phreatomagmatic explosions generated this event. As the explosive venting suddenly changed composition from dacitic to andesitic, fewer phreatomagmatic events occurred, but the wind

continued to blow eastward. Interestingly, the drastic compositional shift from rhyodacite to basaltic andesite occurred without noticeable changes in eruptive style or vent location. We note the presence of a short phreatomagmatic dacitic event within the sequence C (pumice-bearing unit C2). After expelling up to 0.5 km^3 of dacite (~0.25 km^3 DRE) and 0.35 km^3 of andesite (~0.17 km^3 DRE), the eruptive regime increased dramatically, three orders of magnitude in volume, and generated voluminous deposits that covered completely the northeast part of Umnak Island. Noting that the fall deposits were not hot enough to char vegetation when they deposited (Thomas and Sparks 1992), we conclude that the pyroclastic current deposits are responsible for the charred vegetation buried underneath the fall deposits. Those deposits, however, were not enough to cause welding, which suggests that their temperature was between 200 and 600 °C.

The climactic phase expelled about 50 km^3 (~29 km^3 DRE) of material, half of which was deposited on Umnak as a massive facies, and a fraction of which was deposited as a stratified facies on Unalaska and some hills of Umnak. The dramatic increase in both eruptive strength and lithic content lead us to temporally link the emplacement of these deposits and the initiation of the caldera collapse. Unfortunately, the style of caldera collapse cannot be inferred from the present sedimentological study. The characteristics of the massive facies have similar trends regardless of azimuth despite its variable thickness. On a local scale, the base of the deposit is coarser and more variable than the top (Fig. 3.8), whereas there is a decrease in median grain size in all directions with distance from source without significant change in sorting. The local componentry varies by about 20 wt.% in lithic content, with the variation concentrated in the coarse part (>-2 φ) of the distribution and a general trend of coarse-tail grading, with lithic-richer base and scoria-richer top. Changes in componentry between intermediate and distal locations are irregular and less than vertical variations recorded at a given location. The wavy nature of the bottom contact and the flat surface defined by its top (Fig. 3.7a) indicate that the massive facies filled in the previous topography, which was probably a rugged plateau with deeply incised gullies. The poor sorting, massive appearance, and distribution of the massive facies suggest that it formed by deposition from a dense, ground-hugging pyroclastic flow (Sparks 1976; Druitt 1998; Freundt et al. 2000). The valley-ponding deposition probably favored the larger variation of grain size at the base of the deposits. We interpret the crude stratification where the topography is rugged to result from the interfingering of multiple lobes within the pyroclastic flow. Along the same line, the weak coarse-tail grading is also probably caused by local conditions of sedimentation. Our grain

size analyses suggest that the spreading of the pyroclastic flow was axis-symmetric, which will be helpful to address the emplacement dynamics of the current, because it allows direct comparison of locations equidistant from the caldera rim.

Although one might think that such a large pyroclastic flow would significantly erode a rugged topography, evidence of erosion is scarce: the only erosive base was found at the proximal eastern locality AOK138 (Fig. 3.1). We interpret the high aphyric basalt content of the base of the location AOK124 (Fig. 3.9) as locally derived from this north-trending ridge, where outcrops of the same basalt abounds. This indirect evidence suggests than the current eroded part of the northward ridge directly north of the caldera (along section Ia, Fig. 3.1).

Less than 0.2% of the volume of the density current deposits is stratified. Nevertheless, the correct interpretation of the topology of this scarce facies is essential to understand the parent density current. The bedding pattern and the variable distribution of this facies suggest that it formed by deposition from dilute, turbulent pyroclastic surges (Fisher 1965; Valentine and Fisher 2000).

The localization of the stratified facies to paleohighs and the massive facies within depressions suggest that they can be characterized as over bank and paleovalley facies (Schumacher and Schmincke 1990). In this view, the scoria accumulations at the facies transition are likely remnants of pumice levees, and their presence where the massive facies thins out suggests that the paleorelief was not high enough at these locations to cause the deposition of the stratified facies. The fact that the stratified facies is a lateral variation of the massive facies suggests their simultaneous deposition. Both the synchronous and axis-symmetric nature of the deposits favor the interpretation of the Okmok II deposits to have been produced by a single density current. We believe the apparent contradiction of coexisting of pyroclastic flow and surge within a single current supported by our observations can be best explained by a segregated pyroclastic density current. In this hypothesis, the current consists of a highly concentrated base that produces massive deposits and an overriding dilute cloud that sediments stratified deposits preferentially on hills (Fisher 1965; Denlinger 1987; Valentine 1987; Fisher 1990; Druitt 1992; Baer et al. 1997; Burgisser and Bergantz 2002).

Interactions with topography

To the southwest of Hourglass Pass (Fig. 3.1), the pyroclastic density current traveled over successive ridges, leaving both stratified and massive facies in the small valleys that separate these ridges. We expect the fabric of these deposits give an insight into some of the processes at play between the dense and dilute parts within the current.

In particular, the massive facies reflect the local conditions of the dense portion of the density current. A pumice levee situated on a hill four kilometers before the first ridge (AOK100, Fig. 3.1) indicates that the transition between massive and stratified facies occurred at 70 m above the lowlands, which suggests that the thickness of the dense part was also about 70 m before the first ridge. Considering that similar transitions exist between massive and stratified outcrops, we infer that the dense part was less than 100 m above the valley bottom after the first ridge, and about 20 m after the second ridge. The first and second ridges are ~120 and ~130 m high, respectively. How can the dense part overcome ridges that are thicker than the current itself? Woods et al. (1998) proposed that ridges higher that a given gravity current can be overcome by the filling-up of the height difference by the upstream current. Such a process is predicted to significantly reduce the thickness of the deposit after the crossing, but would not affect the transport capacities of the current (Bursik and Woods 2001). On the other hand, if the basal part had enough momentum, it could overcome the ridge while maintaining a supercritical regime. The sudden loss of momentum would then enhance sedimentation at the ridge. A thickening of the deposits accompanied by a decrease in grain size would thus be expected just before or just after the ridge. We note a drastic thickness reduction of the massive deposit across the second ridge (from >19 m to 1.5 m), which is consistent with both partial blocking and excess momentum with thickening before the ridge. A similar measurement is unfortunately not possible across the first ridge because the base of the deposit is buried on both sides. There are no deviations in either grain size decay or componentry across both ridges when compared to an unobstructed pathway, which is not consistent with an excess momentum (section Ic, Fig. 3.12 and section IIa, Fig. 3.16b). The fabric of the massive deposit is thus likely to result from the partial blocking and filling-up of the dense part across the ridges (Woods et al. 1998).

The stratified facies does not noticeably vary in thickness, grain size, or componentry across the three first ridges, when compared to an unobstructed pathway (section IIIa, Fig. 3.17a and

section IIb, Fig. 3.16b). This invariance suggests that ridges 1-3 did not affect the dilute part of the density current, most likely because the current was much thicker than the ridges. The fourth ridge, however, caused significant decrease in thickness and grain size with enrichment in glass and crystal. A sudden thinning of the cloud because of partial blocking can cause this change. We do not expect partial blocking at the fourth ridge, however, because it has the same size as ridges 1-3. Most likely, this abrupt change suggests that the thick dilute current became buoyant at that point, preferentially entraining the light scoria while lifting off.

We can reconstruct a likely scenario to explain the depositional sequence (Fig. 3.21). The hypothesis of a single segregated current forming both facies is supported by the match of the size distribution of the stratified deposit with the coarser part of the nearby dense deposits (Fig. 3.16c), because this match is consistent with both the dense and dilute parts being in dynamic equilibrium and constantly exchanging particles with each other before decoupling at the first ridge (Fisher 1995). After being blocked at the first ridge, the basal part thickened until this ridge was crossed. The process repeated at the second ridge, but the upstream flux was not sufficient for the dense part to cross the third ridge. Meanwhile, the dilute part decoupled from the blocked part and successfully crossed the four ridges. After the fourth ridge, the upper cloud became dilute enough to buoyantly lift off.

Beyond water

The entrance of a pyroclastic current into the water has been documented extensively (e.g., Cas and Wright 1991) and possible scenarios abound (e.g., Legros and Druitt 2000). Yet, cases similar to Okmok, where currents traveled over water and deposited analyzable deposits on a distant shore are notably infrequent (Suzuki-Kamata 1988; Fisher et al. 1993; Carey et al. 1996; Allen and Cas 2001). We thus expect the analysis of the deposits beyond water to bring fresh insight into this type of event.

The most striking difference between the deposits on Umnak and Unalaska Islands is the complete absence of the massive facies on the latter island. From the data collected on Umnak, we deduce that the deposits sedimented from a density current that was segregated into a dense basal part and dilute cloud. The facies transition localized on the south side of Idak plateau (Fig. 3.14) suggests that the dense part was ~120 m thick when it reached the east coast of Umnak. Crossing of the 8-km wide Umnak Pass strait thus decoupled the two parts of the density current,

and the dense part dove into the waters. Geologic cases of a dense flow diving into the sea are multiple, such as the Roseau (Carey and Sigurdsson 1980) or the Grande Savanne (Sparks et al. 1980) ignimbrites. Unfortunately, at Okmok, the undisturbed nature of the massive facies at shore and the lack of underwater sampling limit the investigations on the interactions between hot pyroclasts and seawater (e.g., Sigurdsson and Carey 1989). We note that most of the mass of Okmok pyroclastic current did not cross Umnak Pass, unlike the Ito pyroclastic flow, which ran across a shallow lake of several tens of kilometers without leaving deposits at the bottom of the lake (Bear et al. 1997), or the Campanian ignimbrite, which traveled over water to produce thick deposits across the 35-km-wide Bay of Naples (Fisher et al. 1993).

Whether the crossing affected the dilute part can be assessed by comparing the stratified facies between the two islands. Beyond the variability in grain size distribution inherent to the stratified facies, we note that the sorting of the basal crudely stratified deposit on Unalaska matches that of individual layers found on Umnak (Fig. 3.22a). This similarity as well as stratigraphic correlations suggests that the basal unit on Unalaska is the lateral equivalent of the products of the dilute part on Umnak. The componentry of this unit, however, has the peculiarity of being devoid of lithics (Fig. 3.22b). This componentry remains similar over the whole island (Fig. 3.17b), which suggests that the sorting occurred at sea. The preferential loss of dense lithics during transport across water has also been reported for the Krakatau 1883 pyroclastic flow deposit (Carey et al., 1996), and the Kos Plateau Tuff (Allen and Cas 2001). Freund (2003) demonstrated this density-selective process with flume experiments simulating the entrance of pyroclastic currents into the sea. The key idea is that once lithics touch the surface of the water, they immediately sink; lithics are thus removed from the transport system of the dilute current, whereas the low density of the scoria ensures their preservation within the transport system. Following this reasoning, the high lithic content of the upper layer becomes problematic. How to preserve lithics across the 8 km strait? The answer may be linked to pumice rafts, which are large accumulations of low-density clasts on the sea surface generated by fallout or pyroclastic currents traveling over water (Whitham and Sparks 1986). Because densities and porosities of pumice and scoria have similar ranges, we expect that both pumice and scoria rafts share similar floatation properties (Gardner et al. 1996). If the scoria rafts produced by Okmok's eruption became continuous and thick enough, we hypothesize that they could act as a skin over the water, bouncing dense clasts as the ground would. In other words, this artificial enhancement of the

water surface tension could preserve lithics within the traveling current, thus allowing a lithic-bearing layer of pyroclasts to sediment over Unalaska. We note that the lithic-rich layer irregularly found at the base of both facies on Umnak is absent on Unalaska Island, as it cannot be correlated to the upper layer on Unalaska. Its absence after crossing the water is consistent with observed decreases in lithic size in similar lithic-rich ground layers of the Taupo ignimbrite (Wilson 1985) and the Ata pyroclastic deposits (Suzuki-Kamata 1988), which have also been attributed to selective loss of dense clasts after the currents crossed water. Interestingly, both layers are enriched in large (~1 ϕ) crystals in the coastal sections (e.g., Fig. 3.22b). Unfortunately, no satisfactory explanation for this local enrichment (or depletion in fine scoria) has been found.

We link the fine sand units eroding the coastal localities with the entrance of the density current into Umnak Pass. The peculiar location of this deposit, higher than the maximum storm wave base but below 15 m, and its stratigraphic characteristics suggest the sandy units were produced by a tsunami produced by the density current. In this view, the partially eroded basal layer represents the flooding event and the thick bimodal layer the backwash of the tsunami. The partial preservation of the lower stratified pyroclastic unit indicates that the tsunami wave(s) were slower than the dilute current.

The deposit stratigraphy and distribution over Unalaska Island allow us to further explore the probable sequence of deposition. First, we note that the highest locality (AOK145, Fig. 3.1) consists of only the upper unit, which indicates that the current responsible for the basal unit was less than 300 m thick, and that a thicker current deposited the upper unit. The sharp decrease in grain size between the low sites on the coast of Unalaska (section IIIa) and the high plateau (section IIIb) lead us to consider that the 100-m sea cliff acted as a significant topographic barrier of the dilute current, which is consistent with our thickness estimate of the current responsible for the basal unit. We noted earlier the curious bimodality displayed by the near-shore upper unit localities (Fig. 3.18). We see two possible explanations for this localized fines increase. First, the fines could result from short-lived aggregates formed either by electrostatic forces or by excessive moisture (e.g., chapter 16 in Sparks et al. 1997). Second, they could result from local steam explosions at the sea interface (e.g., Freundt 2003).

These observations illustrate clearly the contrasting behavior of dense and dilute flows when they encounter the density filter made by seawater. Similar behavior has also been reported in

literature. In the 1883 Krakatau eruption, one of the best studied examples, dense parts of the flow left massive deposits on the subhorizontal seafloor surrounding the caldera, while hot dilute parts of the flow traveled tens of kilometers over the sea (Carey et al. 1996; Mandeville et al. 1996). During the 1902 eruptions of Mt Pelée, pyroclastic currents entered the sea and their dense part broke telegraph cables nearly 20 km offshore, while associated dilute clouds ran out into the harbor and set fire to anchored ships (Lacroix 1904). In the on-going eruption of Montserrat, basal flows were witnessed to enter the sea and generate a zone of intense boiling, while the overriding ash cloud passed over the surface (Cole et al. 1998).

Implications on the fabric of density currents

The collapse of Okmok caldera generated about 50 km^3 of pyroclasts that spread over 1000 km^2 on Umnak Island before encountering topographic barriers on the southwest and sea elsewhere. The dynamics of emplacement of this deposit, however, remains inaccessible without a kinematic template for the internal workings of the current. We thus propose to apply such a template to retrieve dynamic variables from the information we gathered.

From the analysis of the two facies found around the volcano, we concluded that the pyroclastic deposits from Okmok sedimented from a single, density-segregated current composed of a basal dense part and a dilute cloud. The driving mechanism of segregation is the density stratification of the dilute part, which can concentrate particles to generate dense underflows (Fisher, 1965; Sparks et al. 1978; Freundt and Schmincke 1985; Valentine 1987; Druitt 1992). Both numerical simulations (Valentine and Wohletz 1989; Neri and Macedonio 1996; Todesco et al. 2002) and laboratory experiments (Choux and Druitt 2002) support this mechanism. In particular, we proposed simple Lagrangian scaling relations that consider the effects of turbulence on particle sorting, sedimentation, and transport in pyroclastic density currents (Chapter 2 and Burgisser and Bergantz 2002). From the resulting particle behaviors, Burgisser and Bergantz (2002) proposed the segregation of the density current into a dense basal part and overriding dilute cloud. They thus provide a suitable kinematic template that we briefly review below before applying to Okmok.

Theory and method

Following the model of Burgisser and Bergantz (2002), the multiphase interactions of particles within a pyroclastic density current can be characterized with two dimensionless numbers: the Stokes (S_T) and stability (Σ_T) numbers. S_T measures the coupling between gas and particles and is the ratio of the response time of particles t_v (particle reaction to unsteady forcing by gas turbulence), and the eddy rotation time:

$$S_T = \frac{t_v \Delta U}{\delta} \tag{1}$$

where ΔU is the eddy rotation speed and δ the eddy diameter. The response time t_v is given by:

$$t_v = \frac{\rho_p d^2}{18 \mu f} \tag{2}$$

where ρ_p is the particle density, d its diameter, μ is the carrier phase dynamic viscosity, and f is a drag factor given by (Clift and Gauvin 1970):

$$f = 1 + 0.15 Re_p^{0.687} + \frac{0.0175}{1 + 42500 Re_p^{-1.16}} \tag{3}$$

where Re_p is the particle Reynolds number given by:

$$Re_p = \frac{U_T d}{\upsilon} \tag{4}$$

where U_T is the particle terminal fall velocity and υ is the kinematic viscosity of the carrier phase. Σ_T assesses the steady gravitational forcing on particles and is a measure of the particle residence within an eddy:

$$\Sigma_T = \frac{U_T}{\Delta U} \tag{5}$$

In a fully turbulent current, the most energetic eddies govern the particle behavior. These eddies have a speed ΔU_i related to the root-mean square of the gas velocity U_{rms} by:

$$\Delta U_i = \sqrt{88} \, U_{rms} \, e^{-2} \tag{6}$$

The maximum size of these eddies (δ_i) is limited by the concentration gradient at the base of the current:

$$\delta_i = \frac{\pi \Delta U_i}{N} \tag{7}$$

Where N is the buoyancy frequency of the current near the ground. Using Equ. (7), it is thus possible to make S_T dependent on the buoyancy frequency, whereas Equ. (6) ensures that both S_T and Σ_T are constrained by U_{rms}, the root-mean square velocity of the gas. U_{rms} can be used as a proxy for the mean current speed U, to which it is related by (Pope 2000):

$$U \cong 4U_{rms} \tag{8}$$

The combination of S_T and Σ_T allows us to recognize three main particle behavior: sedimentation ($S_T > 1$, $\Sigma_T > 10^{-0.5}$), where particles are not sustained by turbulence and fall out; transport ($S_T < 1$, $\Sigma_T < 10^{0.5}$), where particles are well mixed within the flow; and transient ($S_T > 1$, $\Sigma_T < 10^{-0.5}$ and $S_T < 1$, $\Sigma_T > 10^{0.5}$), where particles gather and disperse in a transient way, leading to the creation of ephemeral mesoscale structures (Zhang and VanderHeyden 2002). The coexistence of particles with different sizes and densities leads the current to stratify itself in density, and, if a critical density of particles is reached, the current segregates in a dense basal part and an overriding dilute, density-stratified cloud (Burgisser and Bergantz 2002).

To relate field data with this model, we use the fact that at a given location, the dilute part of the current is most likely to sediment the particles that form the mesoscale structures. We track the domain of these structures by looking at Σ_T near unity ($10^{-0.5} < \Sigma_T < 10^{0.5}$) and S_T at unity. The particle density is calculated to the nearest hundredth of unity from the bulk componentry using 1000, 2500, 2000 and 2200 kg m^{-3} for the densities of scoria, lithic, glass and crystal, respectively. Remembering that Σ_T and S_T vary with particle size, we match the median grain size at $\Sigma_T = 1$ and require that the condition $S_T = 1$ lies within 90% of the size distribution. We thus obtain for each location a value of U_{rms} from Σ_T and a range of δ_i from S_T. The uncertainty linked with the determination of S_T give a range of buoyancy frequencies that can be combined with the estimate of the current height H and speed U to frame the Froude number F_R of the current (Burgisser and Bergantz 2002):

$$F_R = \frac{U}{4NH}$$

We demonstrate here how to retrieve the dynamic parameters of the current that traveled across Unalaska plateau (section IIIa in Fig. 3.1). Using the mean density (1150 kg m^{-3}) of the particles obtained from bulk componentry data (Fig. 3.17c) and Equs. (1)-(7), we can plot those ranges on a U_{rms} vs. grain size plot (Fig. 3.23). On this plot are represented three curves representing the key values of Σ_T (10$^{-0.5}$, 1, and 10$^{0.5}$) and six curves for S_T=1 corresponding to various values of the maximum eddy size δ_i. We then match the median grain size (50 wt.%) of each location at Σ_T=1 and represent the size distribution with a box that indicates the 5, 16, 50, 84, and 95 wt.% of the distribution. This match gives a value of U_{rms} for each sample, for which the mean current speed can be retrieved (Table 3.2, see also section IIIa on Fig. 3.24). The 5 and 95 wt.% marks give the range of δ_i, from which Froude numbers are calculated (Equ. (9), Table 3.2).

Proximal dynamics

There are two conflicting interpretations of the dynamical significance of individual layers within a stratified deposit. In the first view, pulsations of the entire current, and thus fluctuations of its mean speed, cause sedimentological variations between beds. In the second, transient motions within the current, and thus fluctuations in U_{rms} cause such variations. Unfortunately, the paucity of data limits the interpretation of the inter-layer variations in Okmok because only the deposits of Kettle Cape present abundant crossed and planar bedding. Our results simply show that the basal lithic-rich unit was deposited by a more energetic current/pulse than the upper scoria-rich unit (Table 3.2). We note that a similar unit has been described at Unzen, where it is thought to originate from the interface between the dense and dilute parts of the current (Fujii and Nakada 1999).

Backward modeling of the stratified deposits on Idak plateau indicates that the speed sharply decays from the northern edge inwards (curve 'Idak plateau' on Fig. 3.24). No significant obstacle, however, could explain such a deceleration. Considering the shape of the plateau and the high variability in thickness and grain size of the related stratified deposits, we suggest that the plateau acted as a stem, splitting the density current in two. The peak at the southwest tip thus acted as a shelter to the rest of the plateau and its altitude gives an upper boundary for the total current height. The deposit on the plateau thus recorded the lateral motions of the current, which

were small (6 to 24 m s^{-1}, Table 3.2) compared to its radial speed (60 m s^{-1} recorded at the plateau edge, AOK64 in Table 3.2). Taking in account the dense part thickness estimate, we therefore propose that the density current was about 300 m thick near Idak plateau with the essential of its mass concentrated in the bottom third, and was traveling at about 60 m s^{-1}.

The average speed of the pyroclastic density current and the volume of inland deposits can provide an upper estimate of the magma discharge rate. Assuming that the fastest speed estimates near the shore (~60 m s^{-1}; Table 3.2) are representative of the current average velocity, the 24 km^3 of inland deposits took at least 250 s to sediment if deposition occurred en masse. Using 1450 kg m^3 for the average density of the massive deposit gives a maximum discharge rate $<1.4\times10^{11}$ kg s^{-1} for the climactic phase of the Okmok II eruption. Of course, the real value is expected to be much lower because sedimentation is unlikely to be instantaneous.

Dynamics of distal decoupling

The distal, decoupled behavior of the segregated current can be constrained by the interactions of the current with the sea and hills. While Unalaksa Island provides regular data over more than 20 km, the ridges on the southwest of the caldera stopped rapidly the progression the current. We thus use the speed evolution of the current over the relatively smooth plateau on Unalaska as a reference behavior to understand the effect of the southwestern ridges.

The velocity of the current across Unalaska plateau decays linearly over more than 20 km (section IIIa, Fig. 3.24). Compared to this remarkably regular trend, localities at the base of Unalaska sea cliff are shifted towards higher speeds (section IIIb, Fig. 3.24). Remembering that the current climbed over Unalaska plateau but was smaller than 300 m, we can picture that a fast (~60 m s^{-1}) 200-to-300-m-thick dilute current traveled across the 8-km Unmak Pass and generated a <15 m high tsunami that reached the Unalaska coast (Fig. 3.25a). Tsunami waves motion is commonly considered with the shallow-water approximation, according to which the linear wave speed U_W is expressed as a simple function of the water depth D (e.g., Piatanesi and Tinti 2002):

$$U_W = \sqrt{gD} \tag{10}$$

The strait between Umnak and Unalaska averages 50 m depth, with a maximum of 100 m. The tsunami generated by the entrance of the dense current thus traveled between 22 and 31 m s^{-1}.

This speed is slower than our 54 m s^{-1} estimate for the pyroclastic current (Table 3.2), as expected from stratigraphic evidence.

After reaching Unalaska Island, the cliffs that fringe Unalaska plateau abruptly decelerated the current. Using the range of buoyancy frequencies given by S_T with this estimate of the current height, we maximize the Froude number at 0.25 at the coast (Table 3.2). The height ratio between the cliff and the current is between 0.3 and 0.5. The current is thus subcritical with a modest height ratio, which suggests that the cliff blocked a significant portion of the base of the dilute current (Baines 1995). On the plateau, the current slowed down to about 40 m s^{-1}, remained subcritical with $F_R < 0.1$, and was presumably amputated of its bottom 100 m (Fig. 3.25b). Both the deceleration and the abrupt thinning of the deposit between the coast and the plateau are consistent with an enhanced sedimentation caused by partial blocking of the dilute current. Inversion of the grain size data of the upper layer indicates a similar steep decrease in current speed at the edge of Unalaska plateau (sections IIIc-d, Fig. 3.24). The elevated localities that bear the upper unit indicate that the dilute could was thicker than 300 m. Thus, the portion of the current that deposited the upper unit was also subcritical (Table 3.2), but thicker and slower than its predecessor (Fig. 3.25c).

Our calculations indicate that the current lost speed in a stepwise fashion while crossing the southwestern ridges compared to the ridgeless surface of Unalaska (section IIb, Fig. 3.24). The speed step across the second ridge has a comparable magnitude to that caused by the sea cliff on Unalaska whereas the decay in speed across the third ridge is modest. Importantly, this stepwise behavior was not apparent from the grain size distribution data (see section *Interactions with topography*). The current abruptly decelerated after the fourth ridge to reach a low value of U_{rms}, which is consistent with the transition from a horizontal to vertical motion as the current lifted off. We can estimate the current height to be at least 300 m in order to cross the ridges. Using the minimal buoyancy frequency, we can estimate F_R to be below 0.09 at all localities (Table 3.2). The current was thus always subcritical and likely to be partially blocked by each successive ridge, and we expect these blockings to unload the current in a way similar to that of the west coast of Unalaska. Both this unloading and the presence of higher, more massive relief on the path after the fourth ridge presumably triggered the lift-off of the decelerated dilute current.

Conclusions

Geological and sedimentological data allow us to reconstruct the dynamics of the Okmok II caldera-forming eruption. After a significant period of quiescence, the 2050 ± 50 BP volcanic episode started with an increasingly vigorous Plinian column of rhyodacite, the umbrella cloud of which was diverted by strong SSE winds. After a second steady pulse, the column faded and the eruption stopped for a short period (days to months). The second part of the eruption started with unsteady phreatomagmatic explosions under a strong western wind. As the explosive venting suddenly changed composition from rhyodacitic to andesitic, the eruption became more magmatic. After expelling up to 0.25 km^3 DRE of rhyodacite and up to 0.17 km^3 DRE of andesite, the eruptive regime increased dramatically because of caldera collapse to generate ~29 km^3 DRE of pyroclastic density current deposits that completely covered the northeast part of Umnak Island.

We presented evidence that a single density current that was segregated into a highly concentrated base and an overriding dilute cloud produced the Okmok II deposits. While the basal part produced massive deposits, the dilute cloud sedimented stratified deposits preferentially on hills. Topographic barriers, such as four successive ridges on the southwest of the caldera, reveal the dynamic behavior of these two parts. At first blocked by the first ridge, the basal part thickened until it could overcome the two first ridges. The upstream flux was insufficient for the basal part to cross the third ridge. Meanwhile, the dilute part decoupled and overtook the dense part to successfully cross four ridges. This dilute cloud, however, was subcritical and thus partially affected by the successive ridges, which caused its speed to decrease in a step-wise fashion. The slowed-down cloud buoyantly lifted-off when encountering the more massive relief after the fourth ridge, most likely because the previous partial blockings had significantly unloaded the cloud.

Using the model by Burgisser and Berganz (2002, Chapter 2), we calculated that the density current was traveling at about 60 m s^{-1} when reaching the east coast of Umnak, and was about 300 m thick with a ~120-m dense basal part in which most of its mass was concentrated. Crossing the 8-km wide strait between Umnak and Unalaska Islands decoupled the two parts of the current: while the dense part dove into the waters, the dilute part traveled over the water, preferentially losing dense lithics it transported. On the other side, the cliffs that fringe Unalaska plateau

decelerated abruptly the dilute, subcritical current and blocked its bottom half, thereby enhancing sedimentation near the cliffs. Climbing up the plateau of Unalaska Island, the current slowed to about 40 m s^{-1} and continued its course, decelerating slowly for more than 20 km. Near the end of the eruption, a subsequent portion of the dilute current reached Unalaska, depositing a unit enriched in lithics. This portion was also subcritical, similarly decelerated at the edge of Unalaska plateau, but was thicker (>300 m) and slower (~40 m s^{-1}) than its predecessor. The lithics were preserved within the late part of the current most likely because of the shield provided by extensive scoria rafts between the two islands.

Pyroclastic density current decoupling can be triggered by both sea entrance and topography interaction. While seawater tends to absorb the dense part of the current and the lithics transported by the dilute cloud, topographical relief noticeably decelerates the currents and favors sedimentation by partial or completed blocking. In the case of subcritical, dilute currents, the resulting unloading may reduce drastically the runout distance by triggering an early buoyant lift-off.

Acknowledgments

Table 3.1 Grain size parameters for the stratified facies.

sample	5 wt.% (ϕ)	16 wt.% (ϕ)	50 wt.% (ϕ)	84 wt.% (ϕ)	95 wt.% (ϕ)	sorting (σ)	distance from rim (km)
Idak plateau							
AOK63	-4.8	-3.7	-1.6	0.5	2	2.1	13.5
AOK64	-4.8	-3.6	-1.4	0.5	1.6	2.05	13.5
AOK69	-0.8	0.5	2	3.4	4.3	1.45	16.6
AOK70	-1.4	-1	-0.3	0.5	1.3	0.75	17.5
Kettle Cape – basal unit							
AOK117	-4.4	-3.4	-1.4	0.5	1.7	1.95	11
AOK114	-3.2	-2.4	-0.6	1.7	3.2	2.05	11
Kettle Cape – upper unit							
AOK116	-3.2	-2.4	-0.2	3	4.8	2.7	11
AOK115	-1.1	-0.3	1.6	3.6	4.6	1.95	11
AOK111	-3.4	-2.9	-1	2.6	4.2	2.75	11
Profile IIb							
AOK169	-3.6	-2.9	-1.6	-0.2	0.8	1.35	12.3
AOK170	-3.4	-2.7	-1.3	0.5	2	1.6	14.4
AOK177	-2.9	-2.1	-0.8	0.8	2.7	1.45	19.7
AOK175	0.6	1.2	2.8	4.2	5.5	1.5	23.7
Profile IIIa – upper unit							
AOK143	-3.4	-2.8	-1.7	-0.5	0.7	1.15	19.9
AOK146	-2.9	-2.2	-1.4	-0.5	0.3	0.85	26
AOK151	-2.3	-1.8	-1	-0.2	0.2	0.8	32.6
AOK149	-2.3	-1.8	-1	-0.2	0.1	0.8	33.2
AOK153	-1.9	-1.2	-0.5	0.4	0.6	0.8	40.3
Profile IIIb – upper unit							
AOK142	-3.8	-3.1	-2.1	-1	-0.2	1.05	21.5
AOK189	-3.2	-2.8	-1.8	-0.9	-0.2	0.95	25.7
Profile IIIc – basal unit							
AOK144	-2.9	-2.2	-0.9	1.7	3.5	1.95	19.9
AOK145	-2.9	-2.1	-1	1.7	3.5	1.9	22
AOK147	-2.1	-1	0.2	1.3	2	1.15	26
Profile IIId – basal unit							
AOK150	-2.4	-1.5	-0.7	0.3	2.7	0.9	36.8
AOK154	-1.2	-0.4	0.6	1.5	2.5	0.95	43.1

Table 3.2 Dynamic parameters for the stratified facies.

sample	ρ avg (kg m^{-3})	U_{rms} (m s^{-1})	δi (m)	mean speed (m s^{-1})	current height (m)	F_R
Idak plateau						
AOK64	1950	15	5-300	60	200-300	<0.25
AOK69	1350	1.5	0.01-2.5	6	200-300	<0.01
AOK70	1250	6	2.5-10	24	200-300	<0.03
Kettle Cape – basal unit						
AOK117	2050	15.5	5-300	62	>100	<0.75
AOK114	1950	9.5	0.75-75	38	>100	<0.19
Kettle Cape – upper unit						
AOK116	1750	7	0.1-50	28	>100	<0.13
AOK115	1450	2	0.01-5	8	>100	<0.01
AOK111	1250	9	0.1-50	36	>100	<0.13
Profile IIb						
AOK169	1150	12.5	5-75	50	>200	<0.09
AOK170	1150	10.5	2.5-50	42	>200	<0.06
AOK177	1450	9	1-50	36	>200	<0.06
AOK175	1450	0.5	0.01-0.5	2	>200	0
Profile IIIa – basal unit						
AOK143	1150	13	7.5-75	52	75-200	<0.25
AOK146	1150	11	7.5-50	44	100-200	<0.13
AOK151	1150	9	5-25	36	50-200	<0.13
AOK149	1150	9	5-25	36	50-200	<0.13
AOK153	1150	6.5	2.5-25	26	50-200	<0.13
Profile IIIb – basal unit						
AOK142	1150	16	10-100	64	150-300	<0.17
AOK189	1150	13.5	10-75	54	150-300	<0.13
Profile IIIc – upper unit						
AOK144	1650	10	7.5-50	40	>300	<0.04
AOK145	1350	9.5	2.5-50	38	>50	<0.25
AOK147	1250	6	0.75-10	24	>100	<0.03
Profile IIId – upper unit						
AOK150	1250	8	0.75-25	32	>200	<0.03
AOK154	1550	4	0.5-7.5	16	>50	<0.04
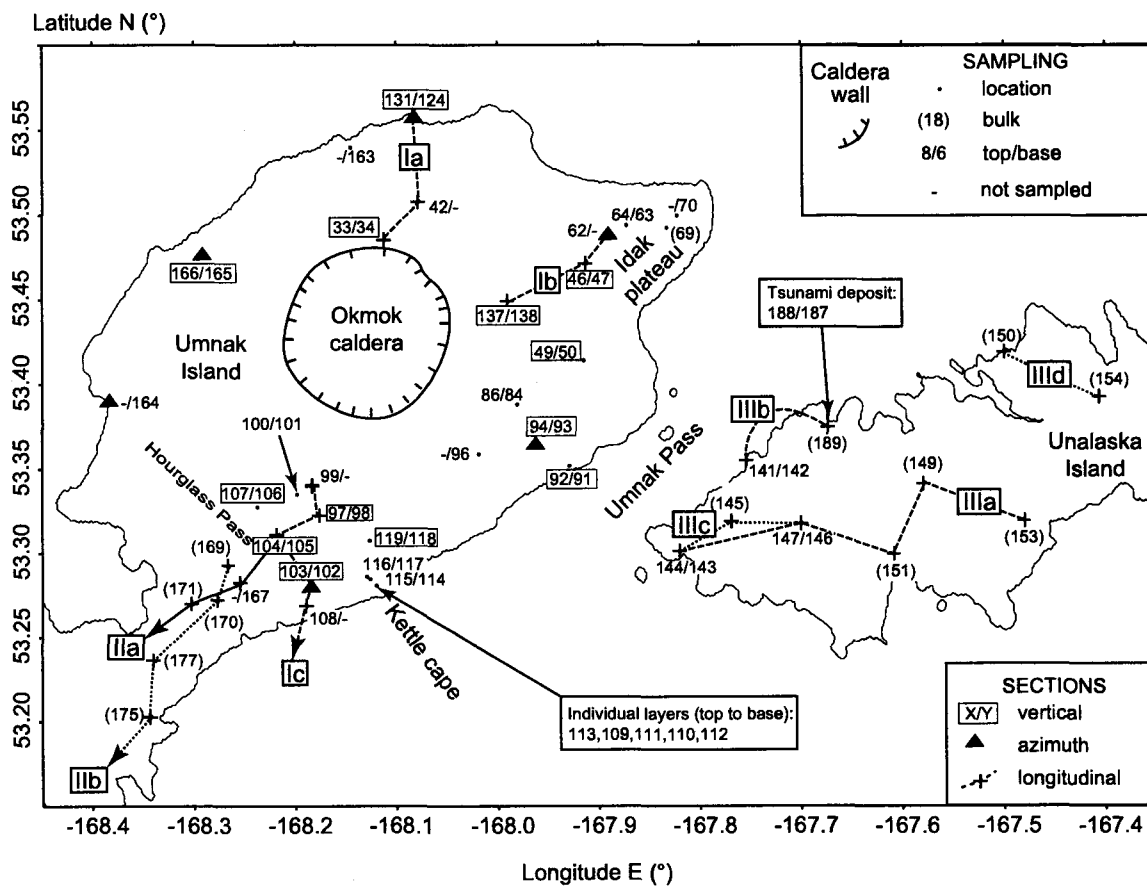
Figure 3.1 Sample localities of the pyroclastic current deposits. Geographic names are also indicated. Localities with an asterisk have been used to study local vertical variations and the corresponding grain size data are reported in Fig. 3.8. Data of the azimuth section are in Fig. 3.10, sections Ia-c in Fig. 3.12, sections IIa-b in Fig. 3.15, sections IIIa-b in Fig. 3.16, and sections IIIc-d in Fig. 3.18.
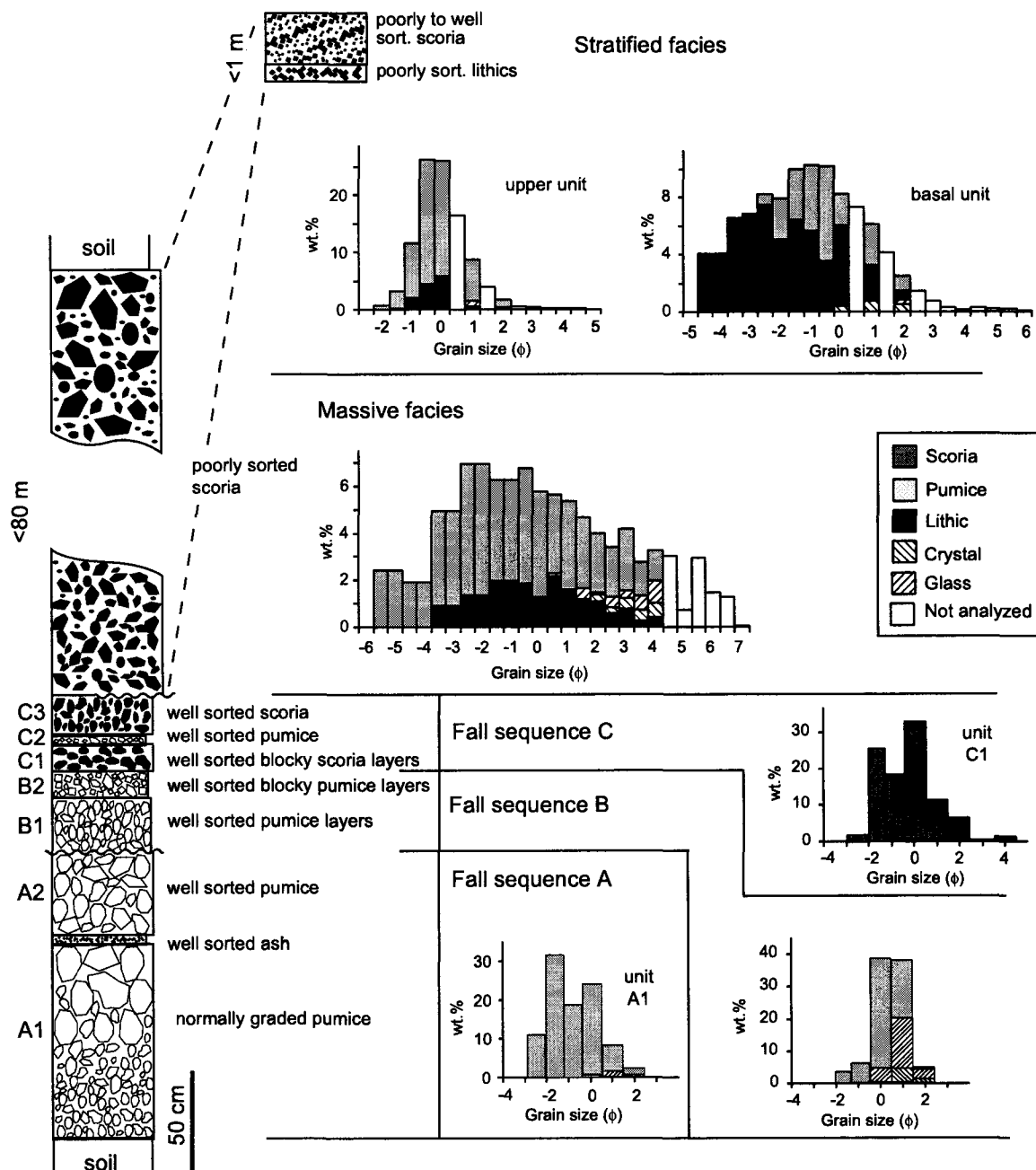
Figure 3.2 Composite stratigraphic section of the Okmok II eruptive products. Filled symbols are scoria; open symbols are pumice. Fall deposits are scaled to their maximum thickness, whereas the massive and stratified facies are not to scale. Representative grain-size distribution with componentry are given for the fall sequences A (A1, AOK6), B (B2, AOK22), C (C1, AOK10), the massive facies (AOK104), and the stratified facies (AOK117 for the basal unit and AOK70 for the upper unit). Samples AOK6 and AOK10 are at the location AOK131 while the sample AOK22 is at the location AOK86 (see Fig. 3.1 for locations).
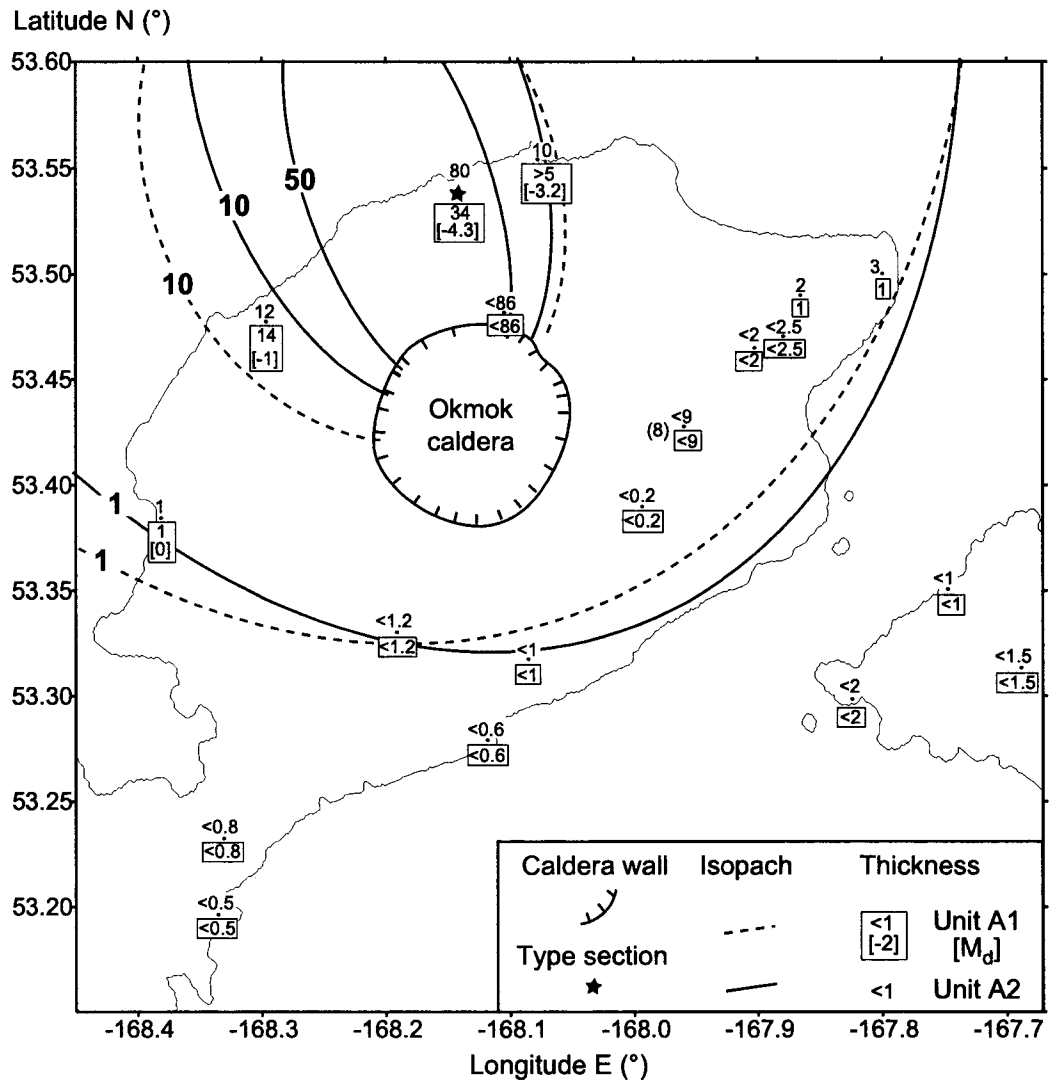
Figure 3.3 Thickness distribution of fall sequences A1 and A2. Signs > and < indicate minimum and maximum thickness, respectively. Isopachs are in centimeters; the star locates the type section, and the median grain size M_d (ϕ) is given for some locations.
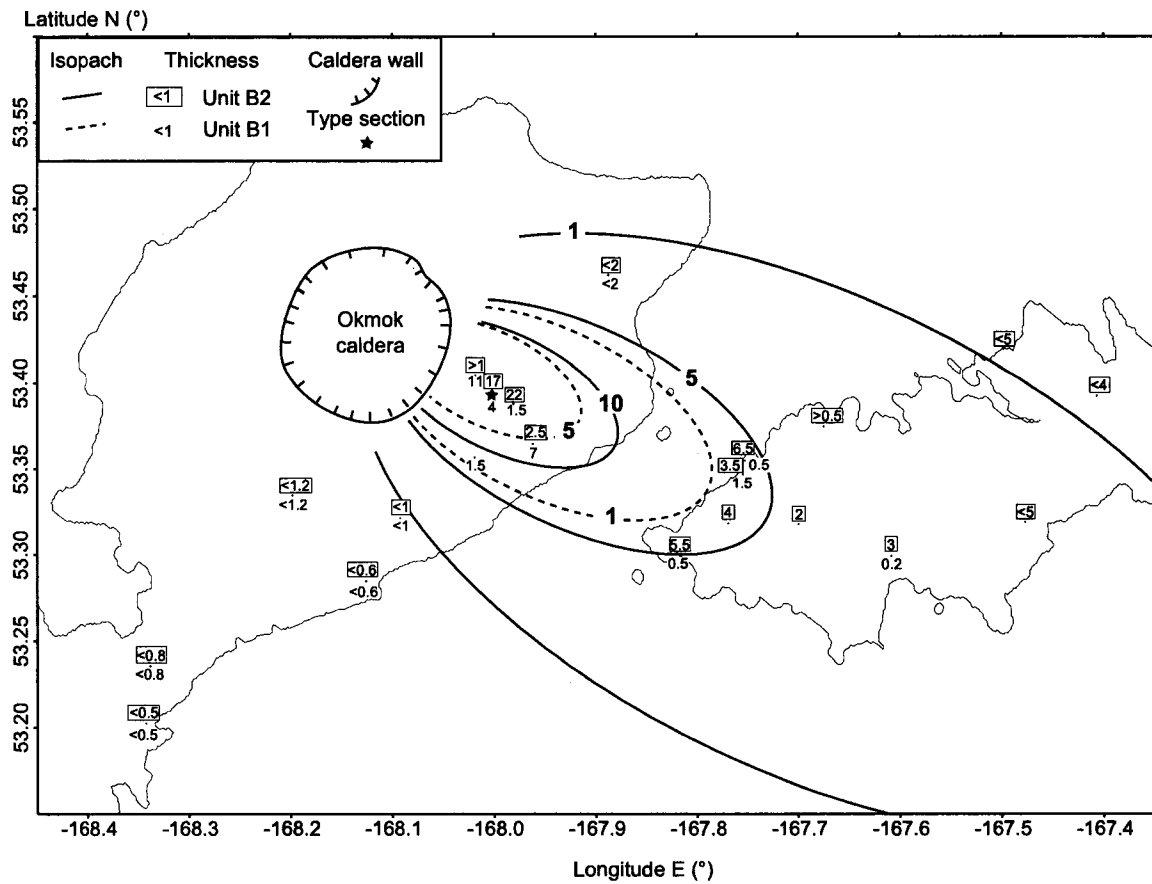
Figure 3.4 Thickness distribution of fall sequences B1 and B2. Signs > and < indicate minimum and maximum thickness, respectively. Isopachs are in centimeters and the star locates the type section.
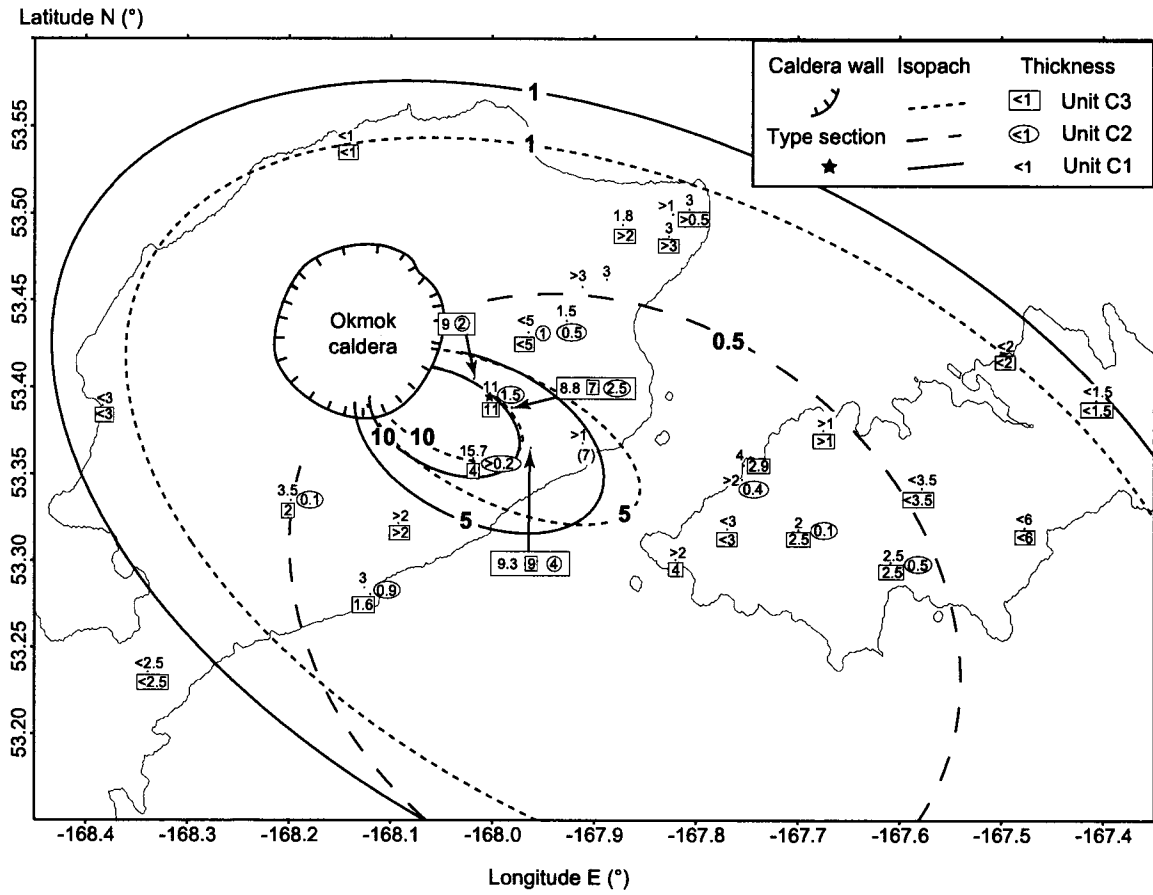
Figure 3.5 Thickness distribution of fall sequences C1, C2, and C3. Signs > and < indicate minimum and maximum thickness, respectively. Isopachs are in centimeters.
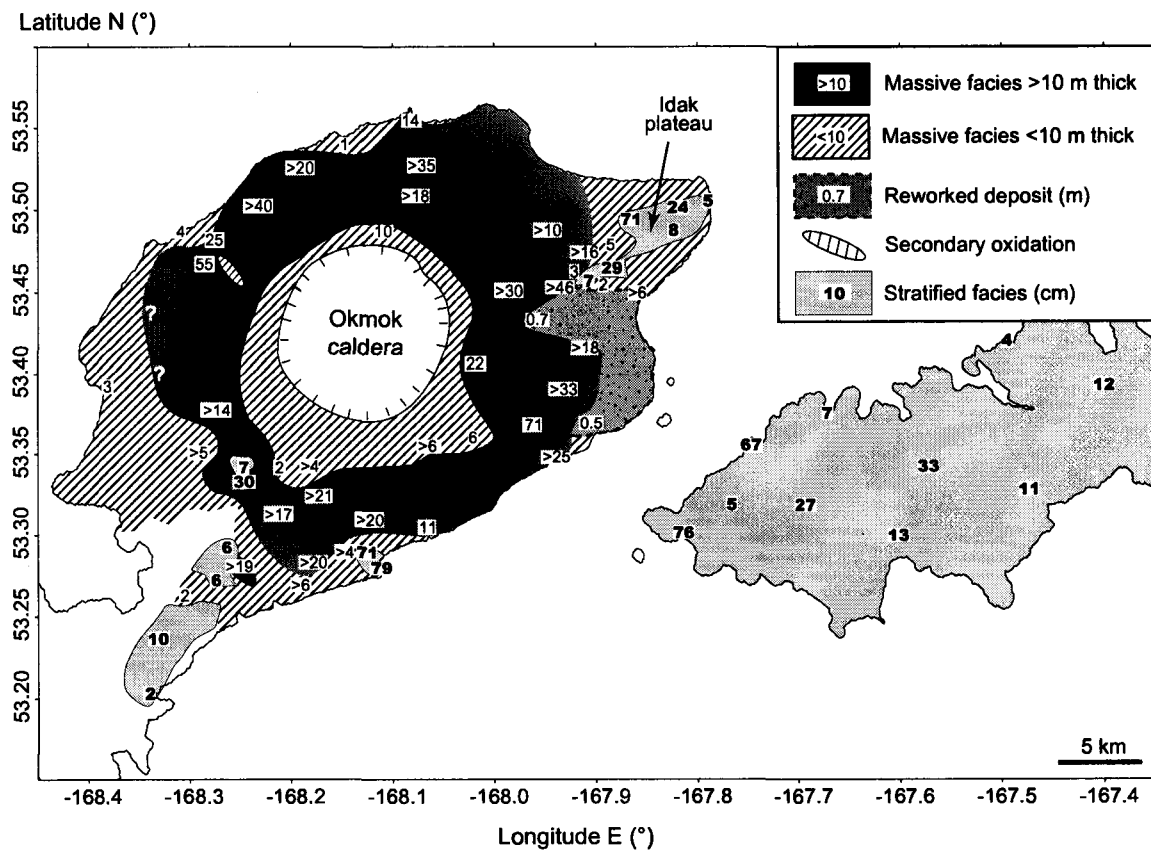
Figure 3.6 Thickness distribution of the pyroclastic current deposits. Massive facies, stratified facies, and post-depositional reworking are indicated. Massive facies thickness is in meters, while stratified facies thickness is in centimeters (bold numbers). The sign > indicates minimum thickness.

A.

B.
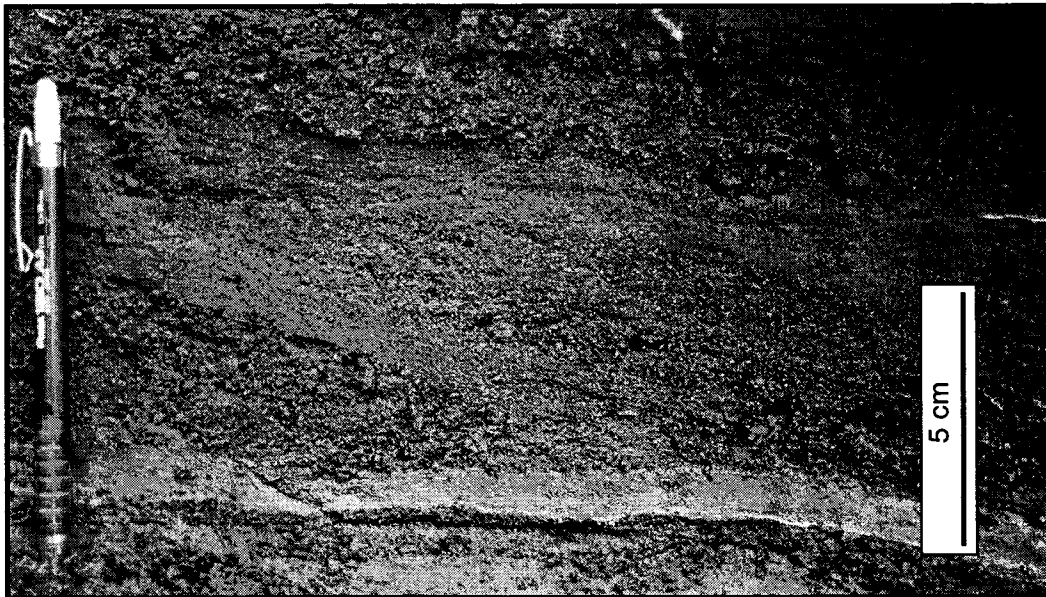
Figure 3.7 Field examples of the pyroclastic deposits. **a.** Massive facies near Hourglass Pass (AOK 103, see Fig. 3.1 for locations). Note the flat upper surface of the ~ 25 m thick deposit. **b.** Stratified facies at locality AOK69. Note the cross bedding inclined from the upper left to the lower right of the photograph.
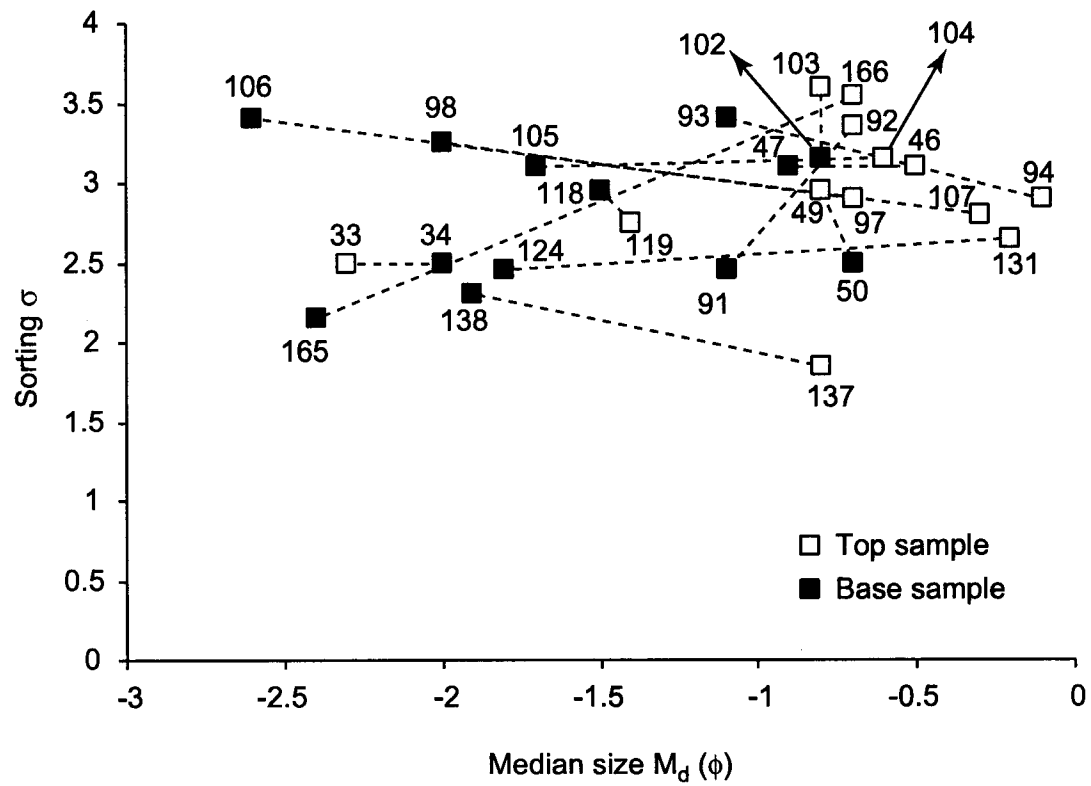
Figure 3.8 Changes in sorting (σ) with median grain size for sample pairs within the massive facies of the pyroclastic current deposits. Basal samples (filled symbols) are linked to the top samples (open symbols).
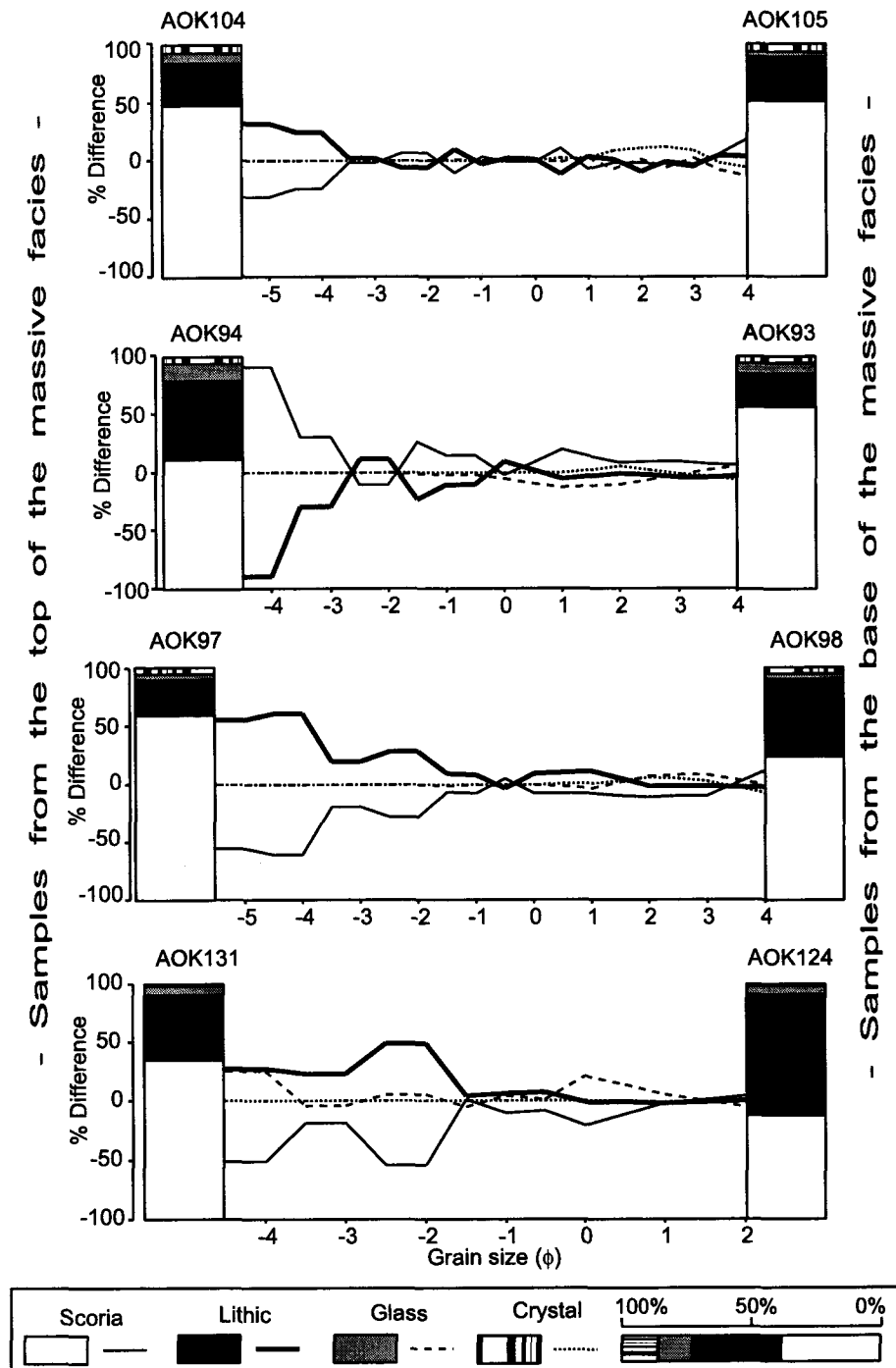
Figure 3.9 Componentry variation with grain size within the massive facies of the pyroclastic current deposits. The samples on the left-hand side are from the top of the deposit, whereas the samples on the right-hand side are from the base (see Fig. 3.1 for samples locations).
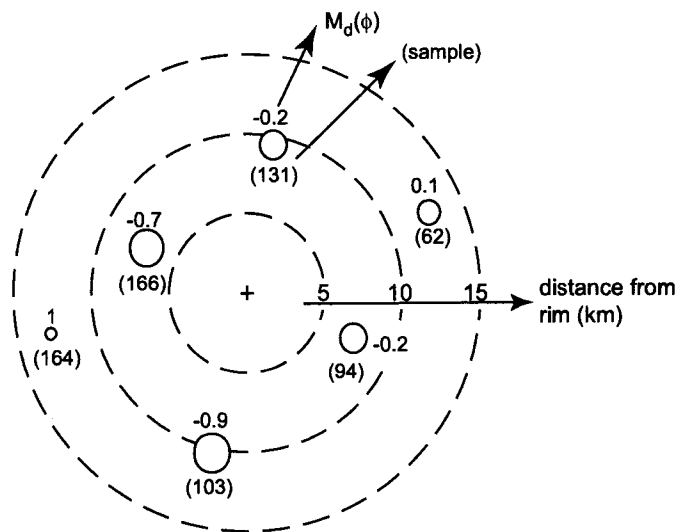
Figure 3.10 Changes in median grain size with distance and azimuth from the caldera rim. Data for the azimuth section (see Fig. 3.1 for location).
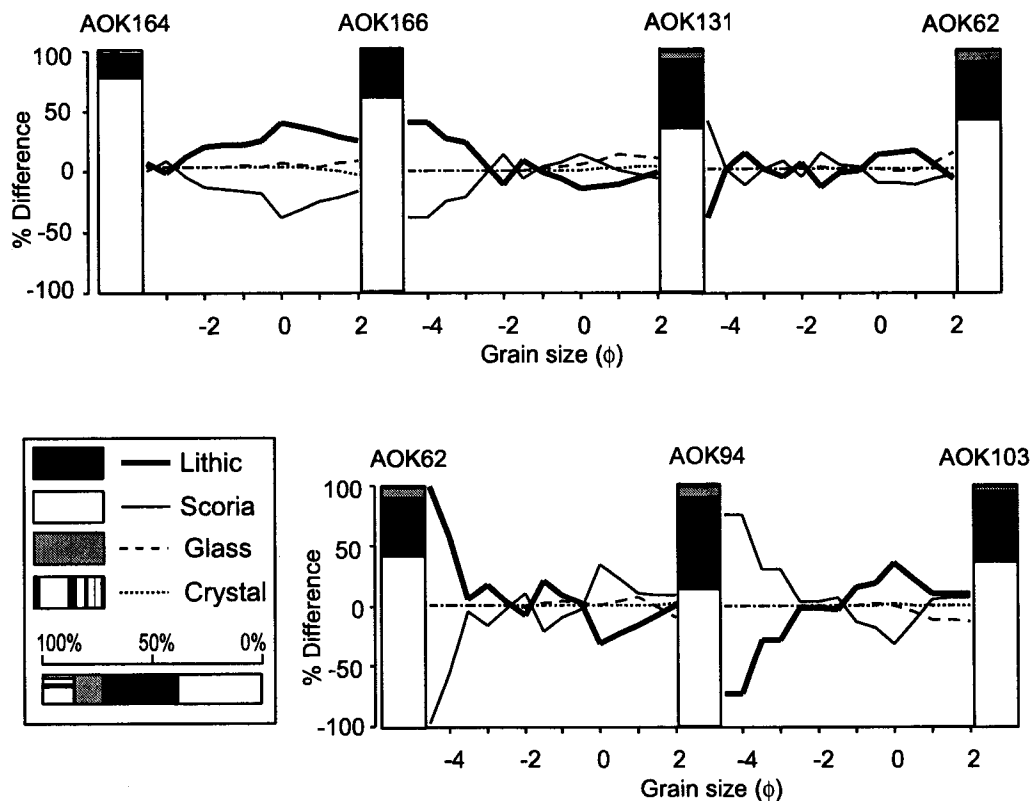
Figure 3.11 Componentry variation with grain size of the azimuth section. See Fig. 3.1 for section location.
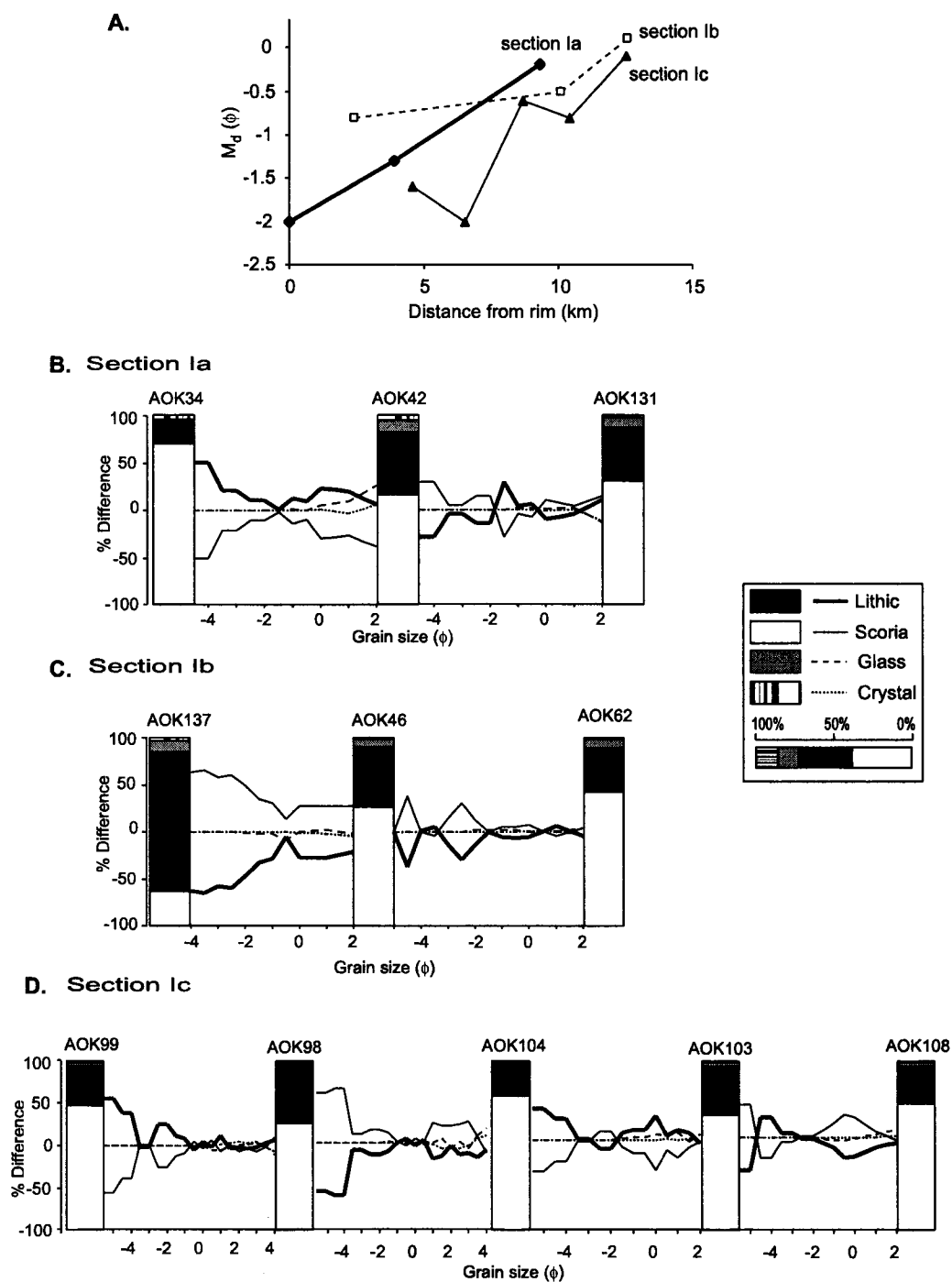
Figure 3.12 Grain size and componentry of the massive facies with distance from source. **a.** Changes in median grain size with distance from the caldera rim for sections Ia-c (see Fig. 3.1). **b.** Componentry variation with grain size of section Ia. **c.** Componentry variation with grain size of section Ib. **d.** Componentry variation with grain size of section Ic.

A. Basal unit

B. Kettle Cape - individual beds

Kettle Cape

-0.5 ◆ 114

M_d (ϕ)

-1

Idak plateau

◆ 117 ◇ 64

-1.5 ◇ 63

-2

10 15

Distance from rim (km)

3

111 □ 112 □ 116 □ upper unit

2.5 □ 110

Sorting σ 109 □ □ 113

2 117 ◆ ◆ 114 115 □

basal unit

1.5

1

-2 -1.5 -1 -0.5 0 0.5 1 1.5

M_d (ϕ)

C.

AOK117 AOK116

Basal unit - bulk samples

100

50

% Difference

0

-50

-100

-4 -3 -2 -1 0 1 2

Grain size (ϕ)

AOK114 AOK115

100

50

% Difference

0

-50

-100

-3 -2 -1 0 1 2

Grain size (ϕ)

Upper unit - bulk samples

■ Lithic

□ Scoria

▨ Glass

▤ Crystal

100% 50% 0%

D. Kettle Cape - upper unit, individual beds

AOK113 AOK109 AOK111 AOK110 AOK112

100

50

% Difference

0

-50

-100

Top Base

-2 0 2 4 -2 0 2 -2 0 2 -2 0 2

Grain size (ϕ)

Figure 3.13 Grain size and componentry of the stratified facies. **a.** Changes in median grain size with distance from the caldera rim for the basal, lithic-rich unit. **b.** Changes in sorting with median grain size of individual layers within the stratified facies. **c.** Componentry variation with grain size of the basal unit. **d.** Componentry variation with grain size of individual layers within the upper unit at Kettle Cape.

A. South side of Idak plateau

uphill

stratified facies

lithic-rich layer

fall units

massive facies

fall units

0.2 m

370 m

5 m

B.

massive facies | stratified facies | lithic-rich layer | scoria accumulation
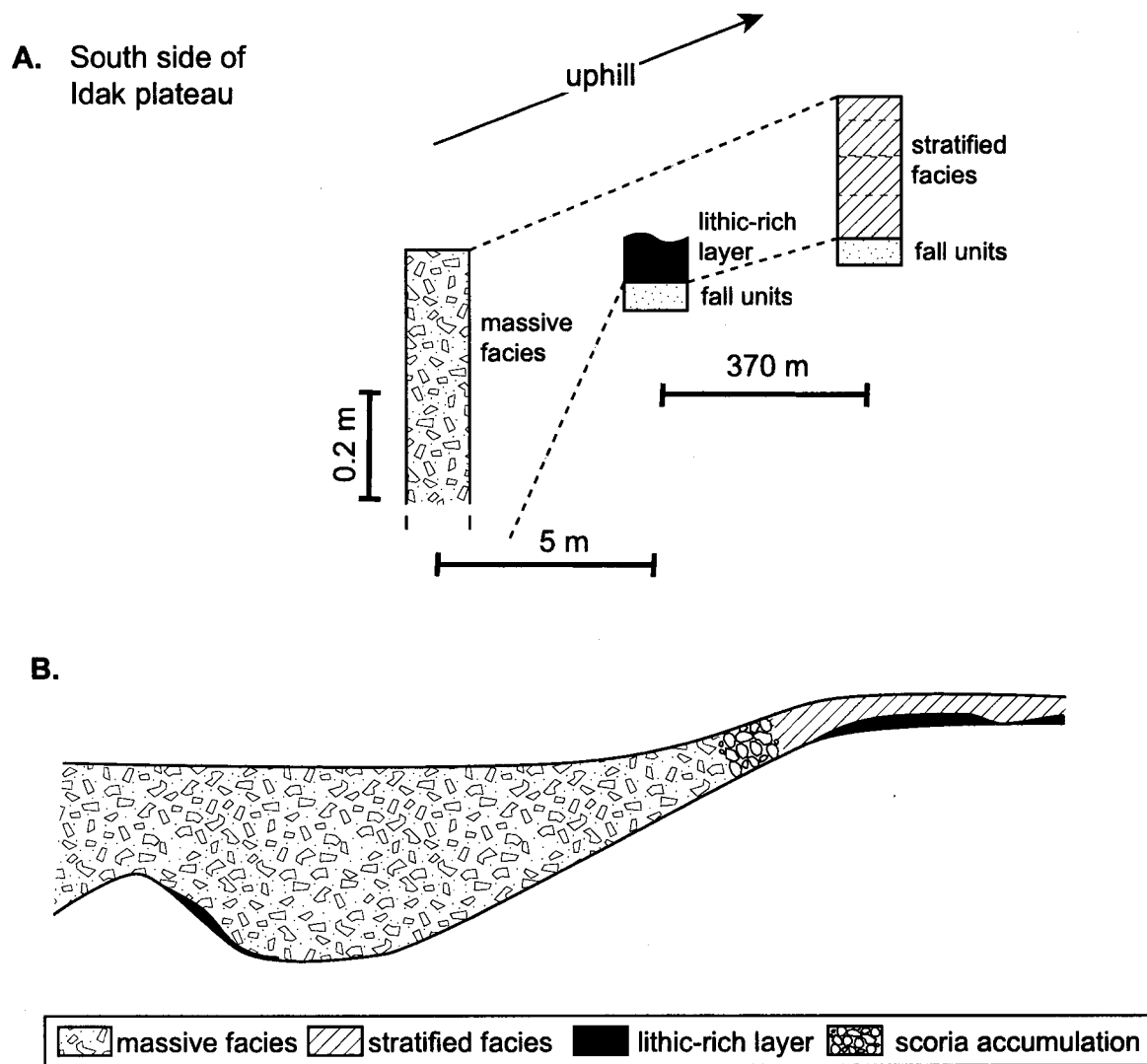
Figure 3.14 Lateral facies variations within the pyroclastic current deposits. a. Stratigraphic correlation between massive and stratified facies on the south side of Idak plateau. b. Schematic interpretation of the lateral changes in facies.
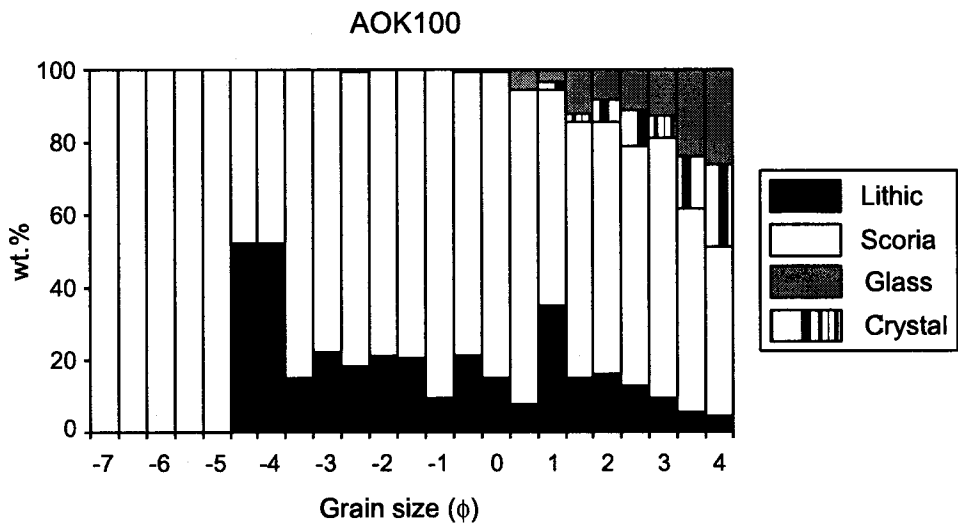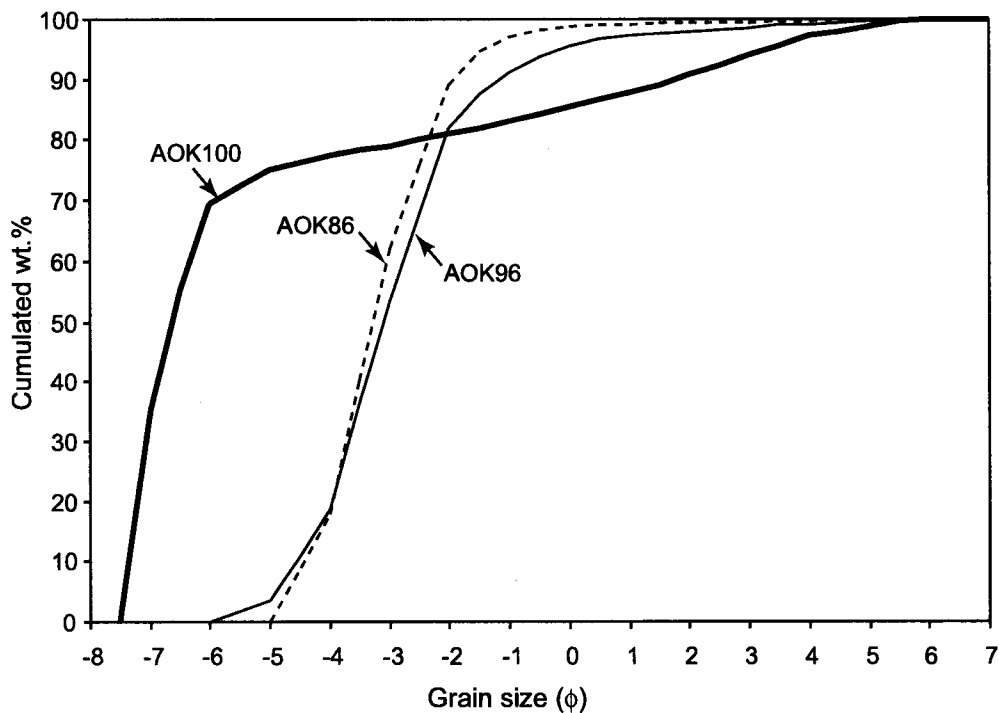
Figure 3.15 Grain size and componentry of scoria accumulations within the pyroclastic current deposits. Componentry are normalized wt.%. See Fig. 3.1 for sample location.
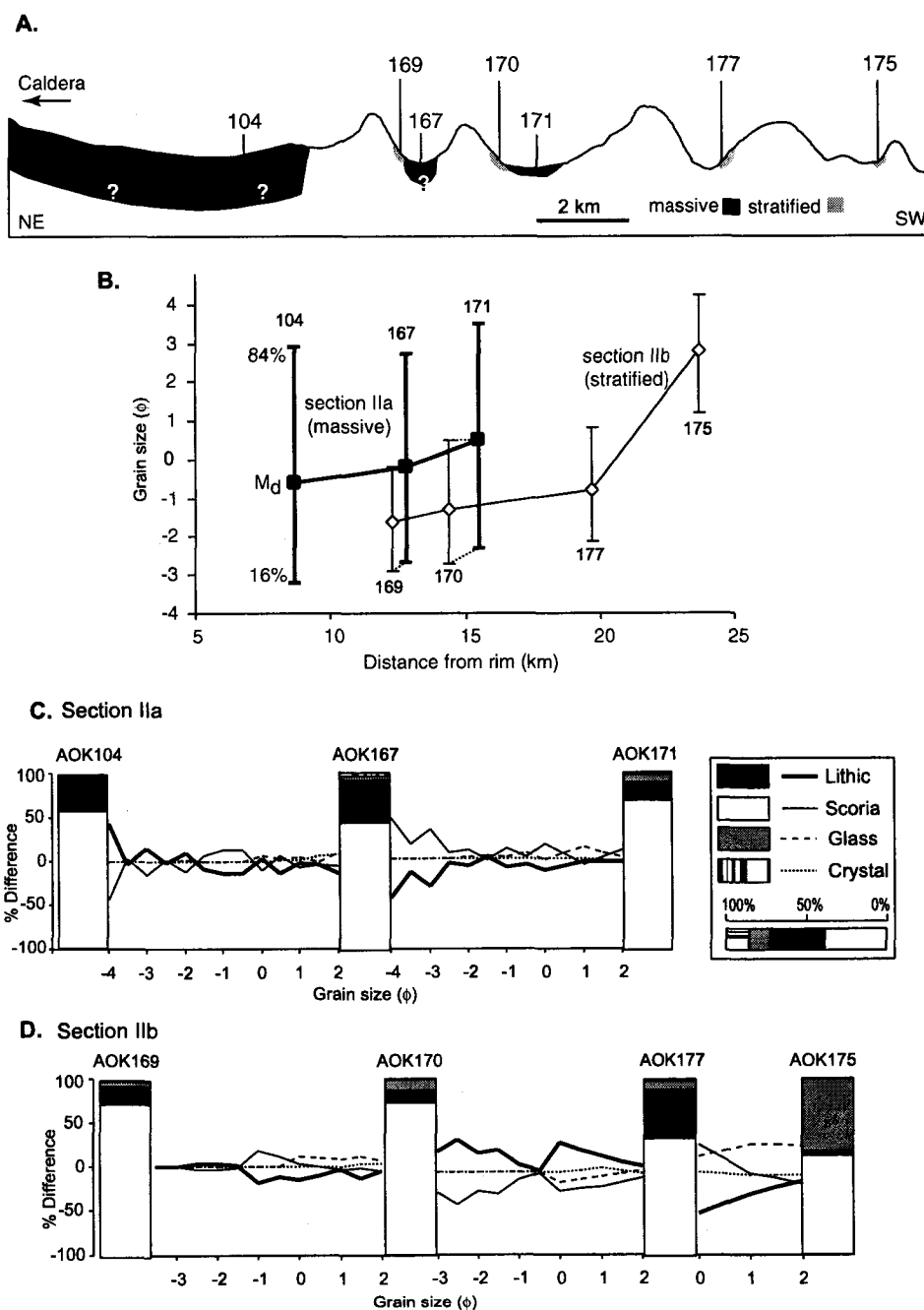
Figure 3.16 Grain size and componentry of the massive and stratified facies on the southwest of Okmok. Massive and stratified facies data are grouped in sections IIa and IIb, respectively (see Fig. 3.1) **a.** Cross section following the position of section IIb across four ridges with sample locations. **b.** Changes in median grain size with distance from the caldera rim. **c.** Componentry variation with grain size of the massive facies. **d.** Componentry variation with grain size of the stratified facies.
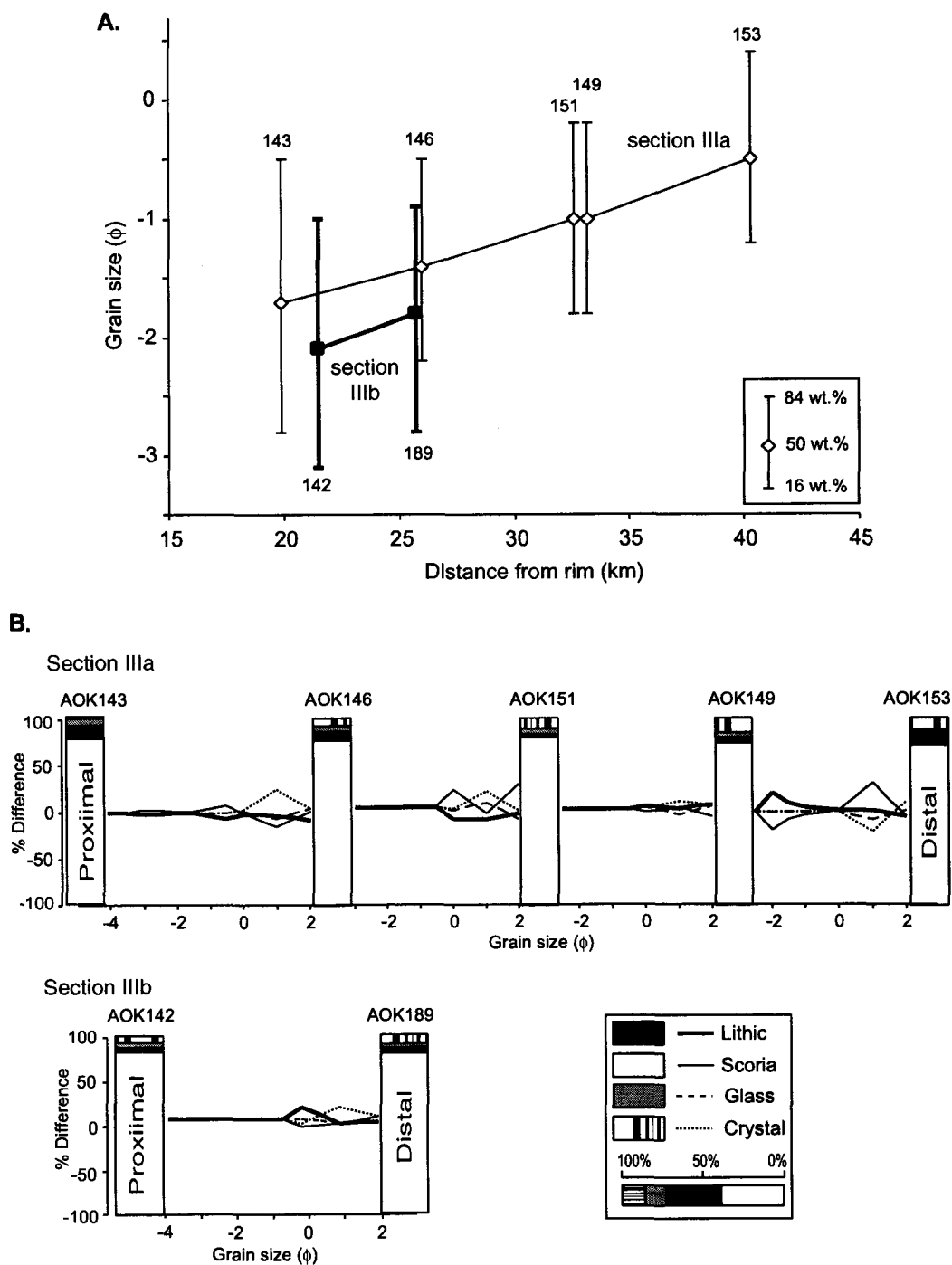
Figure 3.17 Grain size and componentry of the basal unit of the stratified facies on Unalaska Island. Data are grouped in section IIIa at shore and IIIb on the plateau (see Fig. 3.1) **a.** Changes in median grain size with distance from the caldera rim. **b.** Componentry variation with grain size.
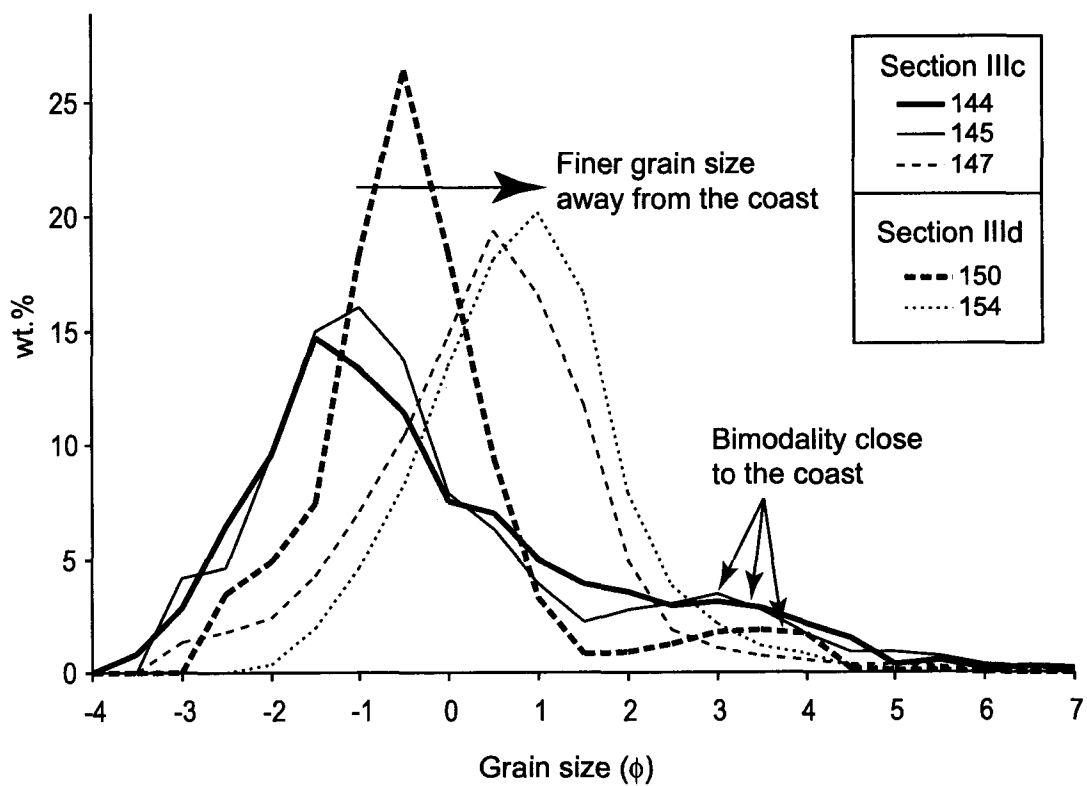
Figure 3.18 Cumulative grain size distribution of the upper unit of the stratified facies on Unalaska Island. Note that the bimodality of the coarser samples coincides with their proximity to the coast.

A.

B.
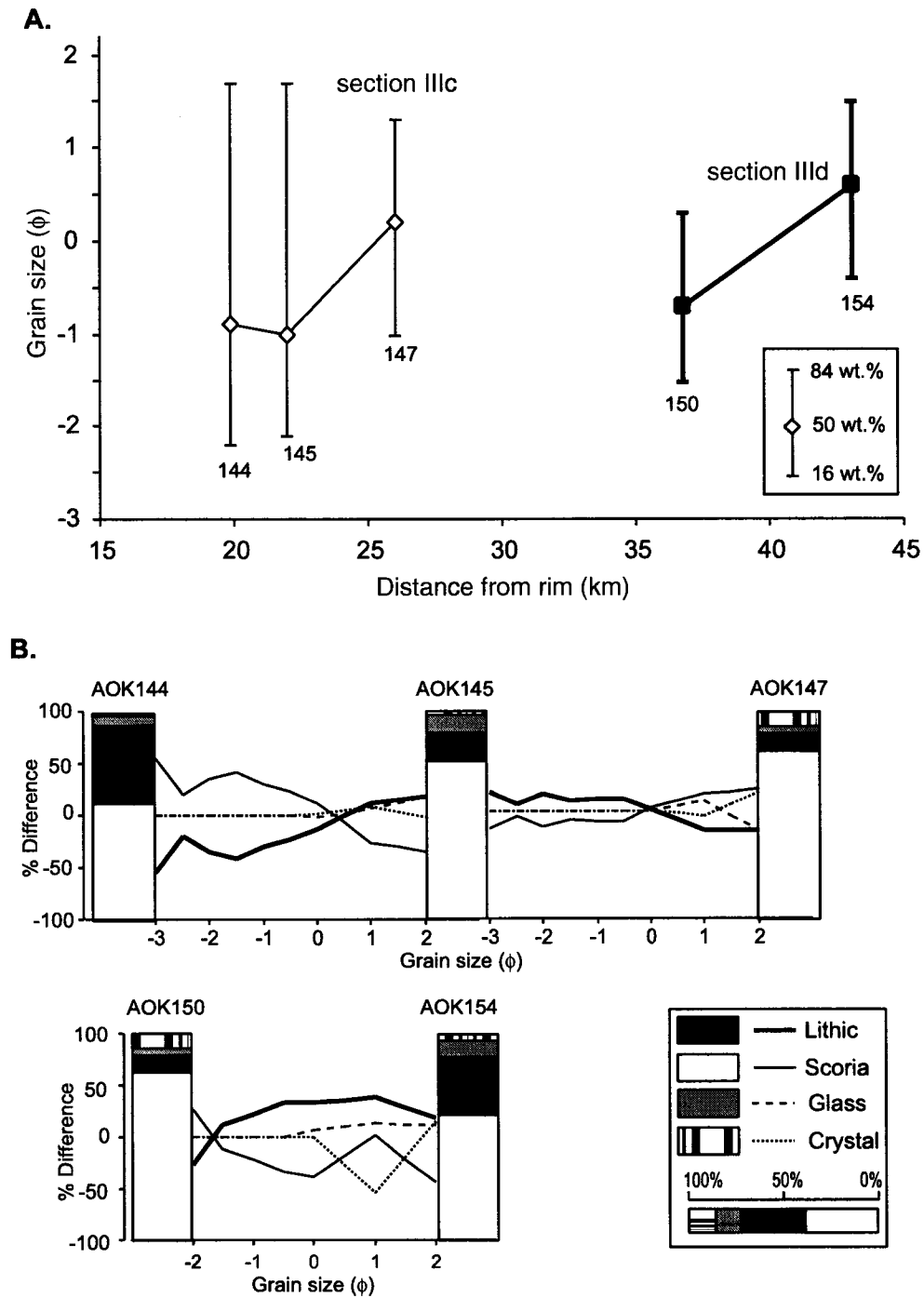
Figure 3.19 Grain size and componentry of the upper, lithic-rich unit of the stratified facies on Unalaska Island. Data are grouped in section IIIc at shore and IIId on the plateau (see Fig. 3.1) **a.** Changes in median grain size with distance from the caldera rim. **b.** Componentry variation with grain size.
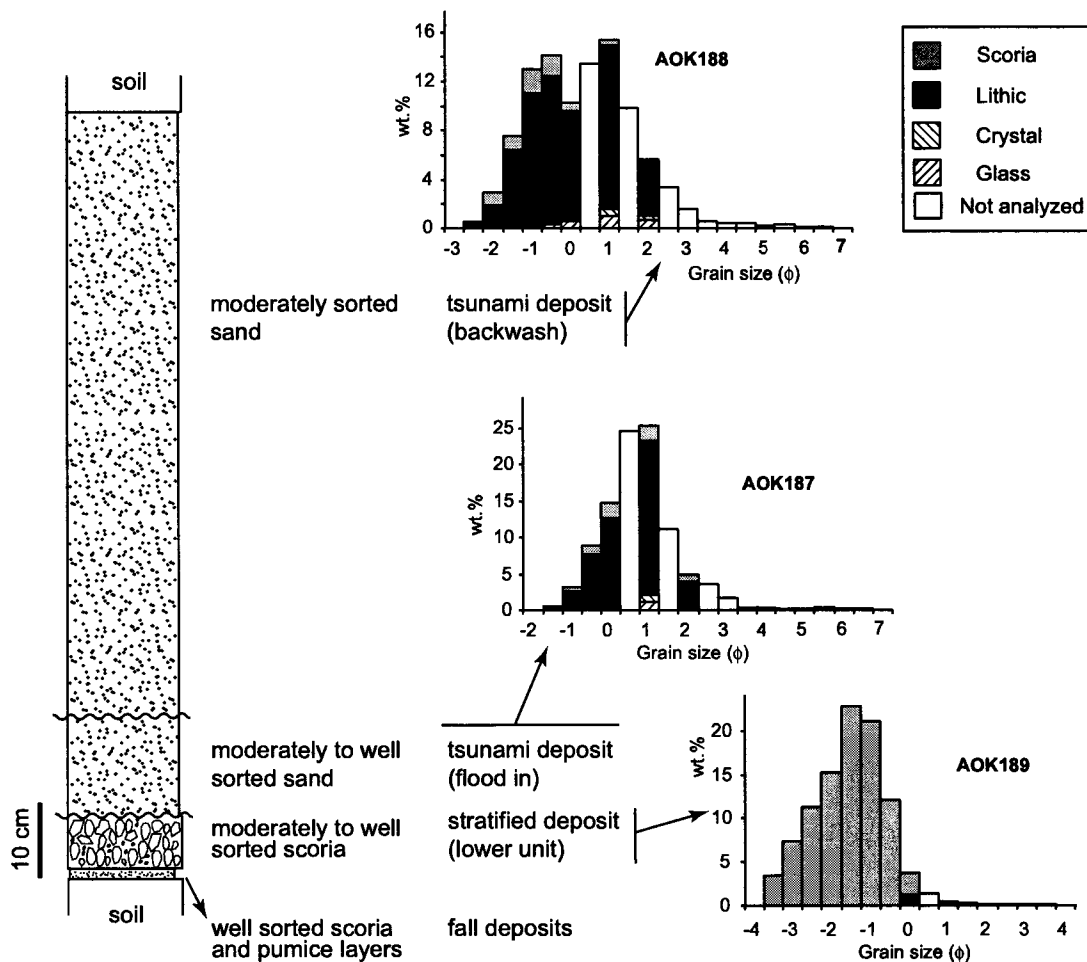
Figure 3.20 Stratigraphy of the western coast of Unalaska with representative grain size distribution and componentry. The two upper sandy units were only found below 15 m of altitude (see Fig. 3.1 for samples location).
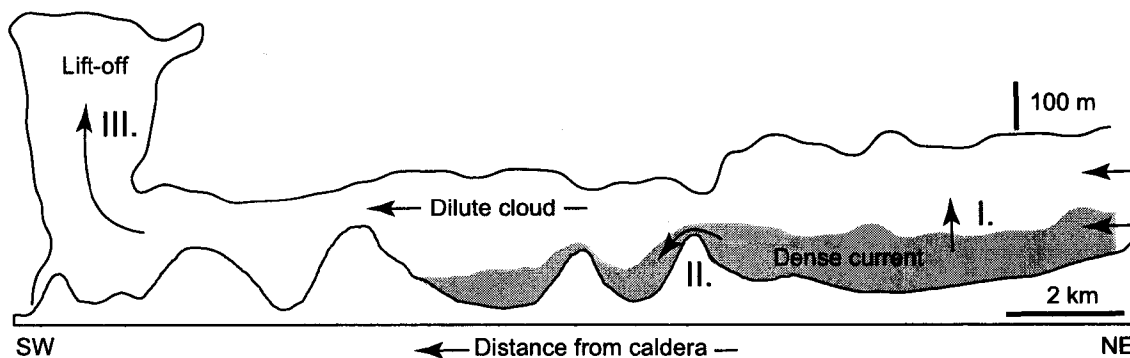
Figure 3.21 Schematic evolution of the pyroclastic density current across the four ridges of section IIb. See Fig. 3.1 for section location.
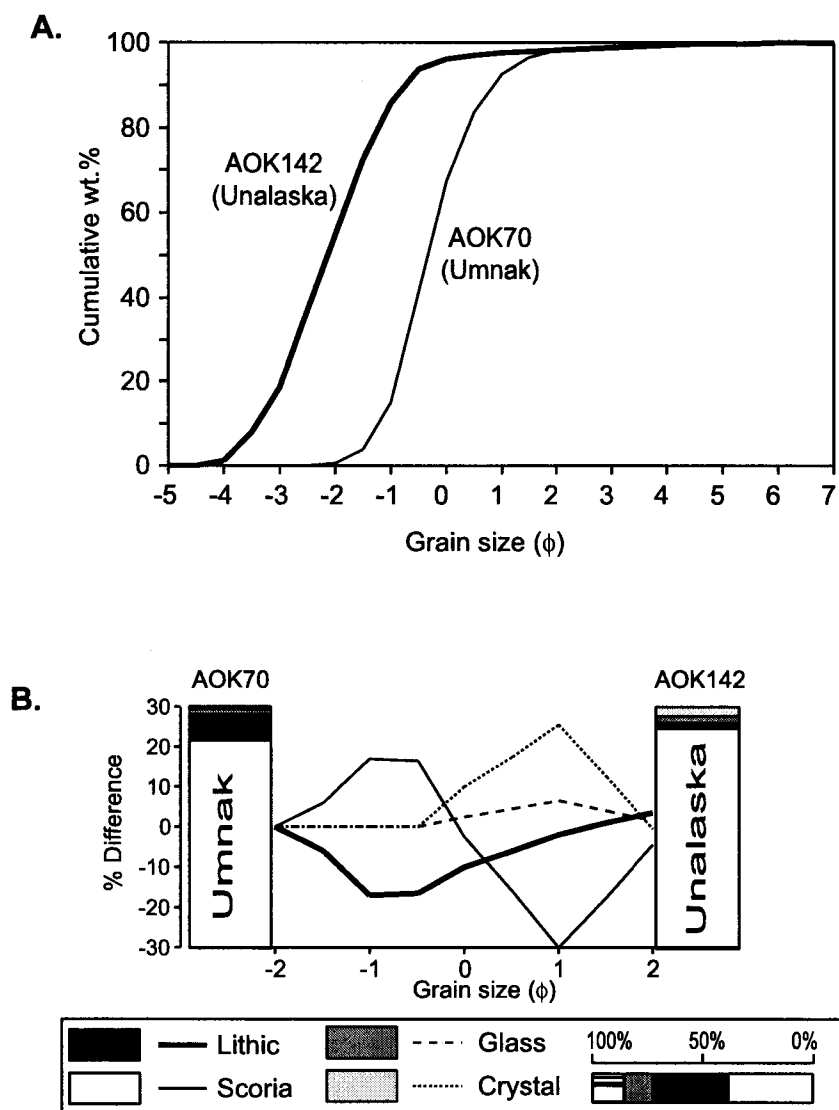
Figure 3.22 Grain size and componentry changes of the stratified facies across Umnak Pass. See Fig. 3.1 for samples location. **a.** Grain size distribution. Note the similar sorting. **b.** Componentry variation with grain size.
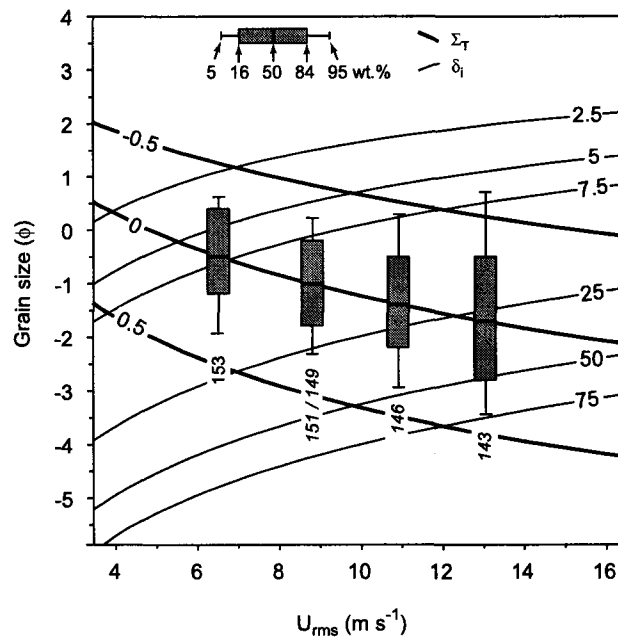
Figure 3.23 Example of backward modeling of field data using a U_{rms} vs. grain size plot. Samples are from the section IIIa (see text). Thick lines are log (Σ_T), thin lines are eddy maximum size δ_i, and boxes represent grain size distributions. Variables used are μ=1.5×10⁻⁵ Pa s, υ=3×10⁻⁵ m² s⁻¹ (air at 300 °C), and ρ_p = 1150 kg m⁻³.
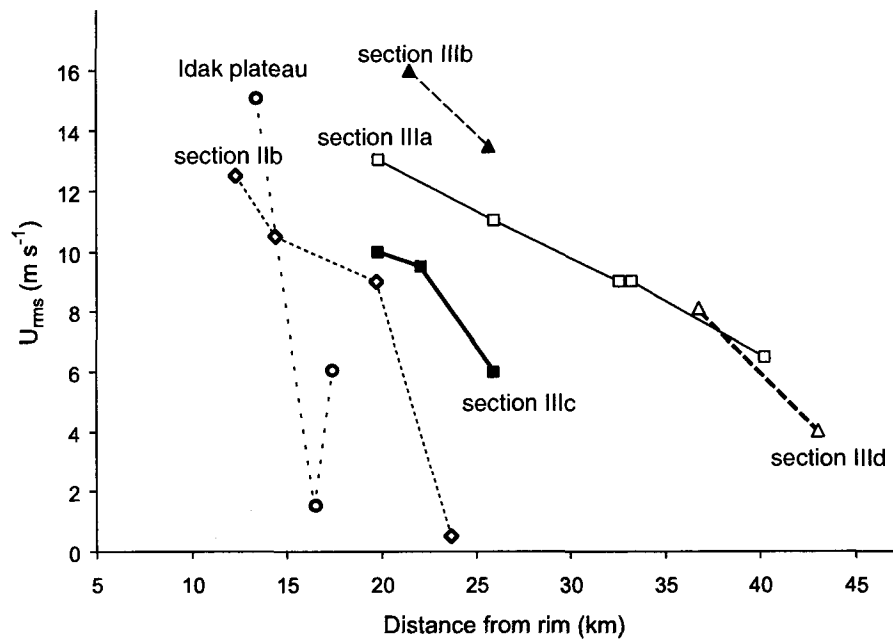
Figure 3.24 Root-mean square velocities U_{rms} of the dilute pyroclastic current for various sections around Okmok. See Fig. 3.1 for sections location.

A.

60 m/s

Dilute current 250 m

Dense current 250 m

Massive unit

Dense current 120 m

Decoupling at sea entrance

55 m/s, 250 m

Tsunami
25 m/s, <15 m

Strat. basal unit

200 m

2 km

W

E

Umnak   Umnak Pass   Unalaska

B.

40 m/s, 150 m

Strat. basal unit

Blocking dense part

Tsunami deposit

?

W   E

C.

25 m/s

40 m/s, >300 m

Strat. upper unit

?

Scoria rafts

W   E
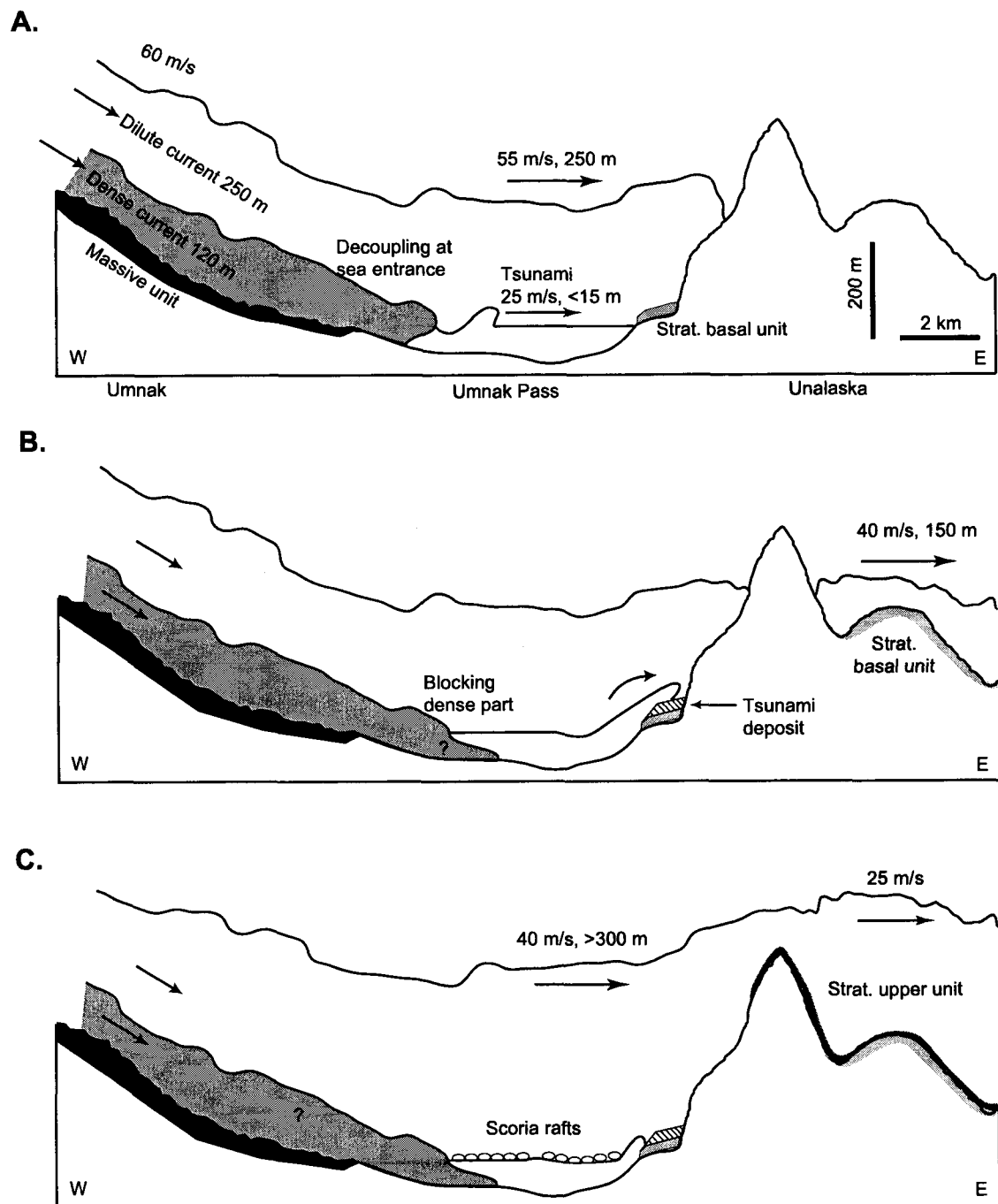
Figure 3.25 Schematic evolution of the pyroclastic density current across Umnak Pass. a. Decoupling of the dilute cloud, which reach Unalaska before the tsunami caused by the entrance of the dense part into the sea (see text). b. Partial blocking of the dilute cloud be Unalaska sea cliffs and emplacement of the tsunami deposits. c. Second, thicker dilute cloud reaching Unalaska, presumably enriched in lithics because of extensive scoria rafts on Umnak Pass.

Appendix 3

This appendix contains the geographical and sedimentological data of the samples collected around Okmok volcano. Sample locations (Table 3.A1) were obtained by GPS, grain-size distributions (Table 3.A2) were obtained by sieving, and componentries (Table 3.A3) were obtained by counting, as detailed in the section *Methods* of chapter 3. Samples locations are given in the map of Fig. 3.1.

Table 3.A1: Sample locations and sampling details. The coordinates are given in decimal degrees, and the samples locations are shown on Fig. 3.1

Sample	Longitude (°E)	Latitude (°N)	Position	Notes
AOK6	-168.08158	53.55703	bulk	fall A1
AOK10	-168.08158	53.55703	bulk	fall C2
AOK22	-167.98082	53.38802	bulk	fall B2
AOK33	-168.11133	53.48553	top	massive
AOK34	-168.11133	53.48553	base	massive
AOK42	-168.07947	53.50728	top	massive
AOK46	-167.91177	53.47148	top	massive
AOK47	-167.91177	53.47148	base	massive
AOK49	-167.91500	53.41417	top	massive
AOK50	-167.91500	53.41417	base	massive
AOK62	-167.89242	53.48825	top	massive
AOK63	-167.87212	53.49375	base	stratified
AOK64	-167.87212	53.49375	top	stratified
AOK69	-167.83232	53.49235	bulk	stratified
AOK70	-167.82275	53.49965	base	stratified
AOK84	-167.98082	53.38802	base	scoria accumulation
AOK86	-167.98082	53.38802	top	scoria accumulation
AOK91	-167.92897	53.35172	base	massive
AOK92	-167.92897	53.35172	top	massive
AOK94	-167.96208	53.36487	top	massive
AOK93	-167.96208	53.36487	base	massive
AOK96	-168.01852	53.35877	base	massive
AOK97	-168.17662	53.32240	top	massive
AOK98	-168.17662	53.32240	base	massive
AOK99	-168.18345	53.34073	top	massive
AOK100	-168.19825	53.33485	top	scoria accumulation
AOK101	-168.19825	53.33485	base	lithic-rich layer
AOK102	-168.18222	53.28132	base	massive
AOK103	-168.18222	53.28132	top	massive
AOK104	-168.21648	53.31087	top	massive
AOK105	-168.21648	53.31087	base	massive
AOK106	-168.23740	53.32740	base	massive
AOK107	-168.23740	53.32740	top	massive

Table 3.A1 continued

Sample	Longitude (°E)	Latitude (°N)	Position	Notes
AOK108	-168.18853	53.26887	top	massive
AOK109	-168.11985	53.28085	above AOK111	stratified, individual layer
AOK110	-168.11985	53.28085	above AOK112	stratified, individual layer
AOK111	-168.11985	53.28085	above AOK110	stratified, individual layer
AOK112	-168.11985	53.28085	base	stratified, individual layer
AOK113	-168.11985	53.28085	top, above AOK109	stratified, individual layer
AOK114	-168.12597	53.28457	base	stratified
AOK115	-168.12597	53.28457	top	stratified
AOK116	-168.12923	53.28602	top	stratified
AOK117	-168.12923	53.28602	base	stratified
AOK118	-168.12650	53.30747	base	massive
AOK119	-168.12650	53.30747	top	massive
AOK124	-168.08158	53.55703	base	massive
AOK131	-168.08158	53.55703	top	massive
AOK137	-167.98958	53.44905	top	massive
AOK138	-167.98958	53.44905	base	massive
AOK141	-167.75318	53.35493	top	stratified
AOK142	-167.75318	53.35493	base	stratified
AOK143	-167.82008	53.30075	base	stratified
AOK144	-167.82008	53.30075	top	stratified
AOK145	-167.76942	53.31833	bulk	stratified
AOK146	-167.69947	53.31795	base	stratified
AOK147	-167.69947	53.31795	top	stratified
AOK149	-167.57803	53.34178	bulk	stratified
AOK150	-167.49803	53.41980	bulk	stratified
AOK151	-167.60863	53.29932	bulk	stratified
AOK153	-167.47988	53.31973	bulk	stratified
AOK154	-167.40687	53.39245	bulk	stratified
AOK163	-168.14517	53.53970	base	massive
AOK164	-168.38345	53.38918	top	massive
AOK165	-168.29128	53.47560	base	massive
AOK166	-168.29128	53.47560	top	massive
AOK167	-168.25500	53.28255	base	massive
AOK169	-168.26645	53.29192	bulk	stratified
AOK170	-168.27703	53.27163	bulk	stratified
AOK171	-168.30105	53.27005	bulk	massive
AOK175	-168.34233	53.20257	bulk	stratified
AOK177	-168.33835	53.23583	bulk	stratified
AOK187	-167.67463	53.37493	base	sandy deposit
AOK188	-167.67463	53.37493	top	sandy deposit
AOK189	-167.67463	53.37493	bulk	stratified

Table 3.A2: Grain size distributions of pyroclastic deposit samples given in cumulative weight percent. Grain sizes are given in φ units (-log$_2$(mm)). Before calculating the cumulative wt.%, the wt.% of each size were normalized to 100 wt.% by using the sample total weight (entry *total wt.*, sizes ≥*field*), the sample laboratory weight (entry *wt. lab.*, sizes <*field*), and the fines weight fraction (<*4 φ*). To obtain the actual weight of material at −2 φ, for example, calculate the difference in normalized wt.% between −2.5 and −2 φ and multiply the result by the total weight of the sample. An empty space means 0 wt.% and n.a. is "not analyzed".

φ	AOK 33	AOK 34	AOK 42	AOK 46	AOK 47	AOK 49	AOK 50	AOK 62	AOK 63	AOK 64	AOK 69	AOK 70
-5.5	n.a.	n.a.		n.a.								
-5.0	2.0	4.7		2.2				3.4				
-4.5	n.a.	n.a.	n.a.	n.a.	6.8	2.0		4.9	5.9			
-4.0	14.5	15.4	6.1	6.9	11.0	9.5	3.8	7.0	13.3	13.3		
-3.5	n.a.	n.a.	n.a.	11.8	14.8	16.0	7.4	8.2	18.1	16.7		
-3.0	33.2	30.8	17.8	16.9	21.3	20.2	13.3	11.0	25.5	21.8		
-2.5	n.a.	n.a.	n.a.	22.4	27.0	24.9	20.0	14.7	33.3	29.1		
-2.0	55.7	49.0	37.4	28.4	34.6	29.5	27.7	20.8	42.0	36.4	0.7	0.7
-1.5	62.3	57.3	46.8	35.8	41.6	38.3	35.5	26.9	52.0	46.9	2.0	3.8
-1.0	67.0	64.2	55.3	42.9	49.0	46.8	44.2	34.6	61.4	57.8	3.7	15.2
-0.5	71.5	69.9	62.2	50.0	56.2	53.7	53.3	41.9	70.6	68.7	6.4	41.5
0.0	74.5	74.9	68.2	56.0	61.4	60.0	60.9	48.8	77.9	77.4	9.8	67.4
0.5	78.1	79.7	73.9	62.0	67.2	65.9	67.8	55.7	84.0	84.4	15.0	83.9
1.0	81.7	84.2	78.8	67.9	72.1	71.2	73.9	62.3	88.9	90.1	22.6	92.6
1.5	84.9	88.0	83.7	73.1	75.7	76.4	78.7	68.9	92.5	94.4	35.1	96.5
2.0	88.3	90.8	87.2	77.0	79.2	80.6	82.5	74.7	94.9	97.1	49.8	98.2
2.5	91.5	93.1	90.2	81.7	82.3	84.4	85.7	79.9	96.4	98.5	65.0	98.8
3.0	94.5	95.1	93.1	85.2	85.6	88.2	88.8	84.7	97.3	99.3	77.7	99.2
3.5	96.7	96.4	95.5	87.9	88.4	91.6	91.6	88.7	97.6	99.6	87.2	99.4
4.0	98.3	97.5	97.3	91.0	91.6	94.5	93.6	92.6	97.8	99.7	93.0	99.6
4.5	99.1	98.8	98.8	95.5	95.2	96.4	95.8	95.2	98.1	99.9	96.5	99.8
5.0	99.2	99.0	99.3	96.1	98.1	97.6	97.3	95.8	98.6	99.9	97.7	99.9
5.5	99.5	99.4	99.5	98.0	99.7	98.9	98.7	97.3	99.2	100.0	99.4	99.9
6.0	99.6	99.5	99.7	98.9	100.0	99.4	99.3	98.2	99.6	100.0	99.7	100.0
6.5	99.8	99.8	99.9	99.8	100.0	99.9	99.9	99.3	99.9	100.0	99.9	100.0
7.0	100.0	100.0	100.0	100.0	100.0	100.0	100.0	100.0	100.0	100.0	100.0	100.0
M$_d$[a]	-2.3	-2.0	-1.3	-0.5	-0.9	-0.8	-0.7	0.1	-1.6	-1.4	2.0	-0.3
σ[a]	2.5	2.5	2.3	3.1	3.1	3.0	2.5	2.7	2.1	2.1	1.5	0.8
<4 φ[b]	14.327	20.283	16.163	123.762	39.981	30.928	30.974	29.084	15.555	1.678	15.402	0.871
total wt.[c]	2721	3735	2147	1382	926	560	819	776	701	662	219	241
field[d]	-2.0	-2.0	-2.0		-2.5		-2.5	-2.5				
wt. lab.[e]	380.307	407.278	371.999		345.962		387.344	336.896				
wt. left[f]	1205	1905	1345		676		655	662				

[a] median size (φ) at ±0.1 φ and sorting parameter (σ).

[b] weight of fines <4 φ, the size distribution of which was determined with the particle counter.

[c] total sample weight at ±0.5 g.

[d] size above which sieving was done in the field (φ).

[e] weight of sample sieved in laboratory (sizes below the value of *field*) at ±0.001 g.

[f] weight of sample left in the field (sizes ≥*field*) at ±0.5 g.

Table 3.A2 continued

φ	AOK 84	AOK 86	AOK 91	AOK 92	AOK 93	AOK 94	AOK 96	AOK 97	AOK 98	AOK 99	AOK 100	AOK 101
-7.0											35.4	
-6.5										n.a.	55.2	
-6.0										6.9	69.3	
-5.5				n.a.	n.a.		n.a.	n.a.	n.a.	n.a.	72.5	n.a.
-5.0				8.3	4.8		3.5	2.2	16.4	13.4	75.1	4.9
-4.5	n.a.	n.a.	n.a.	n.a.	n.a.	n.a.	n.a.	n.a.	n.a.	n.a.	n.a.	n.a.
-4.0	1.2	17.9	4.0	10.8	12.7	2.8	18.7	5.5	20.6	19.3	77.4	14.8
-3.5	n.a.	n.a.	n.a.	n.a.	n.a.	n.a.	n.a.	n.a.	n.a.	n.a.	78.2	19.8
-3.0	20.0	62.1	12.9	16.5	24.0	8.5	53.5	15.9	34.5	30.2	79.1	26.9
-2.5	n.a.	n.a.	n.a.	n.a.	n.a.	n.a.	n.a.	n.a.	n.a.	n.a.	80.0	35.0
-2.0	58.0	89.0	28.1	29.1	37.6	24.1	81.8	30.7	49.9	44.3	80.9	45.2
-1.5	73.6	94.8	40.5	37.6	45.1	30.6	87.5	37.6	56.5	51.3	82.0	56.0
-1.0	83.9	96.9	48.2	45.9	51.2	38.2	91.1	45.0	62.2	57.8	83.2	66.2
-0.5	91.2	98.2	54.9	52.8	56.4	45.5	93.8	52.1	67.7	64.7	84.4	75.7
0.0	95.3	98.8	60.8	58.2	60.9	51.6	95.4	58.3	72.6	69.9	85.5	81.9
0.5	97.4	99.1	66.4	64.0	65.0	58.6	96.6	64.2	76.9	75.3	86.7	86.6
1.0	98.3	99.2	72.0	68.4	69.1	64.2	97.3	69.6	80.8	78.9	88.0	90.2
1.5	98.8	99.3	76.9	72.1	72.6	69.0	97.7	74.3	83.9	82.3	89.2	93.0
2.0	99.0	99.4	81.3	75.4	76.0	73.8	98.0	78.3	86.4	85.2	90.7	94.3
2.5	99.1	99.5	85.0	77.9	79.2	77.7	98.3	81.7	88.3	87.5	92.2	96.2
3.0	99.3	99.5	89.1	80.4	83.3	82.0	98.7	85.5	90.4	89.7	94.1	97.3
3.5	99.3	99.6	92.5	82.5	86.8	85.7	99.0	88.6	92.0	91.8	95.6	98.0
4.0	99.4	99.7	95.9	84.5	90.3	89.7	99.2	91.6	93.9	93.8	97.2	98.6
4.5	99.9	99.9	96.7	91.2	91.3	94.3	99.5	92.8	94.7	95.8	98.1	99.3
5.0	99.9	100.0	97.2	93.8	93.5	96.5	99.7	94.5	95.2	97.2	98.8	99.5
5.5	99.9	100.0	98.8	97.6	96.7	98.2	99.8	96.9	96.5	97.8	99.6	99.8
6.0	100.0	100.0	99.7	99.1	98.3	99.1	99.9	98.6	97.7	98.4	99.9	99.9
6.5	100.0	100.0	100.0	99.9	99.3	99.8	100.0	99.9	99.7	99.3	100.0	100.0
7.0	100.0	100.0	100.0	100.0	100.0	100.0	100.0	100.0	100.0	100.0	100.0	100.0
M_d	-2.2	-3.3	-1.1	-0.7	-1.1	-0.1	-3.1	-0.7	-2.0	-1.6	-6.6	-1.8
σ	1.1	1.0	2.5	3.4	3.4	2.9	1.2	2.9	3.3	3.2	3.2	2.1
<4 φ	3.848	4.830	21.028	54.946	43.067	41.149	8.040	37.371	31.845	27.704	183.669	25.907
total wt.	1906	1890	821	3394	2277	2715	2010	3487	3400	3124	6656	1823
field	-2.0	-2.0	-2.0	-2.0	-2.0	-2.0	-2.0	-2.0	-2.0	-2.0		
wt. lab	289.249	170.541	371.428	251.248	277.756	302.866	186.644	308.832	260.691	249.281		
wt. left	800	207	590	2405	1420	2060	365	2415	1705	1740		

Table 3.A2 continued

φ	AOK 102	AOK 103	AOK 104	AOK 105	AOK 106	AOK 107	AOK 108	AOK 109	AOK 110	AOK 111	AOK 112	AOK 113
-6.5				n.a.	n.a.							
-6.0				5.7	11.9							
-5.5	n.a.	n.a.	n.a.	n.a.	n.a.	n.a.	n.a.					
-5.0	2.3	9.6	4.9	12.3	29.8	1.7	2.1					
-4.5	n.a.	n.a.	n.a.	n.a.	n.a.	n.a.	n.a.				n.a.	
-4.0	8.9	15.9	8.7	17.7	38.5	4.3	4.9				3.2	
-3.5	n.a.	n.a.	n.a.	n.a.	n.a.	n.a.	n.a.	1.4	2.2	4.4	n.a.	
-3.0	18.4	24.3	18.5	29.3	45.5	13.5	13.2	13.8	3.8	13.7	14.9	1.1
-2.5	n.a.	n.a.	n.a.	n.a.	n.a.	n.a.	n.a.	26.1	7.8	24.9	n.a.	2.4
-2.0	32.1	36.5	32.4	44.3	59.5	28.0	25.3	34.7	11.2	33.8	32.1	5.7
-1.5	40.1	42.0	38.7	52.7	64.8	33.9	32.6	42.5	18.5	42.8	38.7	11.5
-1.0	47.3	48.2	44.9	59.3	70.3	40.7	39.0	51.1	26.9	50.2	46.1	18.9
-0.5	54.5	54.5	51.7	65.4	74.9	47.7	45.7	59.1	35.1	56.7	53.2	27.2
0.0	59.9	59.4	57.4	70.2	78.4	54.2	51.5	66.0	41.6	62.1	59.0	35.5
0.5	65.3	64.4	63.0	74.6	81.6	60.7	56.9	72.3	48.2	67.0	64.4	44.2
1.0	70.1	69.1	68.4	78.6	84.3	66.8	62.1	77.6	54.7	71.3	69.5	52.5
1.5	74.0	73.0	73.0	81.8	86.5	72.4	66.8	81.9	60.7	75.5	74.2	60.0
2.0	77.6	76.7	77.0	84.5	88.3	77.2	71.0	85.6	66.4	79.3	78.4	67.0
2.5	80.5	79.7	80.4	86.7	89.9	81.2	74.8	88.9	71.8	83.4	82.4	73.4
3.0	83.6	82.9	84.6	89.1	91.6	85.1	79.6	92.4	78.4	87.3	87.0	80.6
3.5	86.6	86.1	87.3	90.9	93.1	88.8	84.0	95.1	84.5	91.1	91.1	86.3
4.0	89.6	89.1	90.6	93.0	94.7	91.9	88.3	97.3	87.0	94.0	94.0	91.5
4.5	95.0	94.2	93.6	94.0	97.3	95.5	93.2	98.3	89.8	96.5	97.1	96.5
5.0	96.6	95.1	94.3	95.5	97.6	97.0	94.6	99.2	92.4	97.7	98.9	98.2
5.5	98.5	97.0	97.2	97.8	98.4	98.4	96.7	99.7	96.3	99.0	99.8	99.3
6.0	99.1	97.9	98.7	99.0	99.0	99.2	97.2	99.9	98.4	99.5	100.0	99.7
6.5	99.7	99.3	99.9	99.9	99.8	99.7	98.9	100.0	99.8	99.9	100.0	99.9
7.0	100.0	100.0	100.0	100.0	100.0	100.0	100.0	100.0	100.0	100.0	100.0	100.0
M_d	-0.8	-0.8	-0.6	-1.7	-2.6	-0.3	-0.1	-1.0	0.6	-1.0	-0.7	0.8
σ	3.2	3.6	3.2	3.1	3.4	2.8	3.2	2.4	2.6	2.8	2.8	2.3
<4 φ	42.868	47.839	69.473	26.758	47.703	69.698	49.253	3.790	12.064	52.182	20.984	7.865
total wt.	3018	3235	3906	3953	2940	4273	3460	140	93	872	1370	92
field	-2.0	-2.0	-2.0	-2.0	-2.0	-2.0	-2.0				-2.0	
wt. lab	280.469	279.300	499.368	212.242	363.746	620.583	314.844				237.556	
wt. left	2050	2055	2640	2200	1192	3075	2585				930	

Table 3.A2 continued

φ	AOK 114	AOK 115	AOK 116	AOK 117	AOK 118	AOK 119	AOK 124	AOK 131	AOK 137	AOK 138	AOK 141	AOK 142
-5.5					n.a.	n.a.	n.a.			n.a.		
-5.0					9.6	2.3	5.0			12.1		
-4.5			n.a.		n.a.	n.a.	n.a.	n.a.		n.a.		
-4.0			1.7	8.2	15.7	10.0	18.4	1.2	1.3	19.4	1.1	1.2
-3.5	1.9	0.1	n.a.	14.8	n.a.	n.a.	n.a.	n.a.	2.6	26.2	3.9	8.1
-3.0	6.7	0.2	6.0	21.6	27.0	23.4	29.2	7.9	7.7	32.8	14.4	18.6
-2.5	14.0	0.6	n.a.	29.9	n.a.	n.a.	n.a.	n.a.	16.4	40.9	32.7	36.9
-2.0	20.2	1.2	21.6	37.8	41.4	42.8	45.4	19.8	25.2	48.5	50.8	54.7
-1.5	29.9	2.6	27.6	47.8	49.9	48.9	53.7	27.9	35.3	57.8	70.8	72.5
-1.0	40.3	6.0	36.1	58.0	57.1	55.8	61.8	37.3	45.7	66.9	86.0	85.9
-0.5	51.1	13.0	44.9	68.2	63.9	62.7	69.8	45.1	54.5	74.3	94.3	93.8
0.0	60.3	21.3	52.9	76.5	69.1	68.3	75.7	52.4	64.1	79.4	97.2	96.2
0.5	68.9	30.1	60.0	83.8	73.8	73.2	81.8	59.2	73.1	84.5	98.2	97.2
1.0	76.1	38.9	66.5	89.9	77.9	77.7	86.7	65.2	80.7	88.4	98.6	97.6
1.5	81.9	47.3	72.1	94.0	81.3	81.3	90.0	70.5	87.1	91.0	98.8	97.8
2.0	86.7	55.2	76.5	96.5	84.0	84.3	92.7	75.4	91.3	93.1	98.9	98.1
2.5	90.4	63.1	80.2	98.0	86.2	86.8	94.6	79.8	94.7	94.8	99.2	98.4
3.0	94.0	73.7	84.0	98.8	88.5	89.5	96.2	84.1	97.1	96.2	99.4	98.8
3.5	96.3	82.6	87.1	99.1	90.4	91.8	97.3	88.4	98.5	97.1	99.6	99.1
4.0	97.7	89.6	90.1	99.2	92.5	94.2	98.1	91.7	99.2	97.9	99.8	99.3
4.5	99.3	94.9	93.6	99.5	93.7	96.8	98.6	96.0	99.7	98.4	99.9	99.7
5.0	99.6	97.6	95.6	99.7	95.4	98.1	99.1	96.9	99.8	98.9	99.9	99.7
5.5	99.9	99.6	98.7	99.9	99.4	99.5	99.6	98.2	99.9	99.2	100.0	99.8
6.0	100.0	99.9	99.7	100.0	99.9	99.9	99.8	99.1	100.0	99.5	100.0	99.9
6.5	100.0	100.0	100.0	100.0	100.0	100.0	99.9	99.7	100.0	99.8	100.0	100.0
7.0	100.0	100.0	100.0	100.0	100.0	100.0	100.0	100.0	100.0	100.0	100.0	100.0
M_d	-0.6	1.6	-0.2	-1.4	-1.5	-1.4	-1.8	-0.2	-0.8	-1.9	-2.1	-2.1
σ	2.1	2.0	2.7	2.0	3.0	2.8	2.5	2.7	1.9	2.3	1.1	1.1
<4 φ	7.927	59.229	36.980	5.869	35.820	20.884	13.278	31.903	4.293	18.320	0.904	3.985
total wt.	339	569	1809	770	3829	2012	2284	2781	2350	3435	1426	556
field			-2.0		-2.0	-2.0	-2.0	-2.0	-2.5	-2.5	-2.5	
wt. lab			292.171		278.636	206.602	373.916	309.921	468.637	513.905	244.465	
wt. left			1418		2245	1150	1246	2230	1965	2030	960	

Table 3.A2 continued

φ	AOK 143	AOK 144	AOK 145	AOK 146	AOK 147	AOK 149	AOK 150	AOK 151	AOK 153	AOK 154	AOK 163	AOK 164
-5.5											n.a.	
-5.0											12.4	
-4.5											n.a.	
-4.0	0.4			0.7							23.4	
-3.5	2.7	0.8		1.2							30.6	0.4
-3.0	11.1	3.6	4.2	3.4	1.3			0.5			39.8	1.7
-2.5	23.9	10.1	8.7	9.3	3.1	2.0	3.4	1.9	0.8		49.3	4.9
-2.0	39.1	19.6	18.3	22.4	5.5	7.5	8.3	8.4	3.5	0.4	56.3	7.7
-1.5	57.1	34.3	33.3	42.8	9.8	22.8	15.7	25.6	8.5	2.3	64.9	13.7
-1.0	73.5	47.7	49.3	67.0	16.9	48.5	33.9	50.2	23.7	7.0	73.2	21.4
-0.5	84.7	59.1	63.0	85.0	27.4	73.0	60.3	74.6	48.8	15.3	80.4	28.9
0.0	90.4	66.6	70.9	92.8	42.1	89.0	78.8	87.8	72.9	28.7	85.0	36.1
0.5	94.2	73.6	77.2	96.7	61.6	95.4	88.1	95.0	88.4	46.9	89.1	42.7
1.0	95.9	78.6	81.1	98.1	78.1	97.8	91.4	97.7	94.8	67.0	92.2	50.0
1.5	96.6	82.4	83.3	98.5	89.9	98.2	92.2	98.3	97.0	83.7	94.2	57.0
2.0	97.1	85.9	86.0	98.8	94.8	98.4	93.1	98.5	97.4	91.5	95.7	63.6
2.5	97.5	88.9	89.0	99.0	96.7	98.7	94.3	98.8	97.8	95.3	96.6	71.4
3.0	97.9	92.0	92.4	99.2	97.7	98.9	96.1	99.1	98.4	97.4	97.5	79.5
3.5	98.3	94.8	95.1	99.4	98.5	99.1	97.9	99.3	99.0	98.6	98.1	87.2
4.0	98.6	97.0	96.8	99.6	99.0	99.3	99.6	99.6	99.4	99.3	98.6	94.2
4.5	99.3	98.5	97.7	99.8	99.3	99.7	99.8	99.8	99.7	99.6	99.0	95.8
5.0	99.7	98.8	98.6	99.9	99.6	99.8	99.9	99.9	99.8	99.8	99.2	96.8
5.5	99.9	99.3	99.3	100.0	99.9	99.9	100.0	100.0	100.0	99.9	99.6	98.5
6.0	100.0	99.5	99.6	100.0	99.9	100.0	100.0	100.0	100.0	99.9	99.8	99.3
6.5	100.0	99.8	99.9	100.0	100.0	100.0	100.0	100.0	100.0	100.0	99.9	100.0
7.0	100.0	100.0	100.0	100.0	100.0	100.0	100.0	100.0	100.0	100.0	100.0	100.0
M_d	-1.7	-0.9	-1.0	-1.4	0.2	-1.0	-0.7	-1.0	-0.5	0.6	-2.4	1.0
σ	1.2	2.0	1.9	0.9	1.2	0.8	0.9	0.8	0.8	1.0	2.3	2.4
<4 φ	8.074	12.323	1.637	1.425	3.155	1.809	0.164	1.118	0.198	0.172	10.373	19.025
total wt.	561	1925	51	317	307	253	41	257	35	26	2504	1294
field		-2.5									-2.5	-2.5
wt. lab		364.199									384.098	309.856
wt. left		1730									1270	1230

Table 3.A2 continued

φ	AOK 165	AOK 166	AOK 167	AOK 169	AOK 170	AOK 171	AOK 175	AOK 177	AOK 187	AOK 188	AOK 189
-5.5	n.a.	n.a.									
-5.0	6.2	8.8									
-4.5	n.a.	n.a.									
-4.0	22.3	12.9	4.2	1.6		1.8					
-3.5	31.2	16.7	7.7	5.6	2.4	3.2					3.4
-3.0	40.3	20.6	11.6	14.5	10.3	7.3		4.3			10.8
-2.5	49.4	26.4	17.4	26.5	21.1	14.1		10.5		0.5	22.1
-2.0	52.5	34.1	24.6	38.4	32.1	18.5		17.7		3.4	37.4
-1.5	63.2	39.7	31.7	51.7	45.5	24.9		29.0	0.5	11.0	60.2
-1.0	72.2	46.4	39.3	66.2	57.9	31.3		43.2	3.6	24.0	81.2
-0.5	79.7	52.5	47.2	78.1	69.5	37.5		57.7	12.5	38.1	93.3
0.0	85.0	57.8	53.4	87.3	77.5	43.5	1.1	70.6	27.2	48.4	97.1
0.5	89.9	62.6	60.2	93.0	84.5	49.7	3.2	80.1	51.7	61.8	98.5
1.0	93.7	67.0	66.8	96.1	89.4	56.1	11.4	86.4	77.0	77.2	99.0
1.5	96.0	71.1	72.1	97.8	92.6	62.2	22.3	89.9	88.0	87.0	99.3
2.0	97.6	74.9	77.3	98.6	95.2	67.9	31.5	92.1	92.9	92.7	99.5
2.5	98.5	78.7	82.0	99.0	96.9	73.3	41.5	94.2	96.6	96.2	99.7
3.0	99.1	83.2	86.7	99.3	98.3	79.3	53.7	96.3	98.2	97.8	99.9
3.5	99.4	87.6	90.4	99.4	99.0	84.4	67.5	97.7	98.7	98.4	99.9
4.0	99.6	92.9	93.9	99.6	99.4	89.8	81.3	98.8	99.0	98.8	100.0
4.5	99.8	95.6	95.8	99.7	99.4	91.8	87.6	99.5	99.3	99.2	100.0
5.0	99.8	97.5	96.7	99.8	99.5	94.1	90.8	99.8	99.4	99.4	100.0
5.5	99.9	99.6	98.4	99.9	99.7	97.6	95.2	100.0	99.7	99.8	100.0
6.0	100.0	100.0	99.2	99.9	99.8	99.6	96.7	100.0	99.8	99.9	100.0
6.5	100.0	100.0	100.0	100.0	99.9	100.0	98.8	100.0	100.0	100.0	100.0
7.0	100.0	100.0	100.0	100.0	100.0	100.0	100.0	100.0	100.0	100.0	100.0
M_d	-2.4	-0.7	-0.2	-1.6	-1.3	0.5	2.8	-0.8	0.5	0.1	-1.8
σ	2.2	3.6	2.7	1.4	1.6	2.9	1.5	1.5	0.9	1.3	1.0
<4 φ	3.130	27.841	21.802	2.374	1.784	36.912	0.360	2.176	1.036	1.568	0.010
total wt.	2195	2052	1895	581	281	1106	2	175	107	131	96
field	-2.5	-2.5	-2.5			-2.5					
wt. lab	366.759	290.542	294.637			310.852					
wt. left	1110	1510	1565			950					

Table 3.A3: Componentry (%) of pyroclastic deposit samples. Sample locations are shown on Fig. 3.1. Grain size is in ϕ unit ($-\log_2(\text{mm})$). The clast contents are normalized to 100% and were obtained by weighing ($>0\ \phi$) or counting ($\leq 0\ \phi$) a representative quantity of clasts for each size. For example, to obtain the actual weight of scoria of a given size, multiply the content given in this table by the actual weight percent for that size calculated from Table 3.A2. An empty space means 0 wt.% and n.a. is "not analyzed".

ϕ	AOK34 Scoria	Lithic	Glass	Crystal	AOK42 Scoria	Lithic	Glass	Crystal	AOK46 Scoria	Lithic	Glass	Crystal
-5.0	100.0				n.a.	n.a.	n.a.	n.a.	100.0			
-4.0	84.1	15.9			34.1	65.9			62.7	37.3		
-3.5	n.a.	n.a.	n.a.	n.a.	n.a.	n.a.	n.a.	n.a.	64.9	35.1		
-3.0	88.7	11.3			68.0	32.0			57.8	42.2		
-2.5	n.a.	n.a.	n.a.	n.a.	n.a.	n.a.	n.a.	n.a.	59.9	40.1		
-2.0	80.0	20.0			70.0	30.0			66.1	33.9		
-1.5	91.7	7.9	0.4		90.2	8.9	0.9		75.7	24.3		
-1.0	90.2	9.8			77.0	22.3	0.7		71.3	28.7		
-0.5	93.9	6.1			84.3	15.7			73.0	27.0		
0.0	75.2	22.8	1.7	0.3	45.6 (2)	46.0	7.3	1.1	37.7	53.8	8.5	
1.0	73.9 (7)[a]	15.8	3.8	6.5	47.4 (2)	35.8	13.7	3.1	44.6 (3)	39.3	14.2	1.9
2.0	75 (14)	7.0	4.4	13.6	37 (5)	13.1	30.3	19.6	43.1 (3)	20.2	25.6	11.1

[a]Number in parenthesis is the fraction (%) of oxidized scoria: e.g., 73.9 (7) means that the total scoria content for that grain size is 73.9 wt.%, but 7% of the 73.9 wt.% is older, oxidized scoria.

ϕ	AOK62 Scoria	Lithic	Glass	Crystal	AOK63 Scoria	Lithic	Glass	Crystal	AOK64 Scoria	Lithic	Glass	Crystal
-5.0	100.0				n.a.	n.a.	n.a.	n.a.	n.a.	n.a.	n.a.	n.a.
-4.5	100.0					100.0			n.a.	n.a.	n.a.	n.a.
-4.0	62.5	37.5			5.4	94.6			12.7	87.3		
-3.5	60.0	40.0			24.5	75.5			37.5	62.5		
-3.0	71.4	28.6			37.0	63.0			6.8	93.2		
-2.5	89.7	10.3			48.9	51.1			7.0	93.0		
-2.0	78.4	20.0	1.6		49.5	49.5	1.0		13.6	85.5	0.9	
-1.5	75.0	23.6	1.4		60.7	39.3			20.6	78.8	0.6	
-1.0	76.0	22.7	1.3		57.9	41.2	0.9		47.3	51.8	0.9	
-0.5	78.2	20.1	1.7		71.1	26.7	2.2		67.7	31.6	0.7	
0.0	44.6 (1)	47.6	7.5	0.3	39.3 (2)	55.8	3.8	1.1	56.7 (1)	37.1	5.6	0.6
1.0	39.3 (4)	44.9	13.2	2.6	44 (3)	39.9	10.8	5.3	55.1 (3)	22.1	12.5	10.3
2.0	47.2 (4)	15.6	29.8	7.4	55.3 (4)	14.8	13.6	16.3	59.2 (2)	8.2	16.4	16.2

Table 3.A3 continued

φ	AOK69 Scoria	Lithic	Glass	Crystal	AOK70 Scoria	Lithic	Glass	Crystal	AOK84 Scoria	Lithic	Glass	Crystal
-4.0	n.a.	n.a.	n.a.	n.a.	n.a.	n.a.	n.a.	n.a.	78.3	21.7		
-3.0	n.a.	n.a.	n.a.	n.a.	n.a.	n.a.	n.a.	n.a.	35.0	32.0	33.0	
-2.0	93.9	6.1			100.0				19.0	40.0	41.0	
-1.5	79.6	19.2	1.2		93.9	6.1			n.a.	n.a.	n.a.	n.a.
-1.0	76.6	21.9	1.5		82.6	17.4			44.7	27.2	28.1	
-0.5	82.1	17.2	0.7		82.5	17.5			n.a.	n.a.	n.a.	n.a.
0.0	70.6 (2)	27.1	2.3		77.8	19.6	1.9	0.7	46.0	26.4	27.6	
1.0	66.5 (2)	20.9	8.5	4.1	83.6	10.1	4.8	1.5	19.6	24.8	53.5	2.1
2.0	48.9 (3)	21.6	19.7	9.8	78.3	7.4	8.3	6.0	n.a.	n.a.	n.a.	n.a.

φ	AOK86 Scoria	Lithic	Glass	Crystal	AOK93 Scoria	Lithic	Glass	Crystal	AOK94 Scoria	Lithic	Glass	Crystal
-5.0	n.a.	n.a.	n.a.	n.a.	100.0				n.a.	n.a.	n.a.	n.a.
-4.0	98.6	1.4			100.0				10.7	89.3		
-3.0	97.3	2.7			86.4	13.6			56.1	43.9		
-2.0	94.6	5.4			76.4	23.6			87.2	12.8		
-1.5	n.a.	n.a.	n.a.	n.a.	80.7	18.4	0.9		55.2	42.3	2.5	
-1.0	82.4	12.0	5.6		80.6	18.6	0.8		66.4	29.6	3.9	0.1
-0.5	n.a.	n.a.	n.a.	n.a.	88.7	11.3			74.9	22.4	2.7	
0.0	66.5	26.9	6.3	0.3	71.5	27.3	1.2		74.4	18.6	6.9	0.1
1.0	n.a.	n.a.	n.a.	n.a.	66.9	24.9	6.2	2.0	47.8	30.2	19.6	2.4
2.0	n.a.	n.a.	n.a.	n.a.	63.4	14.5	9.6	12.5	55.3 (4)	15.6	20.9	8.2
3.0	n.a.	n.a.	n.a.	n.a.	64.3	8.6	15.4	11.7	55.3 (2)	13.6	18.0	13.1
4.0	n.a.	n.a.	n.a.	n.a.	50.9	3.9	32.8	12.4	45.3 (4)	8.0	27.9	18.8

φ	AOK96 Scoria	Lithic	Glass	Crystal	AOK97 Scoria	Lithic	Glass	Crystal	AOK98 Scoria	Lithic	Glass	Crystal
-6.0	n.a.	n.a.	n.a.	n.a.	n.a.	n.a.	n.a.	n.a.	100.0			
-5.0	100.0				100.0				44.6	55.4		
-4.0	100.0				100.0				39.6	60.4		
-3.0	94.6	5.4			93.4	6.6			73.5	26.5		
-2.0	89.6	10.4			94.6	5.4			67.1	32.9		
-1.5	n.a.	n.a.	n.a.	n.a.	65.1	33.1	1.8		57.9	41.8	0.3	
-1.0	84.2	10.6	5.1	0.1	75.6	23.7	0.7		68.0	32.0		
-0.5	n.a.	n.a.	n.a.	n.a.	71.5	26.8	1.7		76.3	23.2	0.5	
0.0	72.4 (1)	17.3	10.0	0.3	80.7	17.4	1.4	0.5	72.9	26.5	0.6	
1.0	51 (1)	23.3	23.3	2.4	56.5	35.3	4.8	3.4	48.3	46.0	1.5	4.2
2.0	n.a.	n.a.	n.a.	n.a.	55.7	33.2	2.9	8.2	44.3	31.6	10.3	13.8
3.0	n.a.	n.a.	n.a.	n.a.	49.1	31.1	6.3	13.5	39.3	29.6	14.6	16.5
4.0	n.a.	n.a.	n.a.	n.a.	41.0	24.5	14.7	19.8	52.2	21.4	14.1	12.3

Table 3.A3 continued

φ	AOK99 Scoria	Lithic	Glass	Crystal	AOK100 Scoria	Lithic	Glass	Crystal	AOK101 Scoria	Lithic	Glass	Crystal
-7.0	n.a.	n.a.	n.a.	n.a.	100.0				n.a.	n.a.	n.a.	n.a.
-6.5	n.a.	n.a.	n.a.	n.a.	100.0				n.a.	n.a.	n.a.	n.a.
-6.0	n.a.	n.a.	n.a.	n.a.	100.0				n.a.	n.a.	n.a.	n.a.
-5.5	n.a.	n.a.	n.a.	n.a.	100.0				n.a.	n.a.	n.a.	n.a.
-5.0	100.0				100.0				24.6	75.4		
-4.0	78.4	21.6			47.9	52.1			35.5	64.5		
-3.5	n.a.	n.a.	n.a.	n.a.	85.0	15.0			75.7	24.3		
-3.0	71.5	28.5			77.7	22.3			65.8 (4)	34.2		
-2.5	n.a.	n.a.	n.a.	n.a.	81.4	18.1		0.5	70.9	29.1		
-2.0	92.0	8.0			78.8	21.2			70 (1)	30.0		
-1.5	69.8	30.1	0.1		79.5	20.3		0.2	82.3 (2)	17.2	0.5	
-1.0	75.9	24.0	0.1		90.3	9.7			78.2	21.6	0.2	
-0.5	71.0	28.2	0.8		78.6	20.8	0.6		82.1 (1)	17.2	0.7	
0.0	76.7	22.3	1.0		84.6	15.2	0.2		85 (1)	13.5	1.2	0.3
0.5	53.8	38.4	6.4	1.4	86.4	7.9	5.7		71.8 (1)	23.0	4.2	1.0
1.0	55.0	34.8	7.3	2.9	59.8	34.9	3.5	1.8	51 (1)	30.5	10.4	8.1
1.5	44.9	41.7	7.6	5.8	70.5	15.0	12.2	2.3	60.4 (1)	22.0	12.7	4.9
2.0	50.5	33.0	8.4	8.1	69.6	15.9	8.2	6.3	39 (3)	27.6	18.4	15.0
2.5	45.3	33.1	10.5	11.1	66.9 (1)	12.2	11.0	9.9	63.3 (2)	10.9	17.5	8.3
3.0	46.1	31.0	11.4	11.5	71.5	9.5	12.9	6.1	50.2 (1)	20.4	14.6	14.8
3.5	47.0	22.3	15.1	15.6	56.6	4.9	23.7	14.8	46.6 (3)	9.7	24.2	19.5
4.0	41.7	15.5	24.7	18.1	46.5 (1)	4.5	25.9	23.1	55.4	12.9	16.4	15.3

φ	AOK103 Scoria	Lithic	Glass	Crystal	AOK104 Scoria	Lithic	Glass	Crystal	AOK105 Scoria	Lithic	Glass	Crystal
-6.0	n.a.	n.a.	n.a.	n.a.	n.a.	n.a.	n.a.	n.a.	100.0			
-5.0	65.0	35.0			100.0				68.5	31.5		
-4.0	75.9	24.1			100.0				76.3	23.7		
-3.0	81.0	19.0			81.8	18.2			79.5	20.5		
-2.0	90.0	10.0			80.5	19.5			87.2	12.8		
-1.5	60.6	38.0	1.4		68.5	30.9	0.6		58.1	40.1	1.8	
-1.0	54.6	41.7	3.7		68.7	31.3			72.2	27.7	0.1	
-0.5	58.3	38.3	3.4		72.3	26.9	0.8		70.8	29.0	0.2	
0.0	45.5	48.3	5.9	0.3	77.6	22.4			76.3	23.1	0.5	0.1
0.5	n.a.	n.a.	n.a.	n.a.	59.2	38.5	2.3		n.a.	n.a.	n.a.	n.a.
1.0	51.6 (1)	37.8	9.2	1.4	70.1 (1)	27.5	1.0	1.4	62.9	30.4	2.7	4.0
1.5	n.a.	n.a.	n.a.	n.a.	64.6 (2)	23.5	9.7	2.2	n.a.	n.a.	n.a.	n.a.
2.0	61 (8)	23.4	8.0	7.6	63.2 (7)	27.1	2.4	7.3	61.1	17.9	3.0	18.0
2.5	n.a.	n.a.	n.a.	n.a.	61.9 (8)	17.1	13.2	7.8	n.a.	n.a.	n.a.	n.a.
3.0	n.a.	n.a.	n.a.	n.a.	62.1 (12)	18.3	7.8	11.8	56.3	13.6	9.9	20.2
3.5	n.a.	n.a.	n.a.	n.a.	51.5 (18)	9.5	21.2	17.8	n.a.	n.a.	n.a.	n.a.
4.0	n.a.	n.a.	n.a.	n.a.	40.2 (19)	11.9	29.2	18.7	57.6	14.6	15.5	12.3

Table 3.A3 continued

φ	AOK108 Scoria	Lithic	Glass	Crystal	AOK109 Scoria	Lithic	Glass	Crystal	AOK110 Scoria	Lithic	Glass	Crystal
-5.0	100.0				n.a.	n.a.	n.a.	n.a.	n.a.	n.a.	n.a.	n.a.
-4.0	54.1	45.9			n.a.	n.a.	n.a.	n.a.	n.a.	n.a.	n.a.	n.a.
-3.5	n.a.	n.a.	n.a.	n.a.	n.a.	n.a.	n.a.	n.a.	100.0			
-3.0	76.1	23.9			100.0				100.0			
-2.5	n.a.	n.a.	n.a.	n.a.	n.a.	n.a.	n.a.	n.a.	90.6	9.4		
-2.0	92.0	8.0			96.2	3.8			88.6	11.4		
-1.5	68.3	31.7			n.a.	n.a.	n.a.	n.a.	84 (1)	16.0		
-1.0	69.3	30.7			86.4 (1)	13.6			83.1	16.9		
-0.5	83.0	17.0			n.a.	n.a.	n.a.	n.a.	79.6 (1)	19.3	1.1	
0.0	67.0	29.0	4.0		80.5 (2)	19.0	0.4	0.1	57.6 (3)	33.2	7.7	1.5
1.0	57.8	27.8	12.9	1.5	63.3	29.8	4.6	2.3	58.9 (3)	17.5	21.1	2.5
2.0	58.0	17.2	15.6	9.2	55.5 (3)	22.4	14.1	8.0	66.9 (2)	3.0	17.0	13.1
3.0	n.a.	n.a.	n.a.	n.a.	57.5 (3)	15.0	14.8	12.7	n.a.	n.a.	n.a.	n.a.
4.0	n.a.	n.a.	n.a.	n.a.	63.7 (2)	6.8	18.8	10.7	n.a.	n.a.	n.a.	n.a.

φ	AOK111 Scoria	Lithic	Glass	Crystal	AOK112 Scoria	Lithic	Glass	Crystal	AOK113 Scoria	Lithic	Glass	Crystal
-4.0	n.a.	n.a.	n.a.	n.a.	100.0				n.a.	n.a.	n.a.	n.a.
-3.5	93.1	6.9			n.a.	n.a.	n.a.	n.a.	n.a.	n.a.	n.a.	n.a.
-3.0	100.0				99.4	0.6			100.0			
-2.5	92.3	7.7			n.a.	n.a.	n.a.	n.a.	n.a.	n.a.	n.a.	n.a.
-2.0	91.2	8.8			99.0	1.0			96.8	3.2		
-1.5	94.5 (1)	5.5			86.1	13.9			n.a.	n.a.	n.a.	n.a.
-1.0	87.4 (1)	12.6			89.2	10.8			83.4 (1)	16.6		
-0.5	79.5	20.5			92.2	7.8			n.a.	n.a.	n.a.	n.a.
0.0	61.6 (2)	31.6	6.8		75.2	23.2	1.6		85.2 (1)	14.0	0.6	0.2
1.0	67.7 (3)	12.8	16.6	2.9	62.8 (2)	18.1	16.0	3.1	51.1 (3)	39.4	7.0	2.5
2.0	76.1 (2)	2.2	14.8	6.9	76.6 (1)	2.7	14.8	5.9	44.7 (3)	33.2	11.3	10.8
3.0	n.a.	n.a.	n.a.	n.a.	n.a.	n.a.	n.a.	n.a.	55.9 (5)	14.3	18.1	11.7
4.0	n.a.	n.a.	n.a.	n.a.	n.a.	n.a.	n.a.	n.a.	58 (3)	11.4	17.7	12.9

φ	AOK114 Scoria	Lithic	Glass	Crystal	AOK115 Scoria	Lithic	Glass	Crystal	AOK116 Scoria	Lithic	Glass	Crystal
-4.0	n.a.	n.a.	n.a.	n.a.	n.a.	n.a.	n.a.	n.a.		100.0		
-3.5		100.0			100.0				n.a.	n.a.	n.a.	n.a.
-3.0		100.0			100.0				42.3	57.7		
-2.5		100.0			8.4	91.6			n.a.	n.a.	n.a.	n.a.
-2.0	2.2 (14)	97.8			67.0	33.0			70.0	30.0		
-1.5	28.3 (4)	71.7			64.8	34.2	1.0		75.1	22.7	2.2	
-1.0	73.7 (2)	26.3			78.5	21.5			76.8	23.2		
-0.5	76.2 (1)	23.8			85.8	14.2			73.9	23.0	3.1	
0.0	45.5 (4)	50.7	2.8	1.0	64.5 (2)	27.5	5.6	2.4	37 (1)	56.1	6.9	
1.0	73.2 (3)	11.2	8.7	6.9	77 (2)	10.2	9.4	3.4	53 (1)	32.1	13.5	1.4
2.0	62.4 (5)	2.1	20.3	15.2	65.2 (3)	3.4	17.1	14.3	57.3 (1)	14.6	21.3	6.8

Table 3.A3 continued

φ	AOK117 Scoria	Lithic	Glass	Crystal	AOK124 Scoria	Lithic	Glass	Crystal	AOK131 Scoria	Lithic	Glass	Crystal
-5.0	n.a.	n.a.	n.a.	n.a.	100.0				n.a.	n.a.	n.a.	n.a.
-4.0		100.0			11.1	88.9			62.5	37.5		
-3.0		100.0			53.6	46.4			72.2	27.8		
-2.5	9.5	90.5			n.a.	n.a.	n.a.	n.a.	n.a.	n.a.	n.a.	n.a.
-2.0	35.9	64.1			30.0	70.0			84.0	16.0		
-1.5	35.4	64.6			62.6	37.4			61.8	38.2		
-1.0	44.7	55.3			62.3	35.8	1.9		72.3	25.8	1.9	
-0.5	65.3	34.7			68.0	30.2	1.8		76.2	22.0	1.8	
0.0	27.2 (1)	67.8	5.0		35.3	56.5	8.0	0.2	55.9 (1)	36.1	8.0	
1.0	47.1 (2)	39.3	12.0	1.6	48.9 (1)	34.1	15.3	1.7	51.3 (2)	30.8	15.3	2.6
2.0	47.4 (7)	19.3	20.9	12.4	55.7 (2)	18.6	17.5	8.2	51.3 (4)	23.3	17.5	7.9

φ	AOK137 Scoria	Lithic	Glass	Crystal	AOK141 Scoria	Lithic	Glass	Crystal	AOK142 Scoria	Lithic	Glass	Crystal
-4.0		100.0			100.0					100.0		
-3.5	n.a.	n.a.	n.a.	n.a.	100.0					100.0		
-3.0		100.0			100.0					100.0		
-2.5		100.0			99.6	0.4				100.0		
-2.0	16.8	81.8	1.4		99.4	0.6				100.0		
-1.5	40.7	57.3	2.0		98.9	1.1			99.7	0.3		
-1.0	41.1	56.6	2.3		96.4	3.6			99.9	0.1		
-0.5	59.7	32.4	7.9		96.1	3.3		0.6	99.3	0.7		
0.0	10.3 (3)	80.8	8.1	0.8	58.9	20.8	15.4	4.9	75.4	9.6	4.4	10.6
1.0	17.7 (6)	66.8	11.6	3.9	45.1	20.2	13.7	21.0	53.8	8.2	11.1	26.9
2.0	16.3 (12)	40.7	27.7	15.3	54.1	21.2	19.9	4.8	73.6	10.9	9.9	5.6

φ	AOK143 Scoria	Lithic	Glass	Crystal	AOK144 Scoria	Lithic	Glass	Crystal	AOK145 Scoria	Lithic	Glass	Crystal
-4.0	100.0				n.a.	n.a.	n.a.	n.a.	n.a.	n.a.	n.a.	n.a.
-3.5	100.0				33.3	66.7			n.a.	n.a.	n.a.	n.a.
-3.0	98.4	1.6			45.5	54.5			100.0			
-2.5	98.1	1.9			80.0	20.0			100.0			
-2.0	98.5	1.5			65.7 (1)	34.3			100.0			
-1.5	98.9	1.1			57.7 (2)	42.3			100.0			
-1.0	95.4	4.6			68.1 (1)	31.9			98.2	1.8		
-0.5	92.6	7.4			72.8 (1)	27.2			96.8	3.2		
0.0	81.8	14.3	3.2	0.7	40.5 (1)	54.2	5.1	0.2	52.7	41.6	4.0	1.7
1.0	47.0	21.6	22.4	9.0	40.7 (4)	36.3	19.8	3.2	14.1	48.1	25.9	11.9
2.0	57 (1)	26.5	12.2	4.2	56.8 (4)	11.8	23.9	7.5	22.2 (4)	29.5	42.7	5.6

Table 3.A3 continued

φ	AOK146				AOK147				AOK149			
	Scoria	Lithic	Glass	Crystal	Scoria	Lithic	Glass	Crystal	Scoria	Lithic	Glass	Crystal
-4.0	100.0				n.a.	n.a.	n.a.	n.a.	n.a.	n.a.	n.a.	n.a.
-3.5	100.0				n.a.	n.a.	n.a.	n.a.	n.a.	n.a.	n.a.	n.a.
-3.0	100.0				83.8	16.2			n.a.	n.a.	n.a.	n.a.
-2.5	100.0				94.3	5.7			100.0			
-2.0	100.0				85.1	14.9			100.0			
-1.5	99.6	0.4			91.6	8.4			100.0			
-1.0	99.9	0.1			88.3	11.7			100.0			
-0.5	99.0	1.0			86.4	13.6			100.0			
0.0	80.6	12.4	4.0	3.0	54.5	42.3	2.6	0.6	94.4	2.9	1.6	1.1
1.0	31.8	18.3	15.7	34.2	29.4 (2)	29.3	34.2	7.1	25.2 (1)	5.3	13.0	56.5
2.0	58.3	17.7	16.3	7.7	41.6 (5)	11.6	23.7	23.1	73.6	14.2	6.0	6.2

φ	AOK150				AOK151				AOK153			
	Scoria	Lithic	Glass	Crystal	Scoria	Lithic	Glass	Crystal	Scoria	Lithic	Glass	Crystal
-3.0					100.0				n.a.	n.a.	n.a.	n.a.
-2.5	100.0				100.0				100.0			
-2.0	74.0	26.0			100.0				80.0	20.0		
-1.5	92.7	7.3			100.0				91.4	8.6		
-1.0	93.1	6.9			100.0				96.5	3.5		
-0.5	96.2	3.8			100.0				97.7	2.3		
0.0	82.4	16.4	1.2		98.8		0.8	0.4	95.4	3.4	0.8	0.4
1.0	32.0	4.7	5.7	57.6	25.0	5.4	19.7	49.9	55.9	6.3	3.5	34.3
2.0	77.0	1.8	18.8	2.4	82.5	10.3	3.8	3.4	67.3	9.2	7.5	16.0

φ	AOK154				AOK164				AOK165			
	Scoria	Lithic	Glass	Crystal	Scoria	Lithic	Glass	Crystal	Scoria	Lithic	Glass	Crystal
-5.0	n.a.	n.a.	n.a.	n.a.	n.a.	n.a.	n.a.	n.a.		100.0		
-4.0	n.a.	n.a.	n.a.	n.a.	n.a.	n.a.	n.a.	n.a.	23.9	76.1		
-3.5	n.a.	n.a.	n.a.	n.a.	100.0				30.8	69.2		
-3.0	n.a.	n.a.	n.a.	n.a.	88.2	11.8			47.5	52.5		
-2.5	n.a.	n.a.	n.a.	n.a.	95.2	4.8			82.5	17.5		
-2.0	100.0				87.9	12.1			44.0	56.0		
-1.5	80.5	19.5			86.9	13.1			59.1	40.0	0.9	
-1.0	71.6	28.4			90.6	9.4			55.8	42.5	1.7	
-0.5	63.4	36.6			93.5	6.5			67.0	32.2	0.8	
0.0	43.2	49.1	7.2	0.5	84.8	14.4	0.8		37.4 (1)	55.4	7.0	0.2
1.0	33.7	43.3	18.2	4.8	81.2	12.0	3.7	3.1	34.7 (2)	53.8	9.8	1.7
2.0	32.8 (1)	19.9	30.5	16.8	78.6	5.3	4.2	11.9	44.9 (4)	17.0	22.9	15.2

Table 3.A3 continued

φ	AOK166				AOK167				AOK169			
	Scoria	Lithic	Glass	Crystal	Scoria	Lithic	Glass	Crystal	Scoria	Lithic	Glass	Crystal
-5.0	100.0				n.a.	n.a.	n.a.	n.a.	n.a.	n.a.	n.a.	n.a.
-4.0	100.0				56.2	43.8			100.0			
-3.5	n.a.	n.a.	n.a.	n.a.	84.6	15.4			100.0			
-3.0	93.7	6.3			66.7	33.3			100.0			
-2.5	87.5	12.5			81.8	18.2			98.3	1.7		
-2.0	72.1	27.9			69.7	29.4	0.9		99.1	0.9		
-1.5	68.7	30.8	0.5		75.9	23.4	0.7		95.5	4.5		
-1.0	70.4	28.3	1.3		82.5	17.2	0.3		71.5	28.2	0.3	
-0.5	71.3	28.7			85.9	14.1			76.3	23.7		
0.0	43.6	51.7	4.4	0.3	68.1	25.5	6.1	0.3	64.2	30.4	5.4	
1.0	52.7	42.1	4.0	1.2	64.0	26.2	6.4	3.4	70.8	16.6	10.8	1.8
2.0	58.8	26.4	8.9	5.9	58.3	14.6	11.6	15.5	70.5	12.9	11.9	4.7

φ	AOK170				AOK171				AOK175			
	Scoria	Lithic	Glass	Crystal	Scoria	Lithic	Glass	Crystal	Scoria	Lithic	Glass	Crystal
-4.0	n.a.	n.a.	n.a.	n.a.	100.0				n.a.	n.a.	n.a.	n.a.
-3.5	100.0				100.0				n.a.	n.a.	n.a.	n.a.
-3.0	100.0				97.8	2.2			n.a.	n.a.	n.a.	n.a.
-2.5	94.7	5.3			86.7	13.3			n.a.	n.a.	n.a.	n.a.
-2.0	96.2	3.8			78.8	20.0	1.2		n.a.	n.a.	n.a.	n.a.
-1.5	94.5	5.5			73.0	24.5	2.5		n.a.	n.a.	n.a.	n.a.
-1.0	90.4	9.6			93.1	6.0	0.9		n.a.	n.a.	n.a.	n.a.
-0.5	88.0	12.0			87.5	7.6	4.9		n.a.	n.a.	n.a.	n.a.
0.0	67.9	14.7	17.4		83.7	12.1	4.2		76.6		23.4	
1.0	67.0	12.8	18.8	1.4	57.2 (1)	22.1	18.0	2.7	47.3 (1)	5.2	46.5	1.0
2.0	65.6	7.1	19.3	8.0	66.7 (1)	10.8	12.5	10.0	44.2	2.9	52.0	0.9

φ	AOK177				AOK187				AOK188			
	Scoria	Lithic	Glass	Crystal	Scoria	Lithic	Glass	Crystal	Scoria	Lithic	Glass	Crystal
-3.0	75.3	24.7			n.a.	n.a.	n.a.	n.a.				
-2.5	56.0	44.0			n.a.	n.a.	n.a.	n.a.	16.0	84.0		
-2.0	72.9	27.1			n.a.	n.a.	n.a.	n.a.	33.9	66.1		
-1.5	67.0	33.0			21.9	78.1			14.2	82.8	3.0	
-1.0	82.1	17.9			15.2	82.8	2.0		14.8	83.3	1.9	
-0.5	85.7	14.3			11.5	85.6	2.9		11.6	85.7	2.7	
0.0	44.7	50.2	5.1		13.7 (2)	83.9	2.4		6.6	87.9	5.5	
1.0	49.2	31.9	13.0	5.9	8.7 (6)	83.3	4.8	3.2	3.0 (6)	86.6	6.5	3.9
2.0	58.9	14.1	21.1	5.9	17.4 (4)	70.7	3.9	8.0	4.4 (16)	78.3	11.2	6.1

φ	AOK189			
	Scoria	Lithic	Glass	Crystal
-3.5	100.0			
-3.0	100.0			
-2.5	100.0			
-2.0	100.0			
-1.5	100.0			
-1.0	100.0			
-0.5	100.0			
0.0	68.0	21.4	5.0	5.6
1.0	48.9	4.2	7.2	39.7
2.0	76.8	7.5	7.6	8.1

References

Allen SR, Cas RAF (2001) Transport of pyroclastic flows across the sea during the explosive, rhyolitic eruption of the Kos Plateau Tuff, Greece, Bull. Volcanol. 62:441-456.

Baer EM, Fisher RV, Fuller M, Valentine G (1997) Turbulent transport and deposition of the Ito pyroclastic flow: determinations using anisotropy of magnetic susceptibility, J. Geophys. Res. 102:22565-22586.

Baines PG (1995) Topographic Effects in Stratified Flows, Cambridge University Press, 482 p.

Black RF (1975) Late quaternary geomorphic processes: Effects on the ancient Aleuts of Umnak Island in the Aleutians, Arctic 28:159-169.

Burgisser A, Bergantz GW (2002) Reconciling pyroclastic flow and surge: the multiphase physics of pyroclastic density currents, Earth Planet. Sci. Lett. 202:405-418.

Bursik MI, Woods AW (2001) The effect of topography on sedimentation from particle-laden turbulent density currents, J. Sediment. Res. 70:53-63.

Byers FM (1959) Geology of Umnak and Bogoslov Islands, Aleutian Island, Alaska, U.S. Geol. Surv. Bull. 1028-L:107-367

Byers FM Jr (1961) Petrology of three volcanic suites, Umnak and Bogoslov Islands, Aleutian Islands, Alaska, Bull. Geol. Soc. Am. 72:93-128.

Carey SN, Sigurdsson H (1980) The Roseau Ash: deep-sea tephra deposits from a major eruption on Dominica, Lesser Antilles Arc, J. Volcanol. Geotherm. Res. 7:67-86.

Carey S, Sigurdsson H, Mandeville C, Bronto S (1996) Pyroclastic flows and surges over water: an example from the 1883 Krakatau eruption, Bull. Volcanol. 57:493-511.

Cas RAF, Wright JV (1987) Volcanic Successions: Modern and Ancient, Allen & Unwin, London, 528 p.

Cas RAF, Wright JV (1991) Subaqueous pyroclastic flows and ignimbrites: an assessment, Bull. Volcanol. 53:357-380.

Choux CM, Druitt TH (2002) Analogue study of particle segregation in pyroclastic density currents, with implications for the emplacements mechanisms of large ignimbrites, Sedimentology 49:907-928.

Clift R, Gauvin WH (1970) The motion of particles in turbulent gas streams, Proceedings of Chemeca '70, 14-28.

Cole PD, Calder ES, Druitt TH, Hoblitt R, Robertson R, Sparks RSJ, Young SR (1998) Pyroclastic flows generated by gravitational instability of the 1996-97 lava dome of Soufriere Hills Volcano, Monserrat, Geophys. Res. Lett. 25:3425-3428.

Denlinger RP (1987) A model for generation of ash clouds by pyroclastic flows, with application to the 1980 eruptions at Mount St. Helens, Washington, J. Geophys. Res. 92:10284-10298.

Druitt T (1992) Emplacement of the 18 May 1980 lateral blast deposit ENE of Mount St. Helens, Washington, Bull. Volcanol. 54:554-572.

Druitt TH (1998) Pyroclastic density currents, in: Gilbert JS, Sparks RSJ (eds), The physics of explosive volcanic eruptions, Geol. Soc. Spec. Publ., London 145:145-182.

Fisher RV (1965) Mechanism of deposition from pyroclastic flows, Am. J. Sci. 264:350-363.

Fisher RV (1990) Transport and deposition of a pyroclastic surge across an area of high relief: The 18 May 1980 eruption of Mount St. Helens, Washington, Geol. Soc. Am. Bull. 102:1038-1054.

Fisher RV (1995) Decoupling of pyroclastic currents: hazards assessments, J. Volcanol. Geotherm. Res. 66:257-263.

Fisher RV, Orsi G, Ort M, Heiken G (1993) Mobility of a large-volume pyroclastic flow - emplacement of the Campanian ignimbrite, Italy, J. Volcanol. Geotherm. Res. 56:205-220.

Freundt A (2003) Entrance of pyroclastic flow into the sea: experimental observation, Bull. Volcanol. 65:144-164.

Freundt A, Schmincke H-U (1985) Lithic-enriched segregation bodies in pyroclastic flow deposits of Laacher See volcano (East Eiffel, Germany), J. Volcanol. Geotherm. Res. 25:193-224.

Freundt A, Wilson CJN, Carey SN (2000) Ignimbrite and block-and-ash flow deposits, in: Sigurdsson H (ed) Encyclopedia of Volcanoes, Academic Press, 581-599.

Fujii T, Nakada S (1999) The 15 September 1991 pyroclastic flows at Unzen Volcano (Japan): a flow model for associated ash-cloud surges, J. Volcanol. Geotherm. Res. 89:159-172.

Gardner JE, Thomas RME, Jaupart C, Tait S (1996) Fragmentation of magma during Plinian volcanic eruptions, Bull. Volcanol. 58:144-162.

Kay SM., Kay RW (1994) Aleutian magmas in space and time *in*: Plafker G, Berg HC (eds.) The Geology of Alaska, Boulder CO, Geol. Soc. Amer., The Geology of North America, G-1:687-722.

Lacroix A (1904) La Montagne Pelée et ses éruptions, Masson, Paris, 662 p.

Legros F, Druitt TH (2000) On the emplacement of ignimbrite in shallow-marine environments, J. Volcanol. Geotherm. Res. 95:9-22.

Lu Z, Mann D, Freymueller JT, Meyer DJ (2000) Synthetic aperture radar interferometry of Okmok Volcano, Alaska; radar observations, J. Geophys. Res. 105:10791-10806.

Mandeville CW, Carey S, Sigurdsson H (1996) Sedimentology of the Krakatau 1883 submarine pyroclastic deposits, Bull. Volcanol. 57:512-529.

Miller TP, Smith RL (1987) Late quaternary caldera-forming eruptions in the eastern Aleutian arc, Alaska, Geology 15:434-438.

Neri A, Macedonio G (1996) Numerical simulation of collapsing volcanic columns with particles of two sizes, J. Geophys. Res. 101:8153-8174.

Piatanesi A, Tinti S (2002) Numerical modeling of the September 8, 1905 Calabrian (southern Italy) tsunami, Geophys. J. Int. 150:271-284.

Pope SB (2000) Turbulent Flows, Cambridge University Press, 771 p.

Pyle DM (1989) The thickness, volume and grainsize of tephra fall deposits, Bull. Volcanol. 51:1-15.

Schumacher R, Schmincke H-U (1990) The lateral facies of ignimbrites at Laacher See volcano, Bull. Volcanol. 52:271-285.

Sigurdsson H, Carey S (1989) Plinian and co-ignimbrite tephra fall from the 1815 eruption of Tambora volcano, Bull. Volcanol. 51:243-270.

Sparks RSJ (1976) Grain size variations in ignimbrite and implications for the transport of pyroclastic flows, Sedimentology 23:147-188.

Sparks RSJ, Bursik MI, Carey SN, Gilbert JS, Glaze LS, Sigurdsson H, Woods AW (1997) Volcanic Plumes, John Wiley & Sons, 574 p.

Sparks RSJ, Sigurdsson H, Carey SN (1980) The entrance of pyroclastic flows into the sea, I. oceanographic and geologic evidence from Dominica, Lesser Antilles, J. Volcanol. Geotherm. Res. 7:87-96.

Sparks RSJ, Wilson L, Hulme G (1978) Theoretical modeling of the generation, movement, and emplacement of pyroclastic flows by column collapse, J. Volcanol. Geotherm. Res. 83:1727-1739.

Suzuki-Kamata K (1988) The ground layer of Ata pyroclastic flow deposit, southwestern Japan; evidence for the capture of lithic fragments, Bull. Volcanol. 50:119-129.

Thomas RME, Sparks RSJ (1992) Cooling of tephra during fallout from eruption columns Bull. Volcanol. 54:542-553.

Todesco M, Neri A, Esposti Ongaro T, Papale P, Macedonio G, Santacroce R, Longo A (2002) Pyroclastic flow hazard assessment at Vesuvius (Italy) by using numerical modeling. I. Large-scale dynamics, Bull. Volcanol. 64:155-177.

Valentine G (1987) Statified flow in pyroclastic surges, Bull. Volcanol. 49:616-630.

Valentine GA, Fisher RV (2000) Pyroclastic surges and blasts, in: Sigurdsson H (ed) Encyclopedia of Volcanoes, Academic Press, 571-580.

Valentine GA, Wohletz KH (1989) Numerical models of plinian eruption columns and pyroclastic flows, J. Geophys. Res. 94:1867-1887.

Whitham AG, Sparks RSJ (1986) Pumice, Bull. Volcanol. 48:209-223.

Wilson CJN (1985) The Taupo eruption, New Zealand II. The Taupo ignimbrite, Phil. Trans. R. Soc. London, A314:229-310.

Wolfe BA (2001) Paleohydrology of a catastrophic flood release from Okmok caldera and post-flood eruption history at Okmok volcano, Umnak Island, Alaska, M.S. Thesis, U. Alaska Fairbanks, 100 p.

Woods AW, Bursik MI, Kurbatov AV (1998) The interaction of ash flows with ridges, Bull. Volcanol. 60:38-51.

Zhang DZ, VanderHeyden WB (2002) The effect of mesoscale structures on the macroscopic momentum equations for two-phase flows, Int. J. Multiphase Flow 28:805-822.

GENERAL CONCLUSIONS

This work focused on the motions of magma within two transport systems that link the storage zone at depth to the vent, and the vent to the flanks of the volcano. Processes at play in this eruptive chain are extremely diverse: in the first transport system, the volcanic conduit, the magma is an active agent in the dynamics because of degassing, whereas in the second system, the pyroclastic density current, magma fragments are passive. Matters are complicated by the transient nature of volcanic eruptions because controlling processes change not only with location but also with time. This complexity and nonlinear nature of the processes is more than a challenge to our imagination, as it limits our predictive horizon of volcanic crises. If, however, the short-term behavior of an unfolding volcanic event depends on only a few local controls, a better understanding of those controls might extend our predictive horizon. An important thread of this work is the appraisal of the key processes at work at a given time and location during a volcanic crisis.

The degassing of magma in response to decompression is extremely complex to simulate because the dynamics of bubbles involve a large number of free parameters. From decompression experiments of hydrated silicate melt, however, we highlighted general trends of growth and isolated the main controls acting at various stages of magma degassing. At depth, the magma goes from bubble-free to low porosity when the decompression starts. At low crystal content, the inception of the magma ascent shows little sensitivity to nucleation kinetics and is controlled by equilibrium growth. As the magma accelerates, the decompression forces disequilibrium degassing. Bubble growth is then controlled by the degree of volatile super-saturation. At medium porosities ($\sim$40 vol.%), the state (open or closed) of the system controls degassing. In closed systems, bubbles grow until fragmentation occurs, whereas in open systems, the bubbles connect, creating permeability and allowing gas to escape. We established that the development of permeability is time dependent and provided its characteristic time scale. We concluded that bubble connectivity is a key to the mysterious transition between explosive and effusive eruptive regimes

In the second chapter, we reappraised the physics of pyroclastic density currents by the means of a Lagrangian approach of the interplay between particles and turbulence. We find that transient particle concentrations are likely to generate density stratification, which causes the currents to

segregate into a dilute part overriding a dense basal part dominated by granular interactions. This reappraisal shows that a simple change in point of view, from a fixed observer as with the traditional, Eulerian approach to a moving observer as in the Lagrangian framework, gives new insights into the transient behavior of turbulent transport. Our model is, however, limited to the dilute part of the current and ignores the granular processes at play in the dense undercurrent. We are still far from predicting the current behavior from initial conditions to complete rest, but it is reasonable to project that coupled Eulerian-Lagrangian approaches of pyroclastic currents dynamics could connect the large-scale, quasi-steady behavior to the internal unsteadiness that controls small-scale deposition. In our view, this connection would be the royal path leading from geological record to initial source conditions.

In the last chapter, the reconstruction of the eruptive sequence of the 2050 BP caldera-forming eruption of Okmok Volcano (Alaska) illustrates both the recent progresses of physical volcanology and the current limitations of this young science. Changes in discharge rate hold the key to many unclear volcanic processes occurring at depth, such as the magmatic chamber (over)pressure history. Complete records of discharge rate during the unfolding of a volcanic crisis are thus necessary to link subaerial behavior to depth processes. From the spatial distribution of fall deposits, we outlined the inception of a major volcanic eruption at Okmok, characterizing the eruptive column and its dispersal axis. The retrieval of vent conditions (i.e., discharge rate of magma) from the spatial distribution and grain size of the fall deposits is a major success of physical volcanology. Our inability, however, to perform the same inversion on pyroclastic current deposits is a severe limitation because it creates exasperating hiatuses in the dynamic sequence we try to recreate. I see the model of pyroclastic currents (Chapter 2) as an interesting way to link deposits to source conditions, because its application to Okmok deposits provided an upper estimate of the discharge rate. This estimate, however, is weakened by our ignorance of sedimentary processes in granular flows, because most of the mass was transported within the dense part of the current. Beyond the fact that our model does not address the dynamics of granular flow, I think that our general lack of understanding of the granular question blocks our ability to provide a harmonized template of segregated pyroclastic currents and shall be tackled.

Using our model of pyroclastic currents, I showed how to retrieve the speed and thickness of the dilute part from the analysis of individual locations, and, when topography causes the current

to decouple, the relative thickness of both its dense and dilute parts. The spatial distributions of current speed and thickness are remarkably consistent, suggesting that local conditions reflect large-scale behavior when the topography is smooth. Importantly, speed estimates are consistent with an independent estimate of the velocity of a tsunami wave. I view this study as a first step to validating our model presented in chapter 2. A natural subsequent step would be to compare estimates from our model with independent measures of the current velocity and internal particle concentration.

Finally, this work illustrates two opposed tendencies in the scientific approach: the validity of the simplification of complex bubble dynamics by empirical experiments and the danger of overlooking the complexity introduced by the transient interaction of particles and turbulence. Too simple or too complex, the right balance of simplification to represent natural systems is not easy to achieve. In fact, such a balance probably does not exist because science is constantly improving, and thus shares the same condition as the humans who dream it: "S'il se vante, je l'abaisse; s'il s'abaisse, je le vante et le contredis toujours jusqu'à ce qu'il comprenne qu'il est un monstre incompréhensible" (if he (Men in general) praises himself, I deprecate him; if he deprecates himself, I praise him and always contradict him until he understands that he is an incomprehensible monster; Pascal 1670). Science, an incomprehensible monster?

Reference

Pascal B (1670) Pensées, Editions Le Seuil, Fragment 121.